Simulation de modèles personnalisés du coeur pour la prédiction de thérapies cardiaques

Stephanie Marchesseau

ParisTech
INSTITUT DES SCIENCES ET TECHNOLOGIES
PARIS INSTITUTE OF TECHNOLOGY

MINES ParisTech

École doctorale n°84:
Sciences et technologies de l'information et de la communication

Doctorat ParisTech

T H È S E

pour obtenir le grade de docteur délivré par

l'École nationale supérieure des mines de Paris

Spécialité " Informatique temps-réel, robotique et automatique "

présentée et soutenue publiquement par

Stéphanie MARCHESSEAU

le 28 Janvier 2012

Simulation de modèles personnalisés du coeur pour la prédiction de thérapies cardiaques

~~~

Simulation of patient-specific cardiac models for therapy planning

Directeur de thèse: **Hervé DELINGETTE**
Co-encadrement de la thèse: **Nicholas AYACHE, Maxime SERMESANT**
Thèse préparée à l'INRIA Sophia Antipolis, projet Asclepios

Jury

Andrew MCCULLOCH, Department of Bioengineering, UC San Diego	Rapporteur/Président
Nicolas SMITH, St. Thomas' Hospital, King's College London	Rapporteur
Dominique CHAPELLE, MACS Research Team, INRIA Saclay Ile-de-France	Examinateur
Oscar CAMARA, PhySense, Universitat Pompeu Fabra	Examinateur
Reza RAZAVI, St. Thomas' Hospital, King's College London	Examinateur
Nicholas AYACHE, Asclepios Research Project, INRIA Sophia Antipolis	Examinateur
Hervé DELINGETTE, Asclepios Research Project, INRIA Sophia Antipolis	Directeur
Maxime SERMESANT, Asclepios Research Project, INRIA Sophia Antipolis	Examinateur

T H È S E

MINES ParisTech
Centre de Mathématiques Appliquées
Rue Claude Daunesse B.P. 207, 06904 Sophia Antipolis Cedex, France
~~~

This thesis was prepared in ASCLEPIOS Research Project, Sophia Antipolis, FRANCE. It was partially funded by the European Community's euHeart project under grant agreement 224495 and by the ERC advanced Grant MedYMA 291080.

To G.L.P., who was with me all the way.

Simulation de modèles personnalisés du coeur pour la prédiction de thérapies cardiaques

Résumé : La compréhension clinique et le traitement des maladies cardiovasculaires est extrêmement complexe. Pour chaque patient, les cardiologues sont confrontés à des difficultés pour déterminer la pathologie, choisir une thérapie ou encore sélectionner les patients susceptibles de bien répondre à un traitement donné. Afin de fournir une aide additionnelle aux cardiologues, de nombreuses équipes de recherche étudient la possibilité de planifier de telles thérapies grâce à des modèles biophysiques du cœur. Ils formulent l'hypothèse que l'on peut combiner les données fonctionnelles et anatomiques afin de créer des modèles cardiaques personnalisés à chaque patient qui auraient le potentiel de prédire les bénéfices des différentes thérapies. Les simulations électromécaniques du cœur sont basées sur des modèles informatiques qui peuvent représenter la géométrie, le mouvement et la propagation d'ondes électriques pendant un cycle cardiaque avec suffisamment de précision. L'intégration d'information anatomique, mécanique et électrophysiologique pour un patient donné est essentielle pour construire ce type de modèle.

Dans cette thèse, nous présentons tout d'abord les méthodes de personnalisations géométriques, cinématiques et électrophysiologiques nécessaires à toutes modélisations mécaniques. Nous utilisons ensuite le modèle électromécanique de Bestel-Clément-Sorine qui a déjà prouvé avoir un bon réalisme sans être trop complexe au vu des données disponibles. Nous commençons par détailler la nouvelle implémentation de ce modèle dans une plateforme efficace de simulation médicale ayant l'avantage d'être libre et interactive, puis nous analysons les résultats de la simulation par une étude de sensibilité complète.

Dans un deuxième temps, nous étudions la possibilité de personnaliser les paramètres mécaniques de ce modèle à partir d'images médicales (IRM). Pour cela, nous proposons en premier lieu une méthode automatique de calibration qui estime les paramètres mécaniques globaux à partir de courbes de pressions et volumes. Cette technique testée sur 6 volontaires et 2 cas pathologiques nous a permis de faire une étude de spécificité qui consiste à déterminer les paramètres pertinents capables de différencier les cas pathologiques des cas sains.

Une fois initialisés à ces valeurs calibrées, les paramètres sont personnalisés localement avec un algorithme d'optimisation plus complexe. Le « Reduced Order Unscented Kalman Filtering » est utilisé pour estimer les contractilités de toutes les zones AHA du ventricule gauche à partir des volumes régionaux extraits des séquences d'images IRM. Cette stratégie de personnalisation a été validée et testée sur plusieurs cas pathologiques et volontaires. Ces différentes contributions ont montré des résultats prometteurs tout au long de cette thèse et certains sont déjà utilisés pour quelques études de recherche.

Mots clés : Modélisation Cardiaque ; Mécanique Cardiaque ; Modèle Informatique ; Etude de Sensibilité ; Etude de Spécificité ; Calibration des Paramètres ; Personnalisation ; Imagerie Medicale

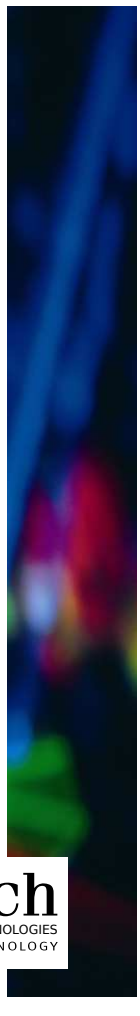

MINES ParisTech

ParisTech
INSTITUT DES SCIENCES ET TECHNOLOGIES
PARIS INSTITUTE OF TECHNOLOGY

Simulation of patient-specific cardiac models for therapy planning

Abstract: The clinical understanding and treatment of cardiovascular diseases is highly complex. For each patient, cardiologists face issues in determining the pathology, choosing a therapy or selecting suitable patients for the therapy. In order to provide additional guidance to cardiologists, many research groups are investigating the possibility to plan such therapies based on biophysical models of the heart. The hypothesis is that one may combine anatomical and functional data to build patient-specific cardiac models that could have the potential to predict the benefits of different therapies. Cardiac electromechanical simulations are based on computational models that can represent the heart geometry, motion and electrophysiology patterns during a cardiac cycle with sufficient accuracy. Integration of anatomical, mechanical and electrophysiological information for a given subject is essential to build such models.

In this thesis, we first introduce the geometry, kinematics and electrophysiology personalizations that are necessary inputs to mechanical modeling. We propose to use the Bestel-Clément-Sorine electromechanical model of the heart, which is sufficiently accurate without being over-parametrized for the available data. We start by presenting a new implementation of this model in an efficient opensource framework for interactive medical simulation and we analyze the resulting simulations through a complete sensitivity analysis.

In a second step, the goal is to personalize the mechanical parameters from medical images (MRI data). To this end, we first propose an automatic calibration algorithm that estimates global mechanical parameters from volume and pressure curves. This technique was tested on 7 volunteers and 2 heart failure cases and allowed to perform a preliminary specificity study that intends to determine the relevant parameters able to differentiate the pathological cases from the control cases.

Once initialized with the calibrated values, the parameters are then locally personalized with a more complex optimization algorithm. Reduced Order Unscented Kalman Filtering is used to estimate the contractilities on all of the AHA zones of the Left Ventricle, matching the regional volumes extracted from cine MRI data. This personalization strategy was validated and tested on several pathological and healthy cases. These contributions have led to promising results through this thesis and some are already used for various research studies.

Keywords: Cardiac Modeling; Cardiac Mechanics; Computer Model; Sensitivity Analysis; Specificity Analysis; Parameter Calibration; Patient-Specific; Medical Imaging

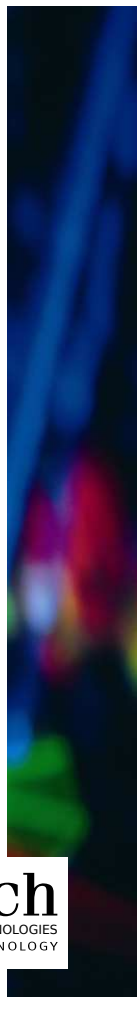

MINES ParisTech

ParisTech
INSTITUT DES SCIENCES ET TECHNOLOGIES
PARIS INSTITUTE OF TECHNOLOGY

Remerciements

Je tiens tout d'abord à remercier chaleureusement Hervé Delingette, Nicholas Ayache et Maxime Sermesant pour avoir su me guider et m'encadrer tout au long de ma thèse. J'ai particulièrement apprécié les heures passées avec Hervé à élaborer les méthodes, l'instinct visonnaire de Nicholas et le soutien permanent de Maxime. Leur grande disponibilité et générosité ont largement contribué à l'aboutissement de ce travail.

Mes sincères remerciements sont également adressés à mes collègues d'Asclepios sans qui ces années de thèse auraient éte bien moins agréables. Notamment, je tiens à remercier Kristin McLeod, une amie sur qui j'ai pu compter que ce soit professionellement ou personellement; Jatin Relan pour son aide quant à la mise en place parfois laborieuse d'outils indispensables à ma thèse et sa patience dans leur apprentissage; Adityo Prakosa, Tomasso Mansi, Ken Wong et Florence Billet pour leurs conseils avisés sur le fonctionnement du coeur; Loïc Le Folgoc et Ján Margeta, mes cobureaux dotés d'une gentilesse, d'une patience et d'une écoute sans faille; Muriel Laffon et Christof Seiler dont le bref passage dans l'équipe a pimenté mon quotidien; Olivier Clatz qui a su me montrer la voie; et tous les autres pour leur constante bonne humeur. Un "merci" spécial à Isabelle Strobant qui rend notre séjour dans l'équipe bien plus facile.

Je remercie de plus mes collaborateurs de King's College London et de l'INSERM qui ont eu la bonté de me fournir des données de qualité sans lesquelles ma thèse n'aurait pu mener à de telles conclusions; et pour leur aide quant à l'analyse des résultats sur un plan physiologique. Sincères remerciements à UPF Barcelone qui a tant aidé dans le traitement des données, et spécialement Catalina Tobon-Gomez avec qui j'ai eu un vrai plaisir à travailler.

Je tiens aussi à remercier mes collègues de l'INRIA Rocquencourt chez MACS, et notamment Marc Fragu dont la venue dans nos locaux a fait grandement progresser mon projet; Radomir Chabiniok qui a beaucoup inspiré mon travail; Philippe Moireau, Dominique Chapelle et Michel Sorine pour leurs remarques et aides constructives quant à la compréhension du modèle cardiaque.

Je remercie sincèrement les membres de mon jury de thèse et particulièrement Andrew McCulloch et Nic Smith qui ont eu la gentillesse de prendre le temps de lire ce manuscript avec attention.

Enfin je remercie tous ceux qui ont toujours cru en moi, mes amis, ma famille, Geoffroy.

MERCI !

Contents

Chapter 1

Introduction

Contents

1.1 Why Building Patient-Specific Models of the Heart?

1.1.1 Clinical Context

Worldwide, 17 millions people die each year from cardiovascular disease[1], particularly heart attacks and strokes. In Europe, cardiovascular disease causes 46 times the number of deaths of AIDS, tuberculosis or malaria combined and represents the major cause of death. At least 80% of these deaths could be prevented either by a healthier life style or a better detection and prediction of the disease.

The early detection and prediction of such disease has therefore become a major challenge to improve patient health and reduce morbidity. Significant progress has been made in the past 20 years in the medical imaging field in order to replace invasive methods. Computed Tomography (CT) scans, electrocardiography and Magnetic Resonance Imaging (MRI) allow to better study the cardiovascular system and clearly detect wall thickness, chamber flow patterns, and follow the myocardium motion along the cardiac cycle.

[1] Facts and figures from http://www.who.int/ncd/cvd/

The variety of currently available data offers great opportunities to improve clinical outcome of cardiovascular disease. The possible measurement allows to detect cardiomyopathy, asynchronous behavior, tachycardia and so on. However, the overflow of information is difficult to process for the clinical practice and often leads to inter-subject variability in pathophysiology. Thus, despite some tremendous advances in imaging and other data acquisitions, determining the optimal treatment remains a challenge.

As an example, Cardiac Resynchronization Therapy, which aims at relieving heart failure symptoms by reducing heart dysynchrony, still gives 30% of non-responders within the treated patients (Smith et al., 2011). The selection of the patients as well as the location of the pacemaker leads is currently not optimized and the clinical definition of the targeted group of patients rather unclear. Finding answers to these optimization issues could therefore give additional guidance to cardiologists.

1.1.2 Role of Medical Image Computing

To give additional guidance to cardiologists, several research groups are working on automatic tools to extract information from the images, simulate the cardiac behaviour under some therapies. The vision is to combine anatomical and functional data to build biophysical models that can reproduce the patient's heart function and therefore simulate the outputs of some therapies *in silico*, study the effects of drugs or quantify the pathology.

Advances have been made on this topic in the past 15 years. First, several automatic (or semi-automatic) tools now exist to extract the geometry of cardiac anatomy from MRI data (Tobon-Gomez et al., 2012b; Ecabert et al., 2011). Imaging softwares also allow to measure interactively some distances (MedInria, Cardioviz3D, Segment, GIMIAS,...). This already helps cardiologists in quantifying a pathology such as a cardiomyopathy or an abnormal large right ventricle.

Second, from the sequence of images, we can extract the movement of the myocardium, and other cardiac structures. Many research groups (Mansi et al., 2011; De Craene et al., 2012a) are still trying to automatically register the motion from MRI data facing significant difficulties. Indeed, since in 3D cine MRI data the slices are taken for several cycles and then resynchronized, the visible motion is perturbed. Moreover, the resolution is pretty low and very anisotropic making the muscle contours challenging to determine with accuracy even manually. Motion tracking can give precious clinical indices of the patient's state such as the ejection fraction or the regional volumes, as well as an estimate of the real motion.

Finally, using the anatomy and cardiac motion extracted from images as a ground truth, as well as electrocardiograms, endocardial pressures, aortic blood pressures and other available measurements, we aim at personalizing electromechanical models of the heart, that is to say we can adapt a generic model to each patient. To this end, a good compromise between the modeled biophysical behavior and the information extracted from images must be found. Once the model is patient-specific, several therapies can be simulated such as cardiac resynchronization therapy, atrial defibrillation, radio-frequency ablation, valve replacement and so on. This could, once further validated, improve the success rate of the therapies and decrease therefore the morbidity (Smith et al., 2011; Mansi et al., 2009; Sermesant et al., 2012).

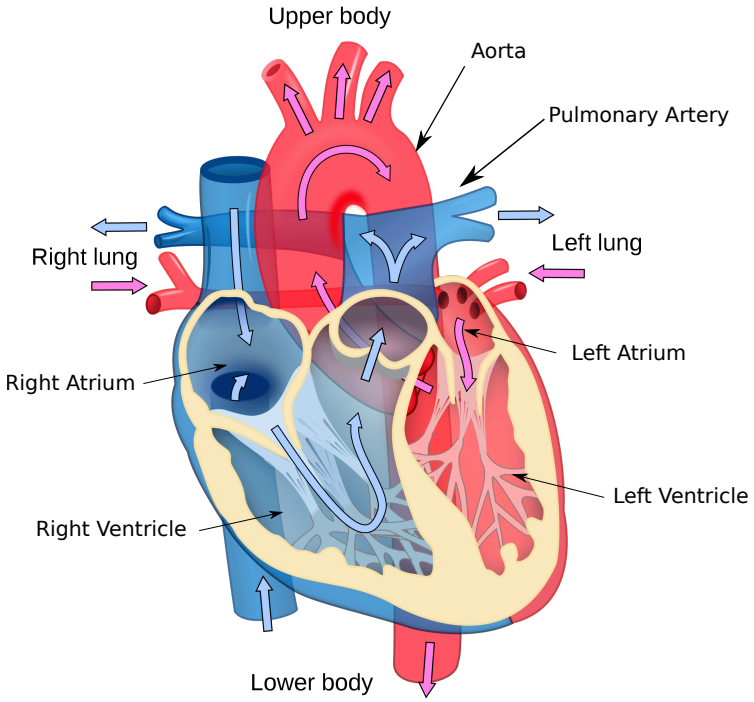

Figure 1.1: (Left) Heart anatomy showing the right and left heart that work synchronously to pump the blood in the pulmonary and general system. Blue vessels represents the blood poor in oxygen and red the blood rich in oxygen. *Modified image from Wikipedia.*

1.2 How Are Such Models Built?

Building an efficient electromechanical model of the heart requires a high knowledge of the structure and function of the heart at different scales.

1.2.1 Structure and Function of the Heart

The heart is a biological engine that pumps the blood through the human body about 70 times per minute. Blood is transported towards the organs to provide them with oxygen and towards the lungs to collect the oxygen in a closed loop. The heart is therefore separated into two parts (see Fig.1.1). The blood poor in oxygen first arrives in the right atrium then is pushed towards the right ventricle before being ejected during the cardiac contraction towards the lungs. Once oxygenated, the blood arrives in the left atrium, is pushed inside the left ventricle and ejected towards the rest of the body during the cardiac contraction. A higher blood pressure is applied by the left ventricle since the circulatory system is much longer than for the right ventricle which is why the left ventricle is thicker and therefore more powerful than the right ventricle.

Cardiac contraction and relaxation are controlled by two biological phenomena. First, an electrical wave propagates along the myocardium to depolarize the cells. Then, the depolarized cells contract and relax to create the global motion.

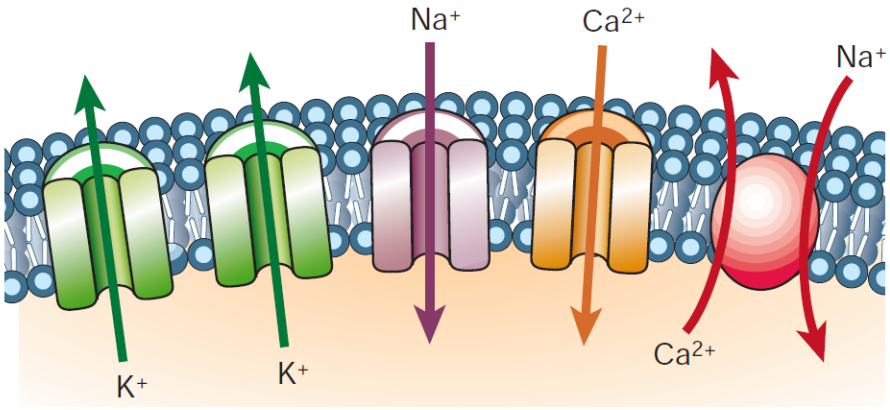

Figure 1.2: Ion exchanges at the surface of the myocytes that create the action potential. *Image from (Marbán, 2002).*

Cardiac Electrophysiology

The electrical wave is triggered by the modification of ion concentration across the surface membrane of each heart cell, also called *myocytes* (see Fig.1.3) which creates the action potential following 5 phases (numbered 0 to 4) as shown Fig.1.2. At rest (Phase 4), the potential inside the myocyte is negative with respect to the outside since the membrane is selectively permeable to various ions. Indeed, the membrane is most permeable to K^+ ions and relatively impermeable to other ions. During electrical activation (Phase 0), the potential reverses (or *depolarizes*) while the membrane becomes permeable to Na^+ ions and the Na^+ channels open. In phase 1, the Na^+ channels desactivate and movement of K^+ and Cl^- ions cause the small downward deflection in the action potential. The "plateau" in phase 2 is sustained by a balance between Ca^{2+} ions moving into the cell and K^+ moving out of the cell and activates the contraction of the myocyte through a calcium-induced calcium release process (Endo, 1977). Once depolarized, the myocytes stay excited during a *refractory period* during which the cell cannot be excited anymore. Finally the Ca^{2+} channels close in phase 3 for the repolarization phase and by re-equilibrating the ion concentration, the negative potential is restored and the cell relaxes.

Electrocardiograms (ECG) enables to record the electrical wave propagation, or sinus rhythm (see Fig.1.4). The electrical wave starts at the sinoatrial node of the atria, also called *physiological pacemaker*, and propagates through the right atrium and then the left atrium leading to the contraction of both atria. This can be seen on the ECG as the P wave. The electrical wave is then delayed at the atrioventricular node (AV node) during the PR segment to allow the atria to finish their contraction. Then, the wave propagates through the Bundle of His where it splits into two bundle branches before going to the left and the right ventricles. Both bundles then produce numerous fibers called *Purkinje fibers* in order to stimulate groups of myocytes. The time during which the electrical depolarization is spread through the ventricle represents the QRS complex. Finally, the cycle finishes with the repolarization of the ventricles during the T wave.

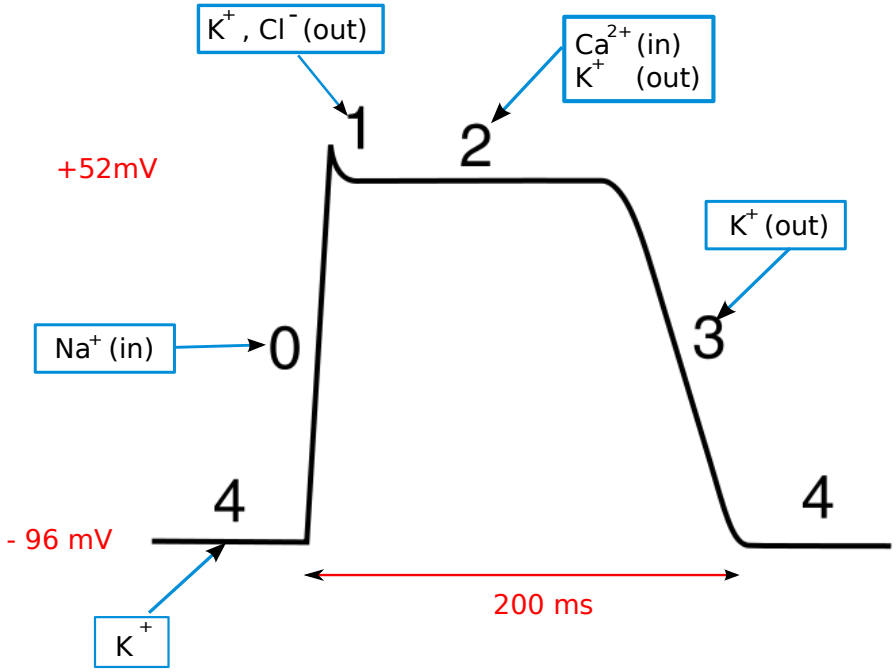

Figure 1.3: Phases of the action potential. *Image from Wikipedia.*

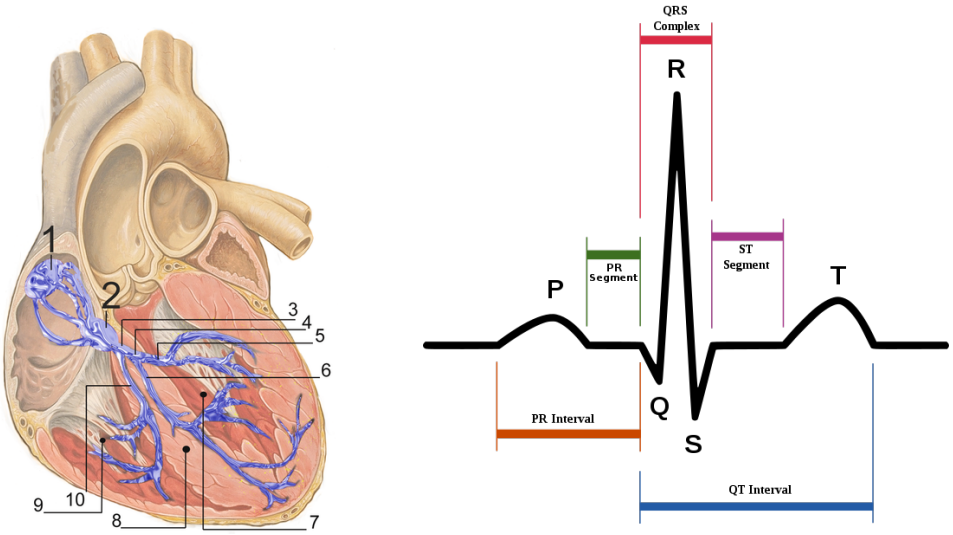

Figure 1.4: (Left) Conduction system with (1)-Sinoatrial node (2)-Atrioventricular node (3)-Bundle of His (4)-Left bundle branch (5)-Left anterior fascicle (6)-Left posterior fascicle (7)-Left ventricle (8)-Ventricular septum (9)-Right Ventricle (10)-Right bundle branch. (Right) Schematic diagram of normal sinus rhythm as seen on ECG. *Images from Wikipedia.*

Cardiac Mechanics

The myocardium is a muscle contracting depending on the cellular ion concentrations along preferred directions. The muscle is contracting along fibers which are bundles of myofibril. These myofibrils can be detailed in series of sarcomeres which are separated by Z-discs. A sarcomere is composed of thin filaments (actin) and thick filaments (myosin) responsible for the contraction and relaxation. Troponin is a component of thin filaments, attached to the protein tropomyosin which blocks the attachment sites for the myosin crossbridges in a relaxed muscle. During contraction, the free calcium ions enter into the sarcomere and some of them attach to troponin causing the actin filaments to change shape and allow the myosin to connect. More precisely, troponin has three subunits: TnC, TnI and TnT. When free calcium ions enter the sarcomere, TnC binds to calcium ions and causes the dislocation of TnI which holded the actin-tropomyosin complex into place. So tropomyosin moves out of the active sites leaving them free for the myosin. Myosin binding to actin creates the crossbridges, the filaments slide towards the Z-discs leading to the shortening of the sarcomere. When the calcium ions are released, the myosin and actin filaments unbind and the sarcomere comes back to its rest state.

At the organ level, the ventricles are filled with blood coming from the atria and ejected through the arteries, with valves ensuring the proper circulation. The closing and opening of these valves lead to four cardiac phases (filling, isovolumetric contraction, ejection and isovolumetric relaxation) (Fig.1.5). First, the ventricles passively filled up with blood from

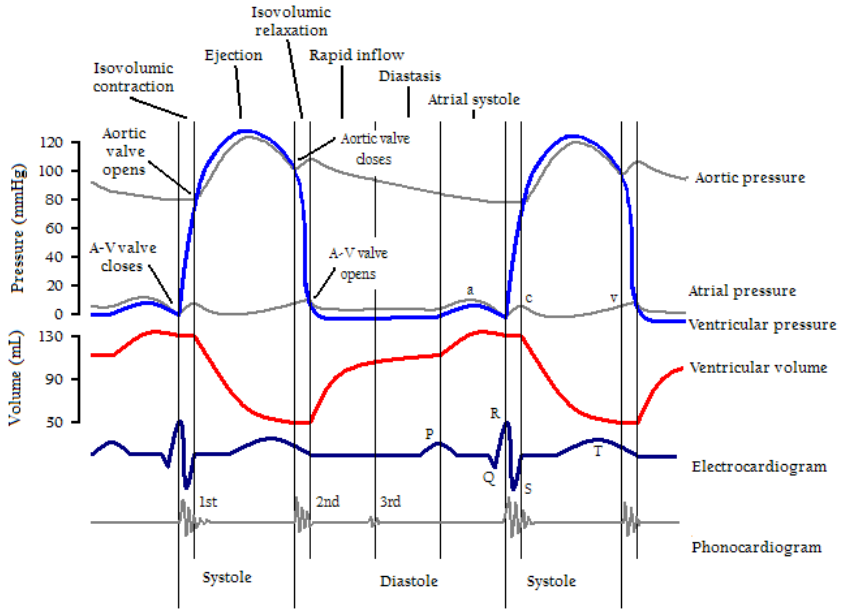

Figure 1.5: Cycle of the left ventricle. *Image from Wikipedia.*

the atria. Then, the atria start contracting and actively eject blood into the ventricles. The atrioventricular valves then close (which generates the first noise of a heart beat) and the ventricles start contracting. The ventricular pressures quickly rise (isovolumetric contraction) until they become higher than the arterial pressures forcing the arterial valves to open. The blood is ejected towards the arteria (ejection) and the pressures still rise and then decrease when the ventricle start relaxing. When the ventricular pressures drop below the

arterial pressures the arterial valves close (second noise) and the isovolumetric relaxation starts. When the pressure becomes lower than the atrial pressure the atrioventricular valves open and the filling phase starts again.

1.2.2 State of the Art of Existing ElectroMechanical Models

Several types of models are already available to represent the cardiac electrophysiology or/and the electromechanical coupling.

Cardiac Electrophysiology

Since the work of (Hodgkin and Huxley, 1952; FitzHugh, 1961), several approaches have been developed to reproduce the propagation of the electrical wave across the cardiac muscle. There exists bi-domain and mono-domain models. Bi-domain models separate the cardiac tissue into intracellular and extracellular domains leading to coupled differential equations with different parameters for both domains. In the mono-domain formulation, the extracellular potential is fixed and therefore the intracellular potential is equal to the transmembrane potential leading to one differential equation. We divide the mono-domain models into three categories:

- **Ionic Biophysical models**: work at the scale of the cell to represent the ionic interactions (Noble, 1962; Noble et al., 1998; Ten Tusscher et al., 2004). Those very detailed models depending often on more than 50 parameters, can control every ion channel through reaction-diffusion partial differential equations.
- **Macroscopic Biophysical models**: work at a more macroscopic level by describing the propagation of the action potential directly without focusing on the ionic phenomena (FitzHugh, 1961; Nagumo et al., 1962; Aliev and Panfilov, 1996; Mitchell and Schaeffer, 2003). They also rely on reaction-diffusion differential equations but with a limited number of parameters.
- **Eikonal models**: are the simplest ones. These models control the electrical wave by computing its arrival time (depolarization time) at a given point of the myocardium (Colli Franzone et al., 1990; Keener and Sneyd, 2009). An extension of this model (Sermesant et al., 2006) computes as well the repolarization times. These models are governed by one or two parameters only. Solving these models has been done very efficiently with Fast Marching Methods (Sermesant et al., 2007).

Biophysical models are more sophisticated and can reproduce better the electrical wave propagation than the simplified phenomenological models or Eikonal models. Nevertheless, they are computationally expensive and over-parametrized for the data usually available. On the other hand, Eikonal models can be simulated efficiently and personalized easily since they depend on few parameters. However, they are extremely simplified and cannot reproduce complex pathologies like fibrillation for instance. Therefore, one has to choose and adapt a model depending on the needs and the available data.

Cardiac Mechanics

The myocardium is mainly made of active myocytes and of hyperelastic soft tissue whose motion is controlled by the propagation of the electrical wave. Its constitutive law is com-

plex, coupling active contraction with passive elasticity, viscosity and friction. Several categories of models intend to represent the active contraction, simulated as an external force that makes the myocardium contract. We can therefore find:

- **Ionic Biophysical Models**: that work on the ion interactions and the actin-myosin binding process to generate the cardiac motion (Hunter et al., 1997; Nash, 1998; Niederer et al., 2006). These very detailed models reproduce the biological mechanisms of sarcomere contraction at the tissue level, with complex equations depending on a large number of parameters related to ionic phenomena.
- **Macroscopic Multi-Scale Biophysical Models**: that derive their equations from the unbinding-binding process at the macroscopic level from statistical mechanics involving the Huxley filament model (Huxley, 1957). These models (Bestel et al., 2001; Sainte-Marie et al., 2006; Chapelle et al., 2012b) build the dynamical system from thermodynamical laws and take into account every involved energy terms.
- **Lumped Models**: focus on one single myocyte. They are analytical models of fiber contraction that therefore do no take into account the spatial variability and do no require a mesh to be solved (Arts et al., 1979).

As for the passive part, several elasticity behaviors have been though of, from linear anisotropic (Sermesant et al., 2006), to isotropic hyperelastic (Bestel et al., 2001) or orthotropic (Holzapfel and Ogden, 2009; Wong et al., 2008; Mazhari and McCulloch, 2000). One major point to consider is the number and observability of parameters that will then need to be estimated. Furthermore, with orthotropic hyperelasticity, fiber, sheet and normal directions have to be known, which is still very challenging.

Therefore, several mechanical models exist with different scale of modelling, complexity and number of parameters. Depending on the modelling goal and the available data, one may choose the corresponding model.

1.3 How are Such Models Personalized?

Personalizing the electromechanical models is very challenging. One needs to combine all available data and extract relevant information at several stages of the personalization (see Fig.1.6). In this thesis, MRI data only were studied.

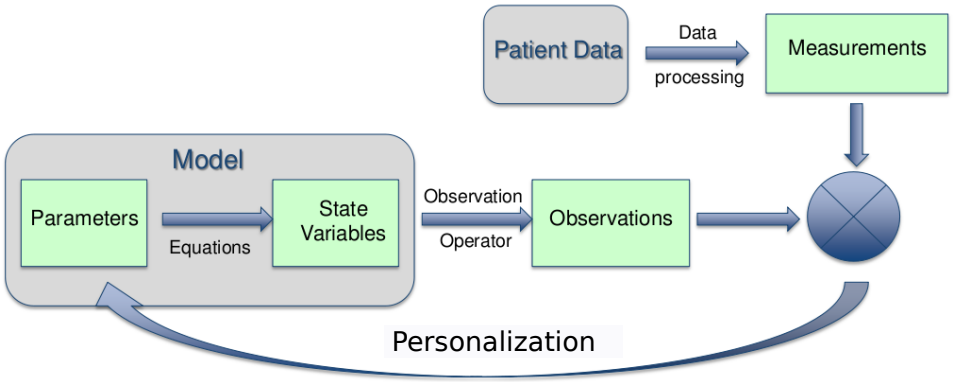

Figure 1.6: Schematic representation of the personalization pipeline.

1.3.1 Processing Imaging Data

Several types of imaging modalities exist, with different purposes and resolutions. To retrieve anatomical information, static 3D SSFP are usually the most convenient since the resolution is pretty high and the field of view include the four chambers (see Fig.1.7). Several

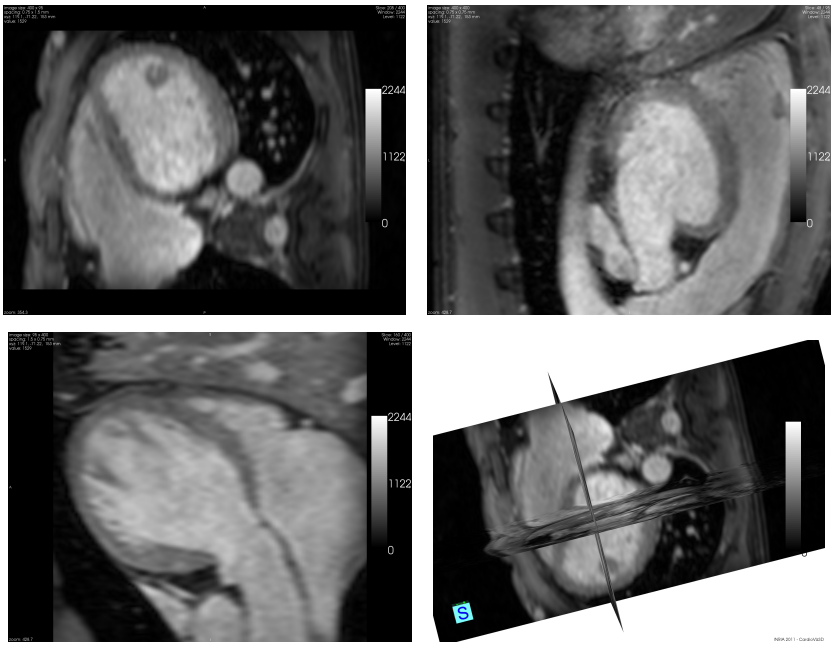

Figure 1.7: Example of static 3D SSFP MR images. Top Left: view with resolution 1.5 mm x 0.75 mm; Top Right: view with resolution 0.75 mm x 0.75 mm; Bottom Left: view with resolution 1.5 mm x 0.75 mm; Bottom right: 3D view.

automatic or interactive tools already exist to create the myocardium geometry (Ecabert et al., 2011; Larrabide et al., 2009).

To study the movement of the cardiac muscle, a time series of images is necessary. We use in this thesis the cine SSFP MRI data which is acquired through several cardiac cycles and then resynchronized using ECG signals. Much less slices are taken for cine MRI leading to a low number of axial slices (see Fig.1.8). Moreover, only two chambers are visible so the movement of the atrium as well as the motion of the basal area cannot be precisely registered.

Tagged-MRI data enables to follow the movement of the myocardium (usually Left ventricle only) through a grid attached to the voxels that will be deformed over time (see Fig.1.9). This imaging modality is very useful to make the registration point-wise. Unfortunately, tagged MRI data are rarely available for pathological cases.

1.3.2 Electrophysiology Personalization

Electrophysiology model personalization can be basically addressed as an inverse problem of parameter estimation. Considerable progress has been made to tackle this issue. First, Moreau-Villéger et al. (2006) used a single heart cycle for 2D phenomenological Aliev & Panfilov model, where the AP propagation was simulated on a simple surface mesh mod-

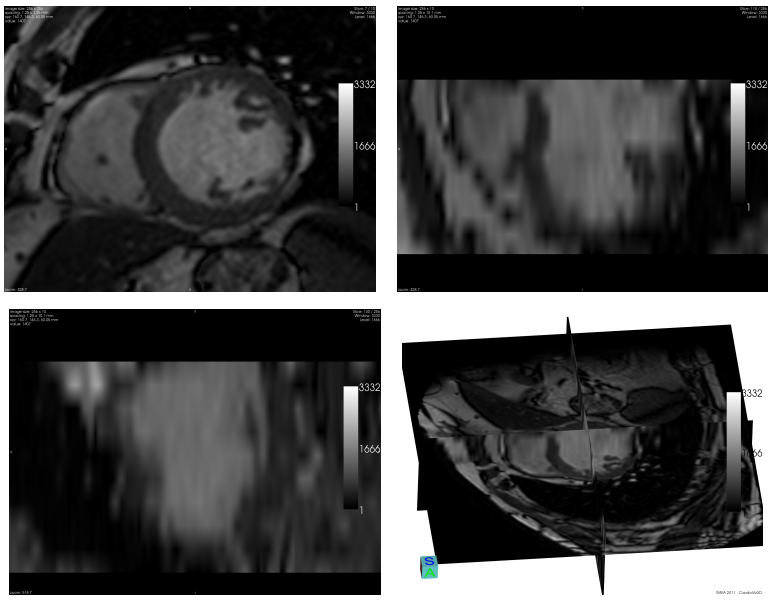

Figure 1.8: Example of cine SSFP MR images. Top Left: short axis view with resolution 1.25 mm x 1.25 mm; Top Right: Long axis view with resolution 1.25 mm x 10.1 mm; Bottom Left: Long axis (orthogonal) view with resolution 1.25 mm x 10.1 mm; Bottom right: 3D view.

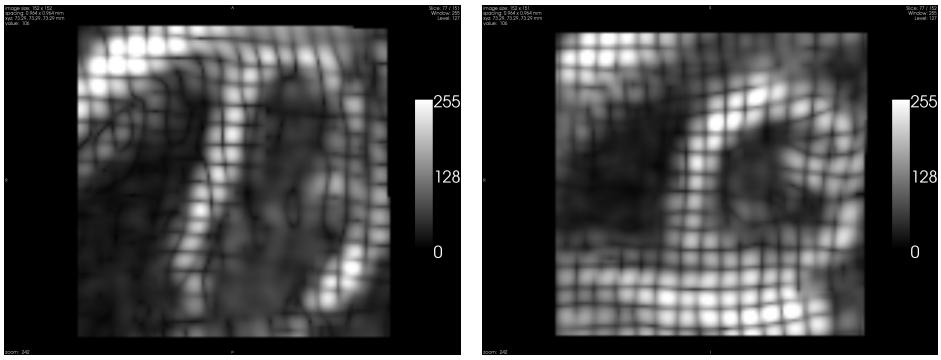

Figure 1.9: Example of tagged MR images. Left: long axis view with resolution 0.9 mm x 0.9 mm; Right: Short axis view with resolution 0.9 mm x 0.9 mm.

elling a dog's heart epicardium. Then, Chinchapatnam et al. (2008) performed the same adjustment for patient data on 2D Eikonal models. Initial step towards personalization of the 3D Aliev & Panfilov model were taken in (Lepiller et al., 2008) with adjustment of Depolarization Times and Action Potential Durations from a single cycle. Finally, Relan et al. (2011a) proposed a personalization framework for a 3D macroscopic Mitchell & Schaeffler model on a volumetric bi-ventricular mesh of the myocardium using 2D epicardial surface data.

1.3.3 Mechanics Personalization

Finally, personalizing mechanics, which is the focus of this thesis, consists in optimizing mechanical parameters of the model so that the simulation behaves, as much as possible in accordance to patient-specific datasets (images and other signals) without loosing its

physiological behavior and predictive power. This inverse problem has been tackled by different authors. For instance, Moireau and Chapelle (2011a) as well as Chabiniok et al. (2011) estimate the contractility parameters using Reduced Order Unscented Kalman Filtering (ROUKF). Xi et al. (2011) compared ROUKF and Sequential Quadratic Programming for the estimation of passive material parameters from synthetic data. Wang et al. (2009) use Sequential Quadratic Programming in order to estimate passive material stiffness from tagged MRI and *ex-vivo* DT-MRI of dog's hearts. Liu and Shi (2009) applied the extended Kalman Filtering on 2D slices from tagged or cine MRI in order to estimate passive parameters. Finally, Sundar et al. (2009) and Delingette et al. (2012) rather use adjoint variational methods to estimate the contractility parameters from synthetic cardiac motion and real pathological cases for the latter. Variational methods have the advantage of being robust to the initialization but require to differentiate a cost function which is computationally expensive and not modular (every change in the model leads to a manual re-derivation of the method). On the other hand, sequential methods can easily be made parallel leading a a fast computation, some do not require a differentiation, but they depend on the initialization.

1.4 Manuscript Organization and Main Contributions

1.4.1 Main Contributions

During this PhD study, four main contributions were proposed.

- A new implementation of the Bestel-Clément-Sorine electromechanical model of the heart was performed in the opensource platform SOFA[2] which allows modularity, interactivity and fast computation.
- To speed up the simulation, a new computational formulation of the finite element method for hyperelastic materials and linear elements is proposed and shows a great improvement in computation time for all the tested hyperelastic materials.
- In order to automatically initialize the mechanical parameters before regional personalization, a fast calibration algorithm is proposed and tested successfully on several healthy and pathological cases leading to a preliminary specificity study.
- We propose a new strategy for regional personalization based on the regional volumes to estimate the contractilities of all AHA zones for several pathological and healthy cases.

1.4.2 Organization of the thesis

The present manuscript is organized along the published and submitted work on which it is mainly based. It follows rather well the studies performed during this thesis in a chronological order: from the modelling of the heart to its personalization.

Chapter 2 describes the necessary steps that lead to an electromechanical model of the myocardium. We start by analyzing the available data (heathy and non healthy cases) and the preprocessing steps that enable to build the mesh, the fiber fields and the electrophysiology input. The complete Bestel-Clément-Sorine model that we used is then presented in

[2]SOFA is an opensource software for medical simulation available at http://www.sofa-framework.org/ (Faure et al., 2012)

details linking each equation to its physiological meaning. Most of this chapter was published in (Marchesseau et al., 2012a). During the course of this thesis we had the opportunity to gather three types of data: 17 heathy cases from which 8 were studied (the selection was made based on segmentation and registration results); 2 Left Bundle Branch Block Heart Failure cases acquired at King's college London with EnSite data and endocardial pressures; and 3 pathological cases acquired at INSERM institute (Rennes, France) selected for CRT (Cardiac Resynchronization Therapy). Table.1.1 summarizes the available data. We had at our disposal several tools to segment and register the image sequences as well as to create the mesh. All this enables to draw rich conclusions on the proposed methods.

Table 1.1: Available data for the studied patient and volunteer cases

Case	Numbers	cine-MRI	EnSite	Pressures
Volunteers from KCL	8	Yes	No	No
Patients from KCL	2	Yes	Yes	Yes
Patients from INSERM	3	Yes	Yes	No

Chapter 3 details our first contribution which consists in a new efficient implementation of the Bestel-Clément-Sorine model on an opensource interactive modular platform, based mainly on (Marchesseau et al., 2012a, 2010b) and (Faure et al., 2012). We use the SOFA platform for simulation which has many advantages. First, it leads to a fast computation, then it is a modular framework that allows to easily change the model for further improvements and finally it is well suited for interactive simulation. In this chapter, we first describe this simulation platform and its scenegraph data structure. Then we develop each component of the model and in particular the hyperelasticity which represents the passive part of the myocardium (and of any soft tissue). We propose an innovative method to compute hyperelastic materials that proved to increase efficiency in comparison to the standard Finite Element Method (Marchesseau et al., 2010b). Finally, we introduce the algorithm implemented to deal with the pressure inside the ventricles that replaces the fluid constraint in a more efficient way. Results of simulation show that the expected cardiac behavior is well recovered.

In Chapter 4 we propose an automatic calibration technique, published in (Marchesseau et al., 2012c) and further developed in (Marchesseau et al., 2012a,d). This method allows to estimate global values of the left ventricle mechanical parameters from indices of the volume and pressure curves using the Unscented Transform algorithm (Julier and Uhlmann, 1997). It computes the covariance matrix between the parameters and the observations and gives the best possible set of parameters to match given observations in one iteration. This calibration method shows good results for 7 healthy volunteers and two pathological cases leading to an estimation of pathological mechanical parameters versus control parameters. A comparison of these parameters leads to a preliminary specificity study that is in agreement with literature and medical knowledge.

Chapter 5 presents a new personalization strategy based on regional volumes, submitted in (Marchesseau et al., 2013a). This strategy extends the global calibration technique to regional contractility estimation using the Reduced Order Unscented Kalman Filtering (Moireau and Chapelle, 2011b). Using regional volumes allowing to smooth the registration imperfections, the proposed strategy shows good results for the studied pathological and volunteer cases. A comparison of the results for heart failures versus volunteers enables first conclusions on non-responders to CRT.

We conclude on the presented contributions and discuss perspectives in Chapter 6. Finally Appendix A gives the application of a numerical analysis technique proposed in Chapter 3 to the modelling of the liver deformation and published in (Marchesseau et al., 2010b). Details of the required calculations are also given in Appendix B and Appendix C.

Chapter 2

Electromechanical Modeling of the Heart

Contents

Based On: Marchesseau et al. (2012a) for the description of the model.

2.1 Introduction

The clinical understanding and treatment of cardiovascular diseases is highly complex. For each patient, cardiologists face issues in classifying the pathology, choosing the therapy or

selecting suitable patients. In order to provide additional guidance to cardiologists, many research groups are investigating the possibility to plan such therapies based on biophysical models of the heart (Kerckhoffs, 2010). The hypothesis is that one may combine anatomical and functional data to build patient-specific cardiac models that could have the potential to predict the benefits of different therapies. Cardiac electromechanical simulations are based on computational models that can represent the heart geometry, motion and electrophysiology patterns during a cardiac cycle with sufficient accuracy. Integration of anatomical, mechanical and electrophysiological information for a given subject is essential to build such models.

Several approaches for the past 20 years have been developed to describe and simulate the cardiac function, including cardiac mechanics and electrophysiology (Humphrey et al., 1990; Hunter et al., 1997; Nash, 1998; Bestel et al., 2001; Sachse, 2004). They differ in their choice of hyperelastic material, electrophysiological properties or electromechanical coupling. In this chapter the Bestel-Clément-Sorine (BCS) model (Bestel et al., 2001), further improved by Chapelle et al. (2012b) is developed. It showed good accuracy and predictive power under different pacing conditions in terms of haemodynamics (Sermesant et al., 2012), without being over-parametrized for the available data.

The following chapter details the available data and tools used before the mechanical modeling and personalization. Three different steps are needed before any mechanical personalization can be performed: extraction of the myocardium geometry, estimation of the patient's cardiac motion and personalization of the electrophysiological propagation.

2.2 Available Data

Our database is made of cardiac MRI data, including both SSFP sequence for anatomical description and cine-MRI for motion tracking. Three types of data were studied in this thesis: a set of volunteer data and a set of patient data acquired at the Division of Imaging Sciences & Biomedical Engineering at King's College London, UK and another set of patient data acquired at INSERM institute, Rennes, FRANCE, as part of studies that were ethically approved. Written informed consent was obtained from all human subjects and the studies were performed with all appropriate institutional human subjects approvals.

2.2.1 Volunteer Study from KCL

This study includes extensive multi-modality imaging of volunteers from which 8 healthy cases were used. All datasets consist of sequences of 4D cine-MRI with a spatial resolution of approximately $1.5\times1.5\times7\text{mm}^3$ and a temporal resolution of around 30 ms (30 images per cardiac cycle), that cover the ventricles entirely. Volunteers were aged 28 ± 5 years, without clinical history of cardiac diseases. This dataset was made available to the research community for the STACOM'2011 challenge, see (Tobon-Gomez et al., 2011) for details regarding the data acquisition of this study.

2.2.2 Patient Study from KCL

We also used here 2 pathological cases from a combined imaging and endocardial mapping study concerning patients selected for CRT (Ginks et al., 2011). They were both charac-

terized by a large QRS, due to a Left Bundle Branch Block (LBBB), and a small ejection fraction, due to the asynchronous contraction of the left ventricle. The first patient was a sixty year old woman with NYHA class III (NYHA classes stand for the stages of heart failure according to the New York Heart Association). The left ventricle ejection fraction was 25% and the patient suffered from significant mechanical dysynchrony, with a QRS duration of 154ms (normal QRS is less than 120ms). This patient is referred to as post myocardial infarction heart failure (post-MI HF). The second patient was also in NYHA class III heart failure, with a left ventricle ejection fraction of 18% and a QRS duration of 200ms. This patient suffered furthermore from severe dilated cardiomyopathy heart failure (DCM HF).

High quality cardiac anatomical and functional data were acquired with MRI, such as myocardial shape, wall motion and infarct sites, with a spatial resolution of approximately $1.5 \times 1.5 \times 7\,mm^3$ and a temporal resolution of around $30\,ms$. Electro-anatomical data was also obtained from catheter-based measurements that are guided using X-ray fluoroscopy with a spatial resolution of less than a centimeter and a temporal resolution close to a millisecond. Acute heamodynamic data was acquired using a high fidelity (200 Hz) pressure sensor to measure left ventricular pressure. This data was registered in space using the developed XMR registration (Rhode et al., 2005).

2.2.3 Patient Study from INSERM

Finally 3 heart failure cases acquired at INSERM institute were studied in this thesis. They were selected for Cardiac Resynchronization Therapy based on criteria from the New York Heart Association (NYHA) class III-IV. Patients had a small ejection fraction (EF) $< 35\%$ and a prolonged QRS on electrocardiogram $> 120ms$. The basal and follow-up of each patients showed that 1/3 patients was a non-responder to the CRT.

Data include cine-MRI and 3D SSFP images as well as EnSite data and electrocardiograms allowing a detailed electrophysiological study.

2.3 Geometry Personalization

To personalize the geometry from images, three methods were used depending on the data and the involved collaboration teams. During the first part of this thesis, the volunteer data was segmented using Philips automatic tool (Sec.2.3.2) and the two available pathological cases from KCL, using CardioViz3D semi-interactive tool (Sec.2.3.1). For the second part of this thesis, the same volunteer data and new cases acquired at INSERM were segmented using newly available segmentation tool GIMIAS (Sec.2.3.3).

2.3.1 Semi-interactive Segmentation

We combined a semi-interactive segmentation of the myocardium from the cine-MRI data at end-diastolic phase to create the 3D geometry using CardioViz3D[1], and a manual correction from the SSFP sequence to include the four valves (see Fig.2.1).

[1] CardioViz3D is an open source software for the processing, simulation and visualization of cardiac data. It is available at http://www-sop.inria.fr/asclepios/software/CardioViz3D/

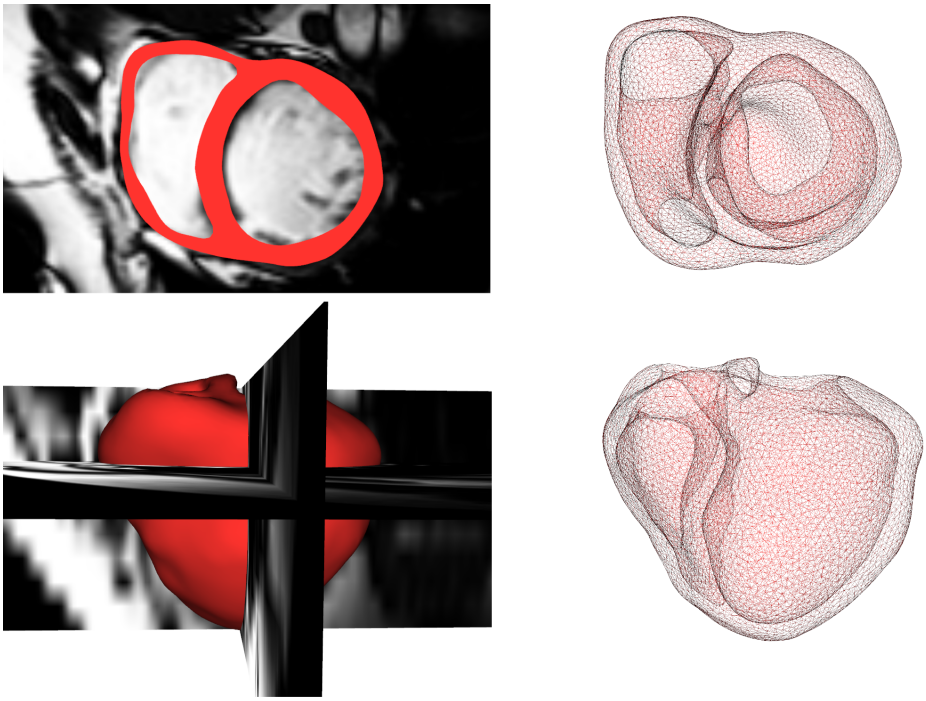

Figure 2.1: Segmented heart with the two ventricles and the four valves, generated from 3D MRI using Cardioviz3D.

2.3.2 Philips Automatic Cardiac Segmentation

Alternatively, we used Philips automatic cardiac segmentation (Ecabert et al., 2011) tool in GIMIAS [2] to extract the ventricles from the SSFP sequence (Fig. 2.2) and then recreate a binary mask of the myocardium. We then used CGAL[3] to create tetrahedral meshes.

2.3.3 GIMIAS Semi-automatic Segmentation

We extracted a biventricular anatomy from SSFP MRI datasets using the segmentation algorithm implemented in (Tobon-Gomez et al., 2012b). This technique is based on a deformable model and allows manual deformations if final corrections are needed. We generated a volumetric binary image from this biventricular surface. The Marching cubes algorithm (Lorensen and Cline, 1987) was then used to extract a polygonal surface. ReMesh (Attene and Falcidieno, 2006) enabled to smooth and ensure a manifold triangular mesh while Tetgen[4] and Netgen[5] generated the tetrahedral meshes (see Fig. 2.3).

2.3.4 Fibre Directions

In the electromechanical model presented in Section 2.6, fiber directions play an important role for both electrophysiological and mechanical simulations. There are several ways

[2] GIMIAS is a work flow-oriented environment focused on biomedical image computing and simulation (Larrabide et al., 2009)

[3] CGAL Computational Geometry Algorithms Library available at http://www.cgal.org

[4] http://tetgen.berlios.de

[5] http://www.hpfem.jku.at/netgen

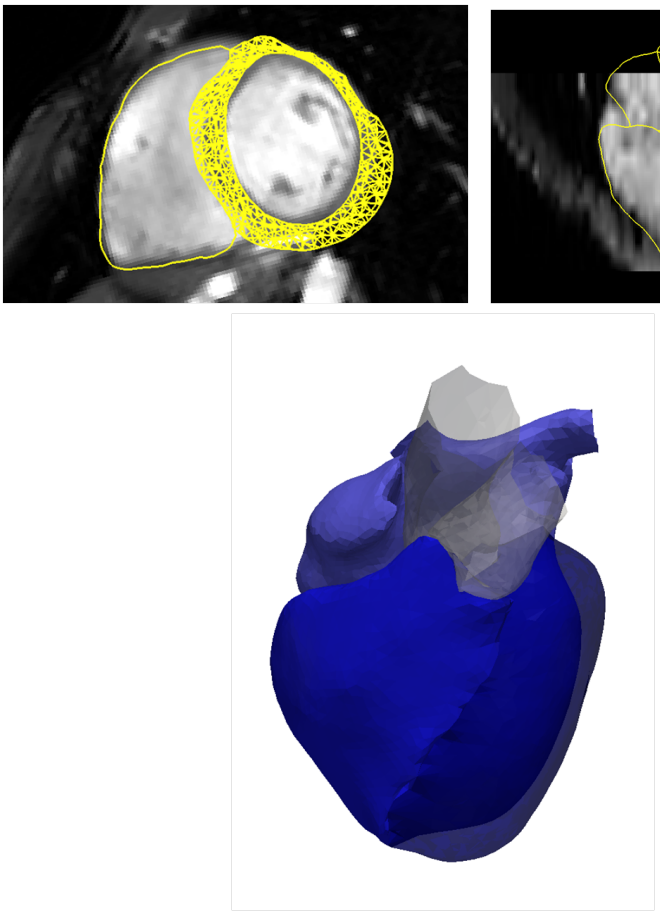

Figure 2.2: (Top) Segmented four-chambers heart generated automatically with Philips plugins. (Bottom) Resulting geometry.

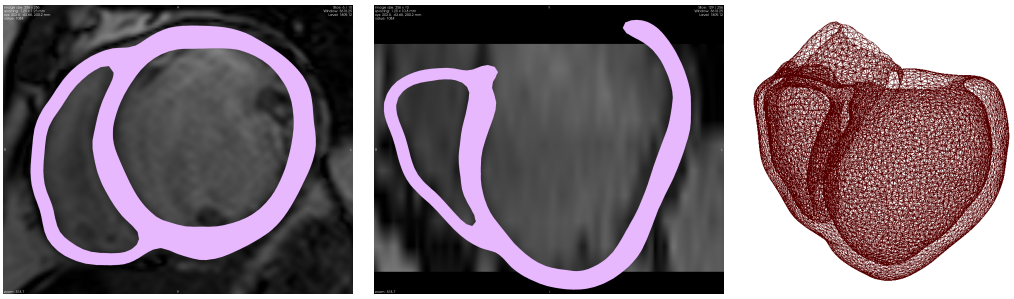

Figure 2.3: Modeling the anatomy of patient INSERM Case #1 (from left to right): extracting geometry from MR datasets, generating volumetric meshes.

to generate realistic fiber directions: by mapping an atlas onto the myocardium geometry (Peyrat et al., 2007; Lombaert et al., 2011; Toussaint et al., 2010) as shown on Fig. 2.4 or by synthetically varying the elevation angle (with respect to the short axis plane) across the myocardium wall. In this thesis, the fibers were created synthetically with angles varying from -70° on the epicardium to 0° at mid-wall to to +70° on the endocardium.

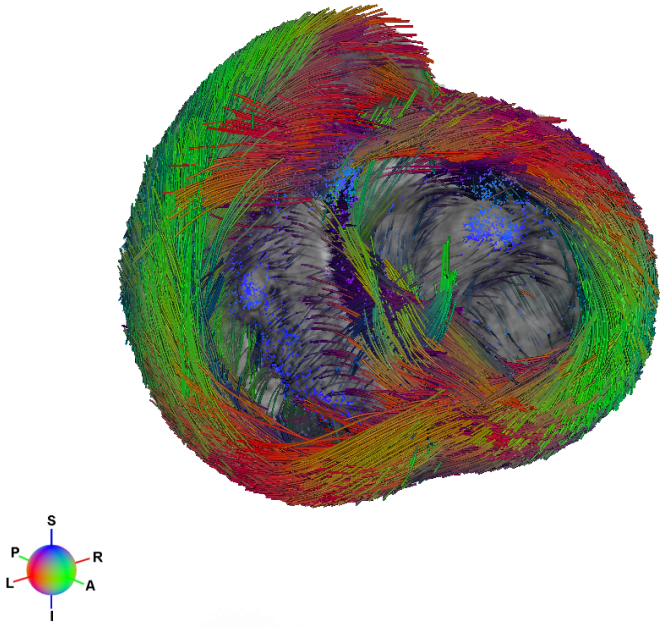

Figure 2.4: Representation of the fibers where the colors describe the orientation of the primary eigenvectors according to the color sphere, from (Peyrat et al., 2007).

2.4 Kinematic Personalization

To track the motion of the myocardium, two methods were used depending on the data and the collaborative teams. During the first part of this thesis, the volunteer data as well as KCL pathological cases were registered using the iLogDemons algorithm (Sec.2.4.1). For the second part of this thesis, the same volunteer data and new cases acquired at INSERM were registered using newly available TDFFD Registration tool (Sec.2.4.2).

2.4.1 iLogDemons Registration

A non-rigid registration algorithm was applied to the clinical 4D image sequences to find the deformation field between the end diastolic image and each subsequent image. We used the incompressible Log-Domain Demons (iLogDemons) developed by Mansi et al. (2011) which estimates a dense non linear transformation that best aligns a template image to a reference image. Moreover, it allows to recover some components of the twist motion of the myocardium by incorporating an elastic regularizer and incompressible constraint into the registration. Comparison of the resulting deformed mesh and the image is presented in Fig. 2.5.

2.4.2 TDFFD Registration

Alternativeley, we used the Time Diffeomorphic Free Form Deformation (TDFFD) algorithm, which has been tested on 3D US datasets (De Craene et al., 2012a) and 3D TAG MRI datasets (De Craene et al., 2012b). The TDFFD algorithm optimizes a 4D velocity field parametrized by B-Spline spatiotemporal kernels. With the transformation obtained from the registration, the static volumetric mesh was deformed and local or regional indices were

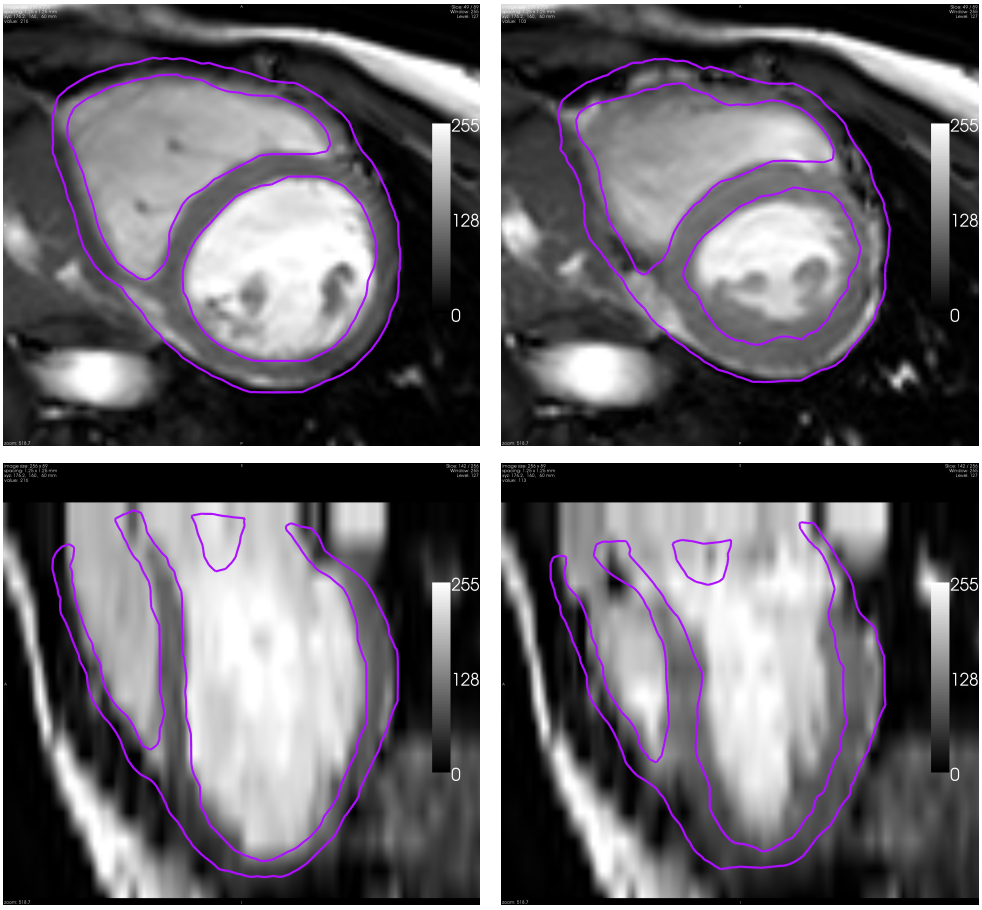

Figure 2.5: Comparison of the registration and the images at end-diastole and end-systole. (Top) Short axis view. (Bottom) Long axis view.

computed. Resulting deformed mesh is compared to the images in Fig. 2.6 at end-diastolic phase (frame used for the segmentation) and end-systolic phase.

2.5 Electrophysiology Personalization

2.5.1 Healthy volunteers

To simulate the electrophysiological pattern of activity, an Eikonal model was solved for the depolarization time T_d at each point of the mesh: $v\sqrt{\nabla T_d^t \mathbf{D} \nabla T_d} = 1$. v is the local electrical conduction velocity and $\mathbf{D} = (1-r)\mathbf{f} \otimes \mathbf{f} + r\mathbf{I}$ is the anisotropic conductivity tensor which depends on the fiber orientation $\mathbf{f}$ and on an anisotropic ratio r. The solution of this electrophysiological model was performed using Multi-Front Fast Marching Method (Sermesant et al., 2007).

For healthy cases, no subject specific electrophysiological data were acquired and therefore standard values were assumed (conduction velocity of 900mm/s and anisotropic ratio of 0.1), the personalization of this model requires to specify the onset of the electrical propagation (manually defined as areas corresponding to the extremities of the Purkinje network, on both endocardiums close to the apex). Fig. 2.7 shows the activation times after

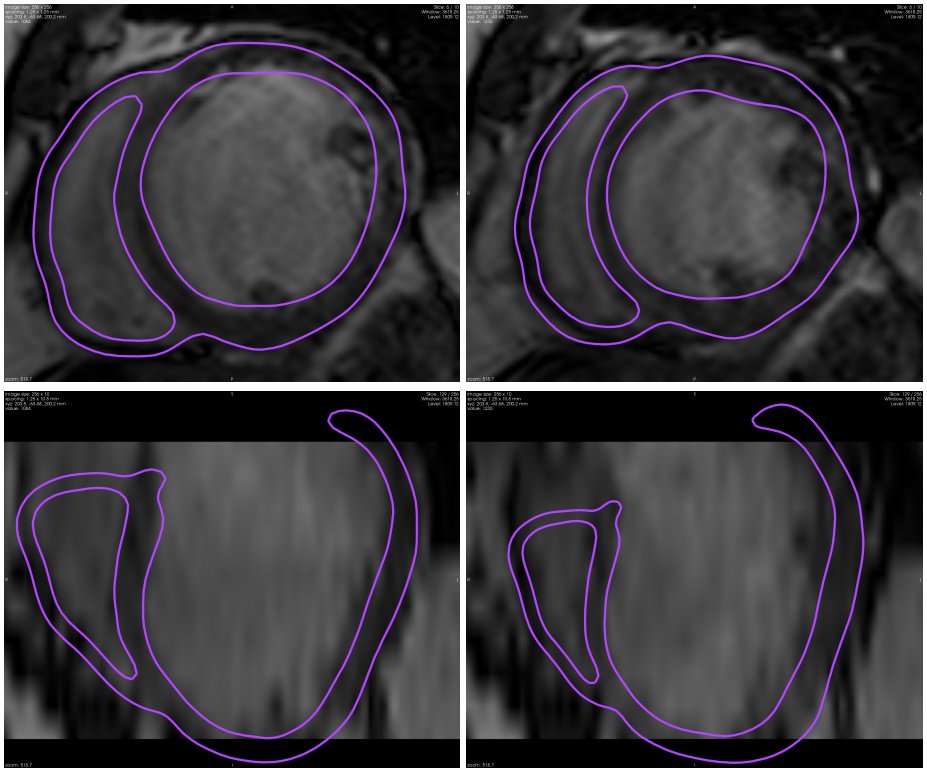

Figure 2.6: Estimation of the motion of patient Case #1 (from left to right): end-diastolic frame, end-systolic frame.

Purkinje propagation. The Action Potential Duration required for the mechanical simulation was calibrated from the volume curves at the same time as the mechanical parameters for the healthy cases.

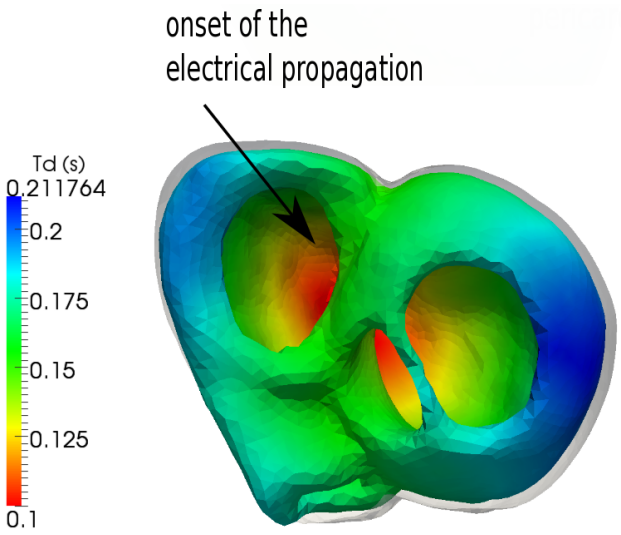

Figure 2.7: (Left) Electrophysiological and geometrical input.

2.5.2 Pathological Cases

For the two LBBB cases and the 3 INSERM cases, intracardiac non contact mappings allowed to estimate the onset of depolarization as well as electrical conductivities (Relan et al., 2011a). Two models are used for the personalization, the Eikonal model described previously and the Mitchell-Schaeffler biophysical model. While the Eikonal model simulated the propagation of the depolarization wave, the Mitchell-Schaeffler model represents the transmembrane potential as the sum of passive current and several active reactive currents. It is a simplified ionic model that allows reasonable computation times while giving good accuracy (Relan et al., 2011b). An example of personalized electrophysiology is given Fig. 2.8 (right) for a LBBB case (wave starting on the right ventricle) after registration and interpolation of the Ensite data available on the left ventricle see Fig. 2.8 (left).

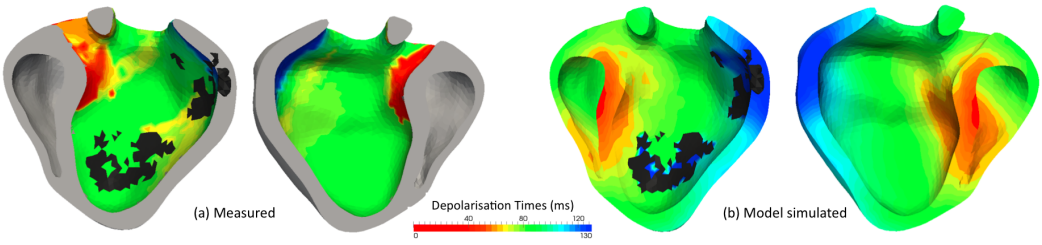

Figure 2.8: Measured (left) and Personalized (right) electrophysiology of a LBBB case from KCL.

2.6 The Bestel-Clement-Sorine Model

Our approach is based on the Bestel-Clément-Sorine (BCS) model (Bestel et al., 2001) further improved by Chapelle et al. (2012b). This choice is governed by some good properties of the BCS model: it is based on a multi-scale analysis, and is compatible with the laws of thermodynamics (balance of energy may be written), which is a useful property that leads to well-posed equations of motion (Krejci et al., 2006). We describe in this section, the modelling used to represent the mechanical behaviour of the heart.

2.6.1 Physiological Description

The myocardium is a multi-scale structure mainly composed of myocytes (muscular cell) and extracellular matrix. A myocyte is a fiber circumscribed by a membrane which encloses the sarcoplasm (fluid) and myofibrils. A myofibril is divided into compartments called sarcomeres separated by Z-discs. A sarcomere is composed of actin-myosin filaments in which the binding and unbinding process occurs to lead to the contraction.

At the organ level, the ventricles are filled with blood coming from the atria and ejected through the arteries, with valves ensuring the proper circulation. The closing and opening of these valves lead to four cardiac phases (filling, isovolumetric contraction, ejection and isovolumetric relaxation).

2.6.2 Hypotheses of the Model

In this section we list the different modelling hypotheses (in *italic font*) and the mathematical formulation used to represent them.

- The contraction of the sarcomere can be derived, at the molecular scale, from the Huxley filament model (Huxley, 1957) and takes into account the Starling effect.
Statistical mechanics allows to describe the contraction at the macroscopic scale, resulting in a differential equation modeling the control of the active stress τ_c and stiffness k_c by an electrical input u:

$$\begin{cases} \dot{k_c} = -(\mid u \mid +\alpha \mid \dot{e_c} \mid)k_c + n_0 k_0 \mid u \mid_+ \\ \dot{\tau_c} = -(\mid u \mid +\alpha \mid \dot{e_c} \mid)\tau_c + \dot{e_c} k_c + n_0 \sigma_0 \mid u \mid_+ \end{cases} \tag{2.1}$$

where α is a constant related to the cross-bridge unbinding due to the deformation rate, k_0 and σ_0 are respectively the maximum stiffness and contraction. n_0 is a reduction factor that allows to take into account *the Starling effect* by which the maximum contraction depends on the fiber strain e_c. The control variable u is derived from the electrical activation model and is a function of the free calcium concentration only. It is simplified here under the form of a function of time, by neglecting the variations in calcium dynamics (see Fig. 2.9):

$$\begin{cases} u(t) = k_{ATP} & \text{for } t \in [T_d,\ T_d + APD] \\ u(t) = -k_{RS} & \text{for } t \in [T_d + APD,\ T_r] \\ u(t) = 0 & \text{for } t \in [T_r,\ T_d + HP] \end{cases} \tag{2.2}$$

k_{ATP} is the rate of the myosin ATPase activity controlling the contraction rate and k_{RS} is the rate of sarcoplasmic reticulum calcium re-uptake controlling the relaxation rate. T_d and APD are respectively the depolarization time and the action potential duration (time during which the cell stays excited). T_d is obtained by a biophysical model of cardiac electrophysiology while the APD is calibrated from the volume curves. T_r is the time at which the active relaxation ends and the passive relaxation starts.

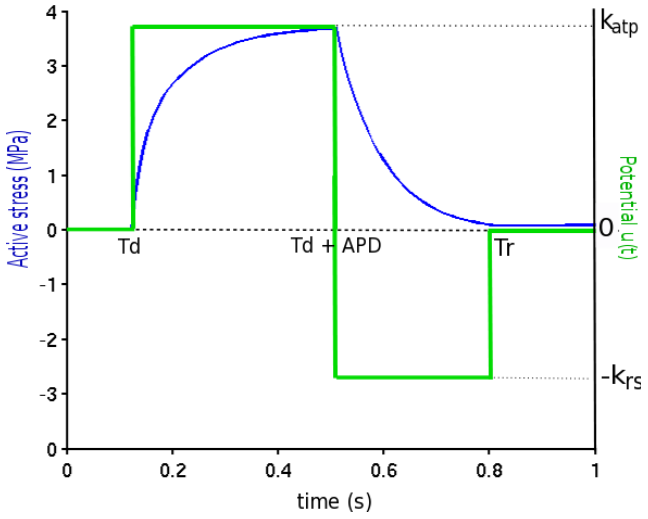

Figure 2.9: Active stress and potential over time

- The sliding of filaments creates friction in the sarcomere.
The contraction stress tensor σ_c is in parallel with a viscosity element (cf Fig. 2.10) which

gives $\sigma_c = \tau_c + \mu \dot{e}_c$.

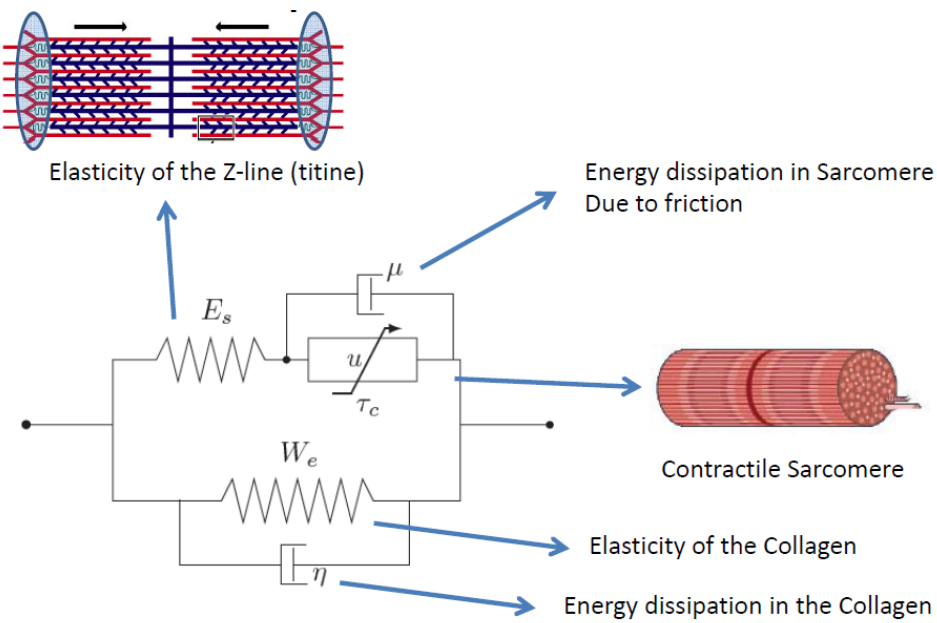

Figure 2.10: Full electromechanical model. W_e is the strain energy of the extracellular matrix considered here as an isotropic material, associated with a dissipative term η. u is a control variable which is driven by changes in transmembrane potential. It controls the contraction stress τ_c. μ deals with the friction in the sarcomere while E_s is a linear spring to enforce elasticity of the Z-discs (titin).

- The Z-discs present an elastic behaviour, which enables isometric contractions.
A linear elastic component having stress $\sigma_s = E_s e_s$ is in series with the contractile component. Therefore, after linearization of the equations presented by Chapelle et al. (2012b), $e_{1D} = e_s + e_c$ and $\sigma_c = \sigma_s$, where e_{1D} is the projection of the Green-Lagrange deformation tensor $\mathbf{E}$ on the fiber direction: $e_{1D} = \mathbf{f}^T \mathbf{E} \mathbf{f}$.

- The extracellular matrix presents a passive hyperelastic behaviour.
Several authors (Holzapfel and Ogden, 2009; Wong et al., 2008; Mazhari and McCulloch, 2000) consider the myocardium as a whole to have an orthotropic behaviour (such as the Costa's law (Costa et al., 2001)), taking into account both fiber and laminar sheets directions. In this thesis, we consider an isotropic behaviour described as a Mooney Rivlin material. Thus globally, adding the elasticity of the Z-discs, the passive behaviour of myocardial tissue in the BCS model is considered to be transversally anisotropic.

- The blood characteristics (flow, pressure) can be represented globally for each structure (atria, ventricles, arteries).
The basic circulation model is represented in Fig. 2.11 and defines the four phases of the cardiac cycle, independently for each ventricle as follows:

- Filling: when the left (right) ventricular pressure P_v is smaller than the left (right) atrial pressure P_{at}, the mitral (tricuspid) valve is open and the left (right) ventricle fills up with blood.

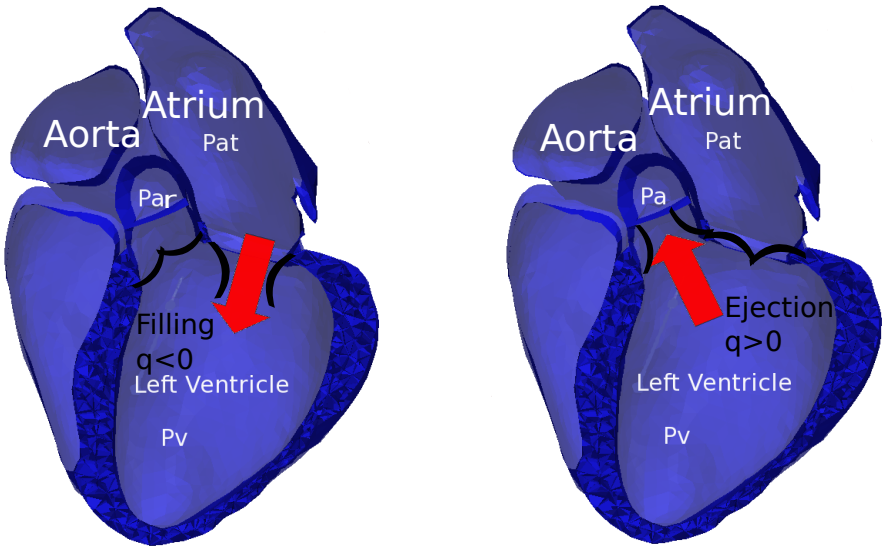

Figure 2.11: Circulation model: (Left) Filling phase. (Right) Ejection phase.

- Isovolumetric Contraction: after the contraction started, when the ventricular pressure reaches the atrial pressure, the mitral (tricuspid) valve close, therefore all valves are closed.

- Ejection: when the left (right) ventricular pressure reaches the arterial pressure, $P_v >$ P_{ar}, the aortic (pulmonary) valve opens and the blood is ejected from the ventricle.

- Isovolumetric Relaxation: after the relaxation started, when the left (right) ventricular pressure drops below the arterial pressure, the aortic (pulmonary) valve closes and therefore all valves are closed.

2.7 Discussion

The choice of this model to characterize the mechanical behaviour of the heart has been justified in several ways (as it will be explained in Chapters 3 and 4). First, the hypotheses that constitute the model are all physiologically relevant and do not input any *a priori* knowledge on the observations (for instance the pressure). Also, the model depends on only 14 global parameters from which 7 were easily tuned from global indices of the volume and pressure curves. The ratio between the number of sensitive parameters and the total number of parameters is therefore good, which confirms the quality of this model for such application. Moreover, tests on preload, afterload and inotropy changes demonstrated that the model behaves in agreement with literature in such conditions (Klabunde, 2011).

This work could be extended in several ways. For instance, fiber orientations which is important to model electrical and mechanical behaviors may be based on a registered human atlas built from DT-MRI (Lombaert et al., 2011) or from *in-vivo* patient specific imaging (Toussaint et al., 2010). Furthermore, the parameters of the registration algorithm could be optimized to better track the cardiac motion. An alternative for image registration is to use

a physically based model (Wong et al., 2010) which may include more *a priori* knowledge about the cardiac motion.

Chapter 3

Numerical Analysis of the BCS Model on SOFA

Contents

Based on: (Faure et al., 2012) for the description of SOFA and on the published paper (Marchesseau et al., 2012a) for the numerical analysis of the BCS Model in this framework. Moreover, section 3.3 is based on a published work (Marchesseau et al., 2010b) on soft tissue modelling applied to the liver deformation.

3.1 Introduction

Our simulations are based on the SOFA platform[1]. SOFA is an open-source framework targeted at real-time simulation with an emphasis on medical simulation, mainly developed at INRIA. A large choice of efficient solvers, hyperelastic or viscous material laws are already implemented in SOFA. Moreover, it enables interactivity during the simulation (pacing, surgery planning, ...) and gives a good trade-off between accuracy and computational efficiency.

The next section describes briefly the requirements to implement the electromechanical coupling in SOFA (based on (Faure et al., 2012)), and the following sections develop the components in more details (based on (Marchesseau et al., 2012a)). Finally the simulation results were published in (Marchesseau et al., 2012d), (Faure et al., 2012), (Marchesseau et al., 2012c) or (Talbot et al., 2012a).

3.2 Simulating the Heart in SOFA

SOFA (Simulation Open Framework Architecture) is an open-source C++ library made for interactive computational medical simulation (Faure et al., 2012). We decided to implement from scratch the BCS electromechanical model of the heart on this platform for its modularity and its efficiency in terms of accuracy, computation times and interactivity.

3.2.1 SOFA platform for simulation

SOFA enables complex dynamical system to be simulated by decomposing the systems into components (time integration solver, loader, linear solver, ...) designed independently and organized in a scenegraph data structure organised in nodes, subnodes and components linked in a XML architecture as presented Fig.3.1. Every dynamical system can be written with the dynamical equation:

$$\mathbf{M}\ddot{\mathbf{X}} + \mathbf{B}\dot{\mathbf{X}} + \mathbf{K}\mathbf{X} = \sum \mathbf{F}_i \tag{3.1}$$

where $\mathbf{M}$ is the mass matrix, $\mathbf{B}$ is the damping matrix, $\mathbf{K}$ is the stiffness matrix, $\mathbf{F}_i$ are some applied forces and $\mathbf{X}$ is the state variable.

In SOFA, each term of this equation is computed independently in various components. To illustrate this concept, Fig. 3.1 shows a SOFA scene that models the deformation of a snake. It contains, as in all SOFA scenes, a mesh loader, a mechanical object that contains the state variables, a topology component that gives information on the mesh (connectivity of the nodes, of the hexahedra or tetrahedra ...), some forcefields that build the right hand term of the dynamical equation and the stiffness matrix $\mathbf{K}$, a mass component to build the mass matrix $\mathbf{M}$, a time integration scheme to compute the dynamical equation at time $t+dt$ as a function of the dynamical equation at time t, and a linear solver to solve this discretized equation.

3.2.2 Simulating the Heart in SOFA

Cardiac mechanics is based on separated components: a passive part that deals with hyperelasticity and viscosity, an active part during the contraction and relaxation phases cor-

[1] http://www.sofa-framework.org

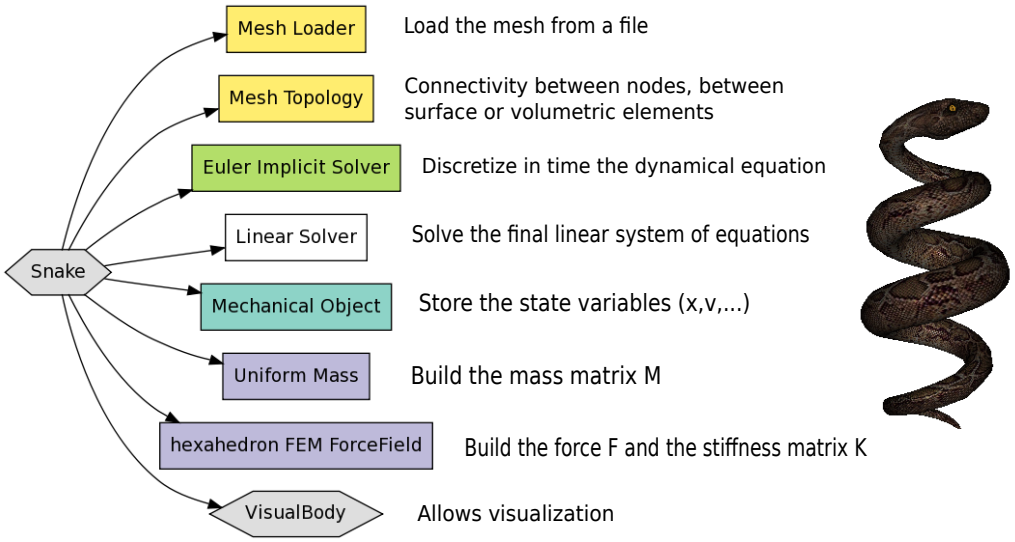

Figure 3.1: SOFA graph with the different components to simulate the complete model of the Snake.

responding to the binding and unbinding of the actin-myosin bridges in the sarcomeres, a valve model to represent the flow in the ventricles, and boundary conditions. All these components were implemented independently following the graph 3.2.

In this case, the passive part of the model is the hyperelastic forcefield *MooneyRivlin* (see Sec.3.3). The active part is more complex since it needs the solution of coupled ordinary differential equations in ContractionNode, which gives the stress tensor τ_c for each element of the mesh (see Sec.3.4 for detailed computation). This stress tensor is then input in *ContractionForceField* for the unidirectional coupling. The constraint due to the blood flow is implemented through the two *Pressure Constraint ForceField* and *Projective Pressure Constraint* components which apply forces in the endocardium due to blood pressure and projects the velocity field to satisfy the valve model (see Sec.3.5). As boundary conditions, first the base (and/or the apex) of the heart is attached with springs (*BaseConstraint*) which is equivalent to adding extra diagonal terms in the stiffness matrix of the basal nodes. Finally, efficient collision detection is implemented to prevent the surface of the myocardium to leave the pericardium (see Sec.3.6).

3.3 Passive Hyperelasticity: the MJED Method

An exponential hyperelastic material has been considered in (Chabiniok et al., 2011) instead of Mooney-Rivlin but with limited benefits due to its contraction behavior. Orthotropic materials may be introduced in the future by integrating recent work from Lombaert et al. (2011) which estimates the laminar sheets direction on human hearts.

Linear tetrahedral finite elements are used to discretize the strain energy describing the Mooney-Rivlin material. Instead of the classical Bubnov-Galerkin Finite Element Method (FEM) formulation, the energy is discretized with the MJED (Multiplicative Jacobian Energy Decomposition) technique published in (Marchesseau et al., 2010b) for its application to the liver motion under deformation (see Appendix A).

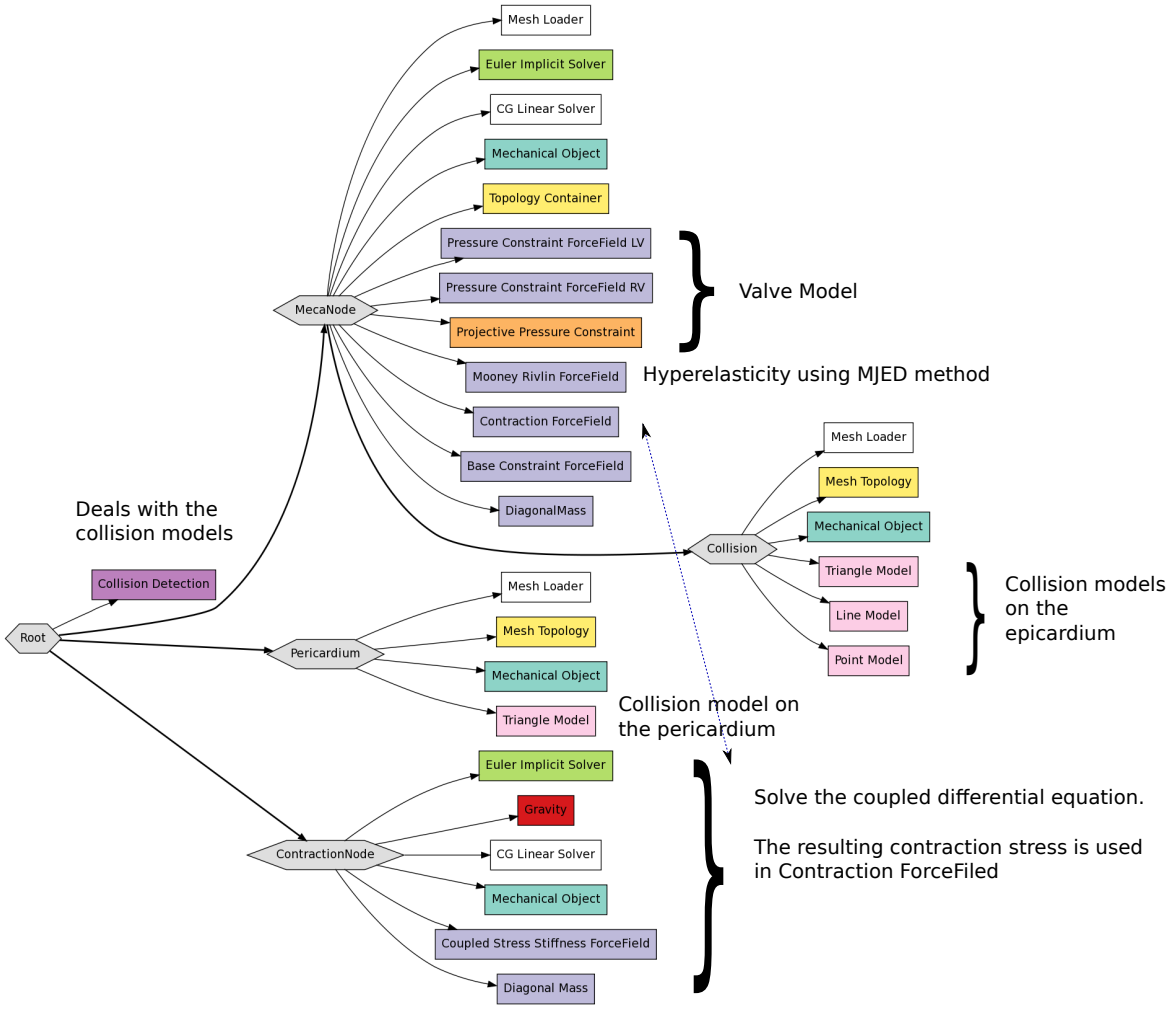

Figure 3.2: SOFA graph with the different components to simulate the complete model of the Heart

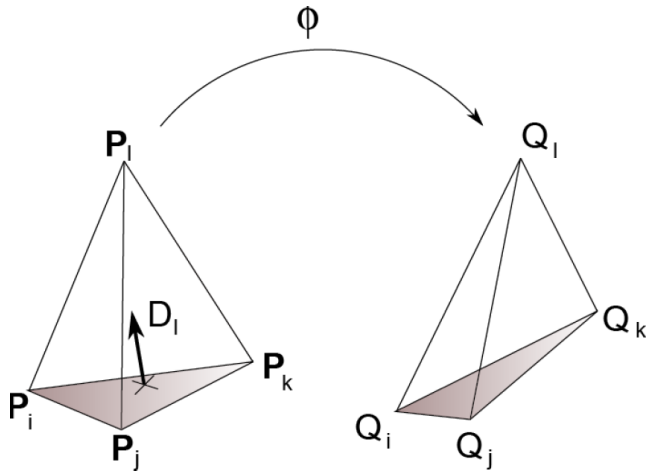

Figure 3.3: Notations for tetrahedral Finite Elements.

3.3.1 Fast computation of Hyperelastic Materials

Under large deformation, linear elasticity is no longer valid and the soft tissue behavior is better represented as an hyperelastic material. Since we are using implicit time integration schemes, it is necessary at each time step to compute hyperelastic forces and stiffness matrices with a discretization method. The Finite Element Method (FEM) is a widely used approach to this end, however the constraint of fast simulation is not always satisfied. The objective of this section is to introduce a fast discretization method suitable for all hyperelastic materials and to compare it with classical FEM. To discretize the geometry, we use tetrahedral linear finite elements because they are straightforward to generate from triangular surfaces that are outputted by image segmentation algorithms. Linear tetrahedral finite elements have some limitations since they can exhibit numerical locking when enforcing incompressibility (Joldes et al., 2009). Note also that all optimizations developed in this section can be easily extended to other elements in particular linear hexahedral elements since it is based on the gradient of shape functions.

In tetrahedral finite elements, T_P is the rest tetrahedron (with vertices P_i) which is transformed under the deformation function $\phi(X)$ into the tetrahedron T_Q (with vertices Q_i), as shown Fig.3.3. Any hyperelastic material is fully determined by its strain energy function W_h which describes the amount of energy necessary to deform the material. This strain energy function is defined in a way which is invariant to the application of rigid transformations: it involves the invariants of the *Cauchy-deformation tensor* defined as $\mathbf{C} = \nabla\phi^T\nabla\phi$. There are numerous invariants of $\mathbf{C}$ (see (Weiss et al., 1996) for detailed explanation) but the ones used for isotropic materials are the following: $I_1 = tr\mathbf{C}$, $I_2 = \frac{1}{2}((tr\mathbf{C})^2 - tr\mathbf{C}^2)$ and the Jacobian $J = det\nabla\phi$. We define furthermore the deviatoric deformation tensor $\bar{\mathbf{C}} = J^{-2/3}\mathbf{C}$, which by construction does not contain any volumetric dilation of the material but only pure deformation. Its first two invariants are written as $\bar{I}_1$ and $\bar{I}_2$.

FEM Discretization of Hyperelastic Materials on Linear Tetrahedra

One way to consider finite elements method, for instance as explained by Zienkiewicz and Taylor (2000), is to use the variational principle. The first variation of the strain energy is

expressed as

$$\delta W = \int_{\Omega} \delta \mathbf{E}_{IJ} \mathbf{S}_{IJ} dV$$

where

$$\mathbf{S}_{IJ} = 2\frac{\partial W}{\partial \mathbf{C}_{IJ}} = \frac{\partial W}{\partial \mathbf{E}_{IJ}}$$

is the second Piola-Kirchhoff (SPK) stress tensor and $\mathbf{E}$ is the Green-Lagrange strain tensor ($\mathbf{E} = 1/2(\mathbf{C} - \mathbf{Id})$). The SPK stress tensor and the Green-Lagrange strain tensor are energy conjugates of each other, similarly to force and displacement or torque and angle in other mechanical problems.

The discretization of those integrals on a tetrahedral mesh requires the definition of shape functions $\xi_i(X) \in \mathbb{R}$ for each point of tetrahedron T_p such that:

$$\begin{cases} \xi_i(P_j) = \delta_{ij} \\ \sum_i \xi_i(X) = 1 \\ \phi(X) = \sum_i \xi_i(X) Q_i \end{cases} \tag{3.2}$$

On a linear tetrahedron, the shape functions $\xi_i(X)$ can be interpreted as the barycentric coordinate of X in T_p and can be written as:

$$\xi_i(X) = \mathbf{D}_i \cdot X + \alpha_i$$

where $\mathbf{D}_i$ is called a *shape vector*. Shape vectors $\mathbf{D}_i = \nabla \xi_i$ are the gradient of the shape functions and only depend on the geometry of the rest tetrahedron T_p. The four shape vectors $\mathbf{D}_i$ in T_p have many remarkable properties among which they sum to zero (see definitions and properties in (Delingette, 2008)).

Since the Green-Lagrange strain tensor is symmetric, it can be represented as a 6×1 vector. Its variation can then be computed as:

$$\delta \mathbf{E} = \sum_i \hat{\mathbf{B}}_i \delta \tilde{u}_i$$

where $\tilde{u}_i$ is the nodal displacement and $\hat{\mathbf{B}}_i$ is the strain-displacement 6×3 matrix. The strain displacement matrix $\hat{\mathbf{B}}_i$ plays a major role in the classical formulation of FEM and its definition relies both on $\nabla \phi$ and $\mathbf{D}_i$. For instance, the nodal force $\mathbf{F}_i$ at a vertex of tetrahedron T_p can be computed as :

$$\mathbf{F}_i(T_p) = -\int_{T_p} \hat{\mathbf{B}}_i^T \, \mathbf{S} \, dV$$

Similarly, the stiffness matrix $\mathbf{K}_{ij}$ at an edge of tetrahedron T_p is formulated as :

$$\mathbf{K}_{ij} = \int_{T_p} \hat{\mathbf{B}}_i^T \hat{\mathbf{N}} \hat{\mathbf{B}}_j dV + \int_{T_p} \mathbf{D}_i^T \mathbf{S} \mathbf{D}_j \, dV$$

where $\hat{\mathbf{N}}$ is the 6×6 Voigt representation of the fourth order elasticity tensor given by $N_{IJKL} = 2\frac{\partial S_{IJ}}{\partial C_{KL}}$.

This discretization method has the advantage of being general. However, it has three limitations. First, the formulation and the computation of the SPK stress tensor $\mathbf{S}$ and the elasticity tensor $\hat{\mathbf{N}}$ can be fairly complex even for common hyperelastic materials such as Mooney-Rivlin for instance. One reason for this complexity is that the first and second

derivatives of $J = det\nabla\phi$ with respect to $\mathbf{C}$ are non trivial and involves the inversion of $\mathbf{C}$, e.g. $\frac{\partial J}{\partial \mathbf{C}} = \frac{1}{2}J\mathbf{C}^{-1}$. Since we use total Lagrangian method, this inversion needs to be done at each time step. This makes the expression of the derivatives of $\bar{I}_1$ and $\bar{I}_2$ particularly cumbersome and therefore computationally expensive to evaluate.

The second limitation is that the strain-displacement matrix $\hat{\mathbf{B}}_i$ combines two terms: the deformation gradient $\nabla\phi$ and the gradient of the shape functions $\mathbf{D}_i$. The former changes at each iteration while the latter is constant. For basic hyperelastic materials for which the elasticity tensor $\hat{\mathbf{N}}$ is constant (for instance St. Venant Kirchhoff materials), this is not optimal and a better choice would be to isolate the deformation gradient and to combine the shape vectors with the elasticity tensor.

The third limitation is that the classical FEM formulation of hyperelastic material cannot cope with flat ($J \equiv 0$) or even inverted tetrahedra ($J < 0$). Indeed, such deformation are non physical and do not represent a configuration managed in continuum mechanics. However, in interactive simulations, such cases of extreme compression can be met due to contact (penalty-based instead of being constraint based) with rigid objects or due to non-physical user-defined gestures. For instance, if the user-interface is not equipped with force-feedback, the tool controlled by the user can undergo non plausible trajectories. To improve robustness in theses cases, it is important to propose a formulation for hyperelastic materials which can handle nearly flat tetrahedra.

Multiplicative Jacobian Energy Decomposition (MJED)

Our original discretization method addresses the three limitations of classical FEM. It consists of three separate contributions:

i) Decomposition of strain energy

Our approach is to decouple in the strain energy, the invariants of $\mathbf{C}$ from J so as to avoid matrix inversions and complex derivative expressions. Instead of computing the force and stiffness matrix using the first and second derivative of the energy with respect to $\mathbf{C}$ (leading respectively to $\mathbf{S}$ and $\hat{\mathbf{N}}$), we compute them directly by deriving the energy with respect to the nodal position:

$$F_i = -\left(\frac{\partial W_h}{\partial Q_i}\right)^T \text{ and } \mathbf{K}_{ij} = \left(\frac{\partial^2 W_h}{\partial Q_j \partial Q_i}\right) \tag{3.3}$$

where W_h is the strain energy. It is important to note that the approach developed in this section is completely equivalent to the classical FEM one but leads to more efficient computation.

We propose to write the strain energy functions as a sum of terms

$$W_h^k = f^k(J)g^k(\tilde{I})$$

or its exponential, where $\tilde{I} = (I_1, I_2, I_4...)$. Therefore g^k is independent of J, its derivative will not involve any matrix inversions. This decomposition applies to every studied case (Boyce Arruda (Arruda and Boyce, 1993), Mooney-Rivlin (Mooney, 1940; Rivlin, 1948), Veronda Westmann (Veronda and Westmann, 1970), Neo Hookean, St Venant Kirchhoff and Ogden (Ogden, 1972)). That gives for instance

$$W_h = V_0 \sum_{k=1}^{n} f^k(J)g^k(\tilde{I}) + V_0\, exp\left(\sum_{k=n+1}^{n'} f^k(J)g^k(\tilde{I})\right) \tag{3.4}$$

Exponential terms here account for models such as Costa's or Veronda Westmann's, the following calculations are made only for non exponential terms. Note moreover that laws such as Costa (Costa et al., 2001), Hunter (Hunter et al., 1997) or Holzapfel (Holzapfel et al., 2000) which do not dependent on the invariants of $\mathbf{C}$ but directly on components of $\mathbf{E}$ can also be considered (see Appendix B.4).

Using this decomposition of strain energy enables complex material formulation to be computed more efficiently with only a sum of reasonably simple terms and no matrix inversions. Once the decomposition is done, getting $f^{k'}(J)$ requires a 1D derivation, and getting

$$\mathbf{S}_h^k = 2\frac{\partial g^k(\tilde{I})}{\partial \mathbf{C}}$$

requires to combine well-known derivatives of the invariants (such as $\frac{\partial I_1}{\partial \mathbf{C}} = \mathbf{Id}$ or $\frac{\partial I_2}{\partial \mathbf{C}} = \mathbf{Id} I_1 - \mathbf{C}$ where $\mathbf{Id}$ is the 3×3 identity matrix). The full derivation, explained in Appendix B, gives

$$F_{h,i} = -V_0 \sum_{k=1}^{n} \left(f^{k'}(J) g^k(\tilde{I}) \left(\frac{\partial J}{\partial Q_i}\right)^T + f^k(J) \nabla\phi \, \mathbf{S}_h^k \, D_i \right)$$

where the derivative of the Jacobian is expressed as

$$\frac{\partial J}{\partial Q_i} = \frac{1}{6V_0}((Q_j - Q_l) \wedge (Q_k - Q_l))^T$$

ii) Formulation of the stiffness matrix

Implicit time integration schemes require the computation of the tangent stiffness matrix at each time step. This naturally involves elasticity tensors computed as the derivative of $\mathbf{S}_h^k$ with respect to $\mathbf{C}$ for each tetrahedron and at each time step. MJED leads to far simpler expressions of those tensors because $\mathbf{S}_h^k$ is independent of J. Furthermore, in many common materials, we show that the term containing those elasticity tensors can be precomputed. The full expression of the stiffness matrix includes 6 terms that are detailed in Appendix B. We only focus below on the term involving the elasticity tensor:

$$\mathbf{R}^k = f^k(J) \left(\frac{\partial \mathbf{S}_h^k}{\partial Q_j} D_i\right)^T \nabla\phi^T$$

which requires the computation of the tensor $\frac{\partial \mathbf{S}_h^k}{\partial \mathbf{C}} : \mathbf{H}$ where $\mathbf{H}$ is a symmetric matrix. In all cases, this tensor can be written as a sum of two kinds of terms,

$$\beta_1^k \, \mathbf{A}_1^k \, \mathbf{H} \, \mathbf{A}_1^k \text{ or } \beta_2^k \, (\mathbf{H} : \mathbf{A}_2^k) \, \mathbf{A}_2^k$$

where β_u^k are scalars, $\mathbf{A}_u^k$ are symmetric matrices, and $\mathbf{A} : \mathbf{B} = tr(\mathbf{B}^T\mathbf{A})$ for any two matrices $\mathbf{A}, \mathbf{B}$. Therefore, the term $\mathbf{R}^k$ is a combination of two terms:

$$f^k(J) \, \nabla\phi \, \mathbf{L}_1^k(i,j) \, \nabla\phi^T \text{ and } f^k(J) \, \nabla\phi \, \mathbf{L}_2^k(i,j) \, \nabla\phi^T$$

where $\mathbf{L}_1^k(i,j)$ and $\mathbf{L}_2^k(i,j)$ are linear matrices depending on the shape vectors D_i, D_j, the matrices $\mathbf{A}_u^k$ and the scalars β_u^k.

This formulation leads to an optimization for the assembly of the stiffness matrix for two reasons. First, no fourth order tensors (often implemented as 6×6 matrices) are required, only scalars and symmetric matrices are involved in the computation. Second, except for the Ogden model, the matrices $\mathbf{A}_i^k$ are constant and therefore matrices $\mathbf{L}_1^k(i,j)$ and

$\mathbf{L}_2^k(i,j)$ can be precomputed for each tetrahedron before the simulation. Both features decrease the number of operations required (additions and multiplications).

iii) Coping with highly compressed elements
When tetrahedra are nearly flat, $1/J$ would normally tends to infinity. To avoid numerical instabilities while computing the force, the value of J was thresholded. However, the volumetric terms $f^k(J)$ in the strain energy still become dominant. This makes the stiffness matrix singular and thus leads to numerically unstable computations because there is an infinite number of deformed configurations leading to the same value of J. In order to cope with this, Teran et al. (2005) perform an SVD decomposition of the deformation gradient matrix. To avoid this computationally expensive decomposition, we propose instead to *regularize* the term

$$\mathbf{G}_h^k = f^{k''}(J)\, g^k(\tilde{I})\, \frac{\partial J}{\partial Q_j} \otimes \frac{\partial J}{\partial Q_i}$$

by replacing it with the following expression :

$$\mathbf{G}_h^k = f^{k''}(J) g^k(\tilde{I}) \left((1-h) \frac{\partial J}{\partial Q_j} \otimes \frac{\partial J}{\partial Q_i} + \frac{1}{3} h \frac{\partial J}{\partial Q_j} \cdot \frac{\partial J}{\partial Q_i} \mathbf{Id} \right)$$

The closer h is to 1, the closer the $\mathbf{G}_h^k$ matrix is to a diagonal matrix. In practice, we set $h = (1-J)$ if $0 \leq J \leq 1$, $h = 0$ if $J \geq 1$ and $h = 1$ if $J \leq 0$. In all cases, the trace of the regularized matrix is equal to the trace of the original matrix. By only regularizing the stiffness matrix, we still minimize the strain energy and therefore do not change the nature of the hyperelastic material. With this technique, it is even possible to handle inverted elements when the strain energy remains finite as $J = 0$.

3.3.2 Testing accuracy and computation time of the hyperelastic implementation

Decreasing computation time of the assembly of the stiffness matrix and force vector is essential to reach real-time simulation as this represents around 45% of the total time needed in one step for a simple mechanical model. Therefore we first compared our implementation with the classical FEM method explained in (Zienkiewicz and Taylor, 2000), referred to as "Standard FEM", both implemented in SOFA. The results are given in Figure 3.4. We measured the time elapsed for the computation of the nodal forces and the stiffness matrices averaged over 100 iterations. We simulated the deformation of a cube with 20 700 tetrahedra and 4300 nodes. For all modes implemented the proposed strategy is definitely more efficient than the standard FEM, up to five times as fast for St Venant Kirchhoff material.

Second, two sets of comparisons have been made to check the accuracy of the MJED. A first set of tests compares the node positions after a specified deformation between our simulation and the Open Source software FEBio (version 1.1.7)[2] where several elastic and hyperelastic materials are implemented. The mean relative difference is around 10^{-6} for every models tested.

A second set of tests has been performed with the analytical solution of a deformed cube on which a vertical pressure p is applied on its top face. To this end, we assume that

[2]FEBio is an opensource software package for FE analysis available at mrl.sci.utah.edu

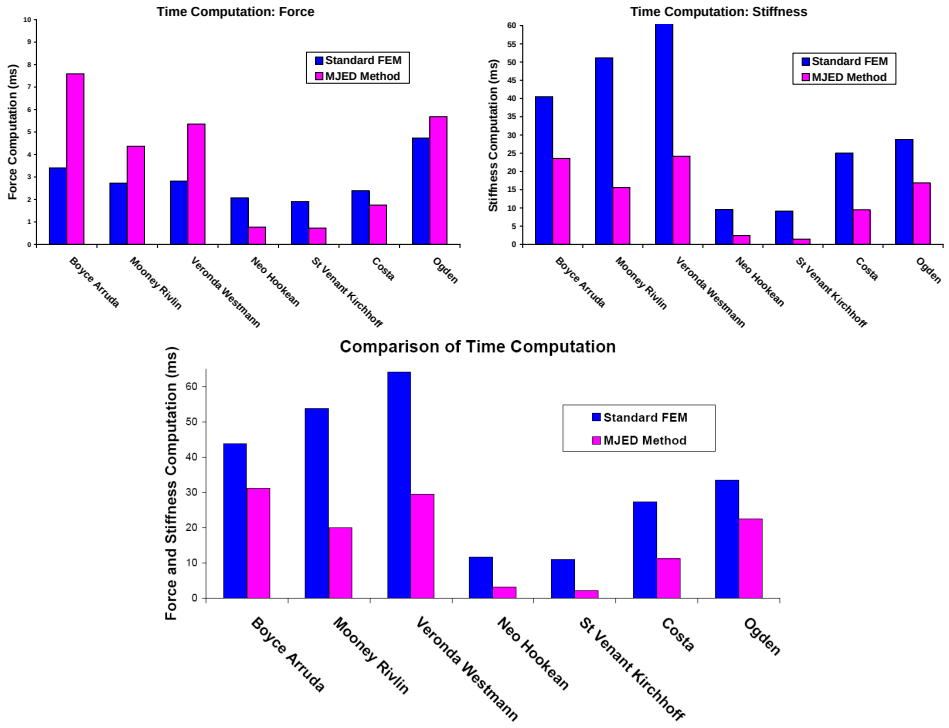

Figure 3.4: (Top) Comparison of the computation times of nodal forces and stiffness matrices between two different discretization methods averaged over 100 iterations. (Bottom) Total computation times.

the deformation gradient in the global x-y-z coordinate system is $\nabla\phi = diag(\alpha,\beta,\gamma)$. The simulated values of α,β,γ are compared to analytical solutions of the system:

$$\begin{cases} e_z^T\ \nabla\phi\ \mathbf{S}_h\ e_z &= p \\ e_x^T\ \nabla\phi\ \mathbf{S}_h\ e_x &= 0 \\ e_y^T\ \nabla\phi\ \mathbf{S}_h\ e_y &= 0 \end{cases}$$

Figure 3.5 shows the results in the non-linear domain, for St Venant Kirchhoff materials.

It can be seen that the computed results are very close to the analytic tests, the mean difference for St Venant Kirchhoff on each constants is of order 10^{-4} in the linear domain and 10^{-2} for larger pressure. For Costa's law, the mean difference is of order 10^{-8} in the linear domain and 10^{-4} for larger pressure.

To conclude, with those two sets of tests, we have validated the accuracy of the MJED method for hyperelastic materials. Moreover a mesh convergence study, with St Venant Kirchhoff material, has been performed to evaluate the trade-off between accuracy and speed on several meshes. It appeared that refining the mesh by multiplying the number of tetrahedra by 20 results in increasing the accuracy by 1% but dividing the number of frames per second by almost 10. Therefore a compromise has to be found to allow realistic interactions.

In the cardiac electromechanical model, which undergoes large deformation, the use of the MJED method is justified for the Mooney-Rivlin hyperelasticity which is used to

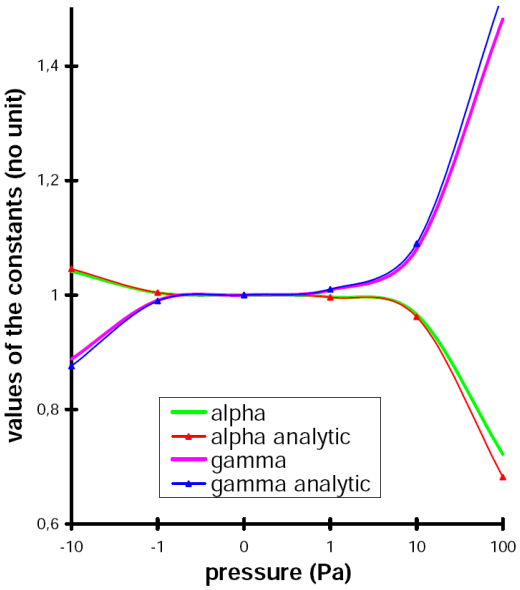

Figure 3.5: Analytical and computed results for α and γ for several pressures, with a log-scale, on St Venant Kirchhoff elasticity

represent the passive behaviour of the myocardium. It obeys the strain energy function:

$$W_e = c_1(\bar{I}_1 - 3) + c_2(\bar{I}_2 - 3) + \frac{K}{2}(J-1)^2 \tag{3.5}$$

where c_1, c_2 are material parameters and K is the Bulk modulus. This strain energy can then we written using the MJED method.

3.4 Active Contraction

As described in Sec. 2.6.2 a differential equation controls the active stress τ_c and the sarcomere stiffness k_c:

$$\begin{cases} \dot{k_c} = -(\mid u \mid + \alpha \mid \dot{e_c} \mid)k_c + n_0 k_0 \mid u \mid_+ \\ \dot{\tau_c} = -(\mid u \mid + \alpha \mid \dot{e_c} \mid)\tau_c + \dot{e_c} k_c + n_0 \sigma_0 \mid u \mid_+ \end{cases} \tag{3.6}$$

3.4.1 Resolution of the differential equation

To solve these coupled equations, we reformulate into

$$\dot{\mathbf{X}} = \begin{pmatrix} -r & \dot{e}_c^n \\ 0 & -r \end{pmatrix} \mathbf{X} + n_0 \mid u \mid_+ \begin{pmatrix} \sigma_0 \\ k_0 \end{pmatrix}$$

where $\mathbf{X} = (\tau_c, k_c)$, $r = (\mid u \mid + \alpha \mid \dot{e}_c^n \mid)$. This is solved using Euler Implicit Solver for instance, and it gives at each time step the couple (τ_c^n, k_c^n). A coupling with the mechanical object in needed to obtain the deformation and compute $\dot{e}_c^n = \frac{e_c^n - e_c^{n-1}}{\Delta t}$.

3.4.2 Contraction Force

The contraction stress at each time step $\sigma_c^n = E_s(e_{1D}^n - e_c^n)$ is given easily once we have e_c^n. Since $\sigma_c = E_s(e_{1D} - e_c) = \tau_c + \mu \dot{e}_c$, we obtain a recursive equation for e_c^n:

$$e_c^{n+1} = \frac{\Delta t E_s}{\mu} e_{1D}^n + \left(1 - \frac{\Delta t E_s}{\mu}\right) e_c^n - \frac{\Delta t}{\mu} \tau_c^n$$

where τ_c^n is given by solving the coupled equations. Therefore we determine the applied force and stiffness using the Total Lagrangian approach of the Finite Elements Method (Delingette and Ayache, 2004). The contraction force $\mathbf{F}_i$ on each deformed vertex $\mathbf{Q}_i$ and the stiffness matrix $\mathbf{K}_{ij}$ on each edge are given by:

$$\mathbf{F}_i = -\frac{1}{4} \nabla\phi \sigma_c (\mathbf{f} \otimes \mathbf{f}) \mathbf{D}_i$$

and

$$\mathbf{K}_{ij} = \frac{\sigma_c}{4} \mathbf{Id} (\mathbf{D}_j^T \mathbf{f} \otimes \mathbf{f}\, \mathbf{D}_i) + \frac{\partial \sigma_c}{\partial \mathbf{Q}_j} \mathbf{D}_i^T \mathbf{f} \otimes \mathbf{f}\, \nabla\phi^T$$

where $\mathbf{f}$ is the fiber direction and $\mathbf{D}_i$ is a shape vector at initial vertex $\mathbf{P}_i$.

We need to differentiate the contraction stress with respect to the nodal point. We start with the definition of the contraction stress $\sigma_c = E_s(e_{1D} - e_c)$ and $e_{1D} = \mathbf{f}^T \mathbf{E} \mathbf{f}$. The Green-Lagrange deformation tensor can be written

$$\mathbf{E} = -\frac{1}{4} \sum_k \sum_{l \neq k} (\|\mathbf{Q}_k - \mathbf{Q}_l\|^2 - \|\mathbf{P}_k - \mathbf{P}_l\|^2)(\mathbf{D}_k \otimes \mathbf{D}_l + \mathbf{D}_l \otimes \mathbf{D}_k)$$

$$e_{1D} = -\frac{1}{2} \sum_{l \neq k} \|\mathbf{Q}_k - \mathbf{Q}_l\|^2 (\mathbf{f}^T \mathbf{D}_k \mathbf{D}_l^T \mathbf{f}) + \|\mathbf{P}_k - \mathbf{P}_l\|^2 (\mathbf{f}^T \mathbf{D}_k \mathbf{D}_l^T \mathbf{f})$$

$$\frac{\partial e_{1D}}{\partial \mathbf{Q}_j} = -\sum_{i \neq j} (\mathbf{Q}_j - \mathbf{Q}_i) \mathbf{D}_i^T \mathbf{f}\, \mathbf{D}_j^T \mathbf{f}$$

Using the definitions of the deformation gradient $\nabla\phi = \sum_i \mathbf{Q}_i \mathbf{D}_i^T$ and the fact that $\sum_{i=1}^4 \mathbf{D}_i = 0$, we rewrite the last equation into:

$$\frac{\partial e_{1D}}{\partial \mathbf{Q}_j} = \mathbf{Q}_j (-\sum_{i \neq j} \mathbf{D}_i^T) \mathbf{f}\, \mathbf{D}_j^T \mathbf{f} + (\sum_{i \neq j} \mathbf{Q}_i \mathbf{D}_i^T) \mathbf{f}\, \mathbf{D}_j^T \mathbf{f} = \nabla\phi \mathbf{f}\, \mathbf{D}_j^T \mathbf{f}$$

Therefore

$$\frac{\partial \sigma_c}{\partial \mathbf{Q}_j} = E_s \nabla\phi \mathbf{f}\, \mathbf{D}_j^T \mathbf{f}$$

3.5 Modeling the Four Cardiac Phases

The ventricles are filled with blood coming from the atria and ejected through the arteries. We represent the four phases of the cardiac cycle, independently for each ventricle as follows:

- *Filling*: while the ventricular pressure (P_v) is below the atrium pressure (P_{at}), the mitral (or tricuspid) valve is open and the ventricle fills up with blood.

- *Isovolumetric Contraction*: the contraction starts and all valves are closed.
- *Ejection*: when $P_v > P_{ar}$ the arterial pressure, the aortic (or pulmonary) valve opens and the blood is ejected from the ventricle.
- *Isovolumetric Relaxation*: the relaxation starts and all valves are closed.

3.5.1 The Heamodynamic Model

To model those phases we apply the heamodynamic model introduced by Chapelle et al. (2012b). It gives a relation between the blood flow leaving the ventricle (q) and the atrial, ventricular and aortic pressures:

$$q = \begin{cases} K_{at}(P_v - P_{at}) & \text{for } P_v \leq P_{at} \\ K_{iso}(P_v - P_{at}) & \text{for } P_{at} < P_v \leq P_{ar} \\ K_{ar}(P_v - P_{ar}) + K_{iso}(P_{ar} - P_{at}) & \text{for } P_v > P_{ar} \end{cases} \tag{3.7}$$

where K_{at} and K_{ar} correspond to linear laws and K_{iso} relaxes the usual isovolumetric constraint ($q = 0$). With this definition, K_{iso} is much smaller than K_{at} and K_{ar}. The aortic pressure is computed following the fourth-element Windkessel model. Windkessel model depends on four parameters: the peripheral resistance R_p, the characteristic time τ, the characteristic resistance Z_c and the total arteria inertance L. The initial and asymptotic arterial pressures also influence the model. The atrial pressure is computed analytically as two sigmoids and depends on an initial and a maximum pressure that is set from the literature (Schäffler and Schmidt, 1999). The sigmoids start during the relaxation and finish before the beginning of the next contraction. An adjustment is set *a posteriori* to fit the volume or pressure curves.

3.5.2 Enforcing the Constraint to the Mechanical Model

The proposed heamodynamic model can be seen as a constraint on the volume (for each ventricle) since $q = -\frac{\Delta V}{\Delta t}$. It can be written $\mathbf{G}^T \Delta \mathbf{u} = \Delta \mathbf{V}$ where $\mathbf{u}$ are the nodal positions and $\mathbf{V} = [V_L, V_R]$ is the volume of the ventricles (see Appendix C). To enforce such a constraint to the dynamical system

$$\mathbf{K_u} \Delta \mathbf{u} = \mathbf{F_u}$$

where $\mathbf{K_u}$ and $\mathbf{F_u}$ are respectively the stiffness and external forces, the most common way is to use the Lagrangian Multipliers leading to the new system:

$$\begin{bmatrix} \mathbf{K_u} & \mathbf{G}^T \\ \mathbf{G} & \mathbf{0} \end{bmatrix} \begin{bmatrix} \Delta \mathbf{u} \\ \lambda \end{bmatrix} = \begin{bmatrix} \mathbf{F_u} \\ \Delta \mathbf{V} \end{bmatrix}$$

However, the unconstrained dynamical system that we intend to solve in our model is written $\mathbf{K} \Delta \mathbf{s} = \mathbf{F}$ where $\mathbf{s}$ are the unknown nodal velocities, which forces use to rewrite the constraint using the nodal velocities. First, knowing that $q = -\frac{\Delta V}{\Delta t}$ and $\frac{\Delta V}{\Delta t} = \mathbf{G}^T(\Delta \mathbf{s}^{t+\Delta t} + \mathbf{s}^t)$, the constraint becomes

$$\mathbf{G} \Delta \mathbf{s} + \mathbf{D} \mathbf{P_v} = \mathbf{F_D} \tag{3.8}$$

where $\mathbf{F}_D = [F_{DL}, F_{DR}]$ and $\mathbf{D} = [D_L, D_R]$ are set for each phase (using eq(3.7)).

- *Filling Phase*: $q = K_{at}(P_v - P_{at})$ gives

$$\begin{cases} D = K_{at} \\ F_D = K_{at} P_{at}^{t+\Delta t} - \mathbf{G}^T \mathbf{s}^t \end{cases}$$

- *Isovolumetric Phases*: $q = K_{iso}(P_v - P_{at})$ gives

$$\begin{cases} D = K_{iso} \\ F_D = K_{iso} P_{at}^{t+\Delta t} - \mathbf{G}^T \mathbf{s}^t \end{cases}$$

For those two phases we need to know $P_{at}^{t+\Delta t}$ which is modeled as two sigmoids following Billet's description (Billet, 2010).

- *Ejection Phase*: $q = K_{ar}(P_v - P_{ar}) + K_{iso}(P_{ar} - P_{at})$

We need to estimate $P_{ar}^{t+\Delta t}$. To this end, we can use several Windkessel models (two, three, or four elements). The method to derive the constraint equation is the same for each of them, hence we only describe here the technique for the four-element Windkessel model which is the most accurate but complex one. The four-element Windkessel equation relates the pressure of the aorta P_{ar} (or pulmonary vein) to the flow and its first two derivatives:

$$R_p C \dot{P_{ar}} + P_{ar} - P_{ve} = (R_p + Z_c)q + (R_p Z_c C + L)\dot{q} + L R_p C \ddot{q} \tag{3.9}$$

with P_{ve} the venous pressure, R_p the peripheral resistance, C the total arterial compliance, Z_c the characteristic impedance, and L the total arterial inertance ($L = 0$ reduces the equation to the three-element Windkessel). We denote $\tau = R_p C$ the characteristic time. We use Euler Implicit integration scheme, therefore

$$\dot{q} = \frac{q^{t+\Delta t} - q^t}{\Delta t} \, , \dot{P_{ar}} = \frac{P_{ar}^{t+\Delta t} - P_{ar}^t}{\Delta t}$$

$$\text{and } \ddot{q} = \frac{1}{\Delta t}\left(\frac{q^{t+\Delta t} - q^t}{\Delta t} - \dot{q}^t\right)$$

From $q = K_{ar}(P_v - P_{ar}) + K_{iso}(P_{ar} - P_{at})$ we extract

$$P_{ar}^{t+\Delta t} = \frac{q^{t+\Delta t} - K_{ar} P_v^{t+\Delta t} + K_{iso} P_{at}^{t+\Delta t}}{K_{iso} - K_{ar}}$$

that we inject into equation (3.9). We thus obtain:

$$\begin{cases} d_0 = & \left(\frac{\tau}{\Delta t} + 1\right)\left(\frac{1}{K_{ar} - K_{iso}} + Z_c\right) + R_p + \frac{L}{\Delta t} + \frac{L\tau}{\Delta t^2} \\ d_1 = & \frac{K_{ar}}{K_{ar} - K_{iso}}\left(\frac{\tau}{\Delta t} + 1\right) \\ P = & \frac{\tau}{\Delta t} P_{ar}^t + P_{ve} + \frac{K_{iso}}{K_{ar} - K_{iso}}\left(\frac{\tau}{\Delta t} + 1\right) P_{at}^{t+\Delta t} \\ & - \left(\frac{\tau Z_c + L}{\Delta t} - \frac{L\tau}{\Delta t^2}\right) q^t - \frac{L\tau}{\Delta t} \dot{q}^t \\ D = & d_1 / d_0 \\ F_D = & P/d_0 - \mathbf{G}^T \mathbf{s}^t \end{cases}$$

The new constraint dynamical system to solve simultaneously for both ventricles, with the pressure vector $\mathbf{P_v} = [P_{vL}, P_{vR}]$ is therefore:

$$\begin{bmatrix} \mathbf{K} & \mathbf{G}^T \\ \mathbf{G} & \mathbf{D} \end{bmatrix} \begin{bmatrix} \Delta \mathbf{s} \\ \mathbf{P_v} \end{bmatrix} = \begin{bmatrix} \mathbf{F} \\ \mathbf{F}_D \end{bmatrix} \tag{3.10}$$

3.5.3 Resolution of the Constraint

To solve the dynamical system (3.10) and especially

$$\mathbf{K}\Delta\tilde{\mathbf{s}}^{t+\Delta t} = \mathbf{F} - \mathbf{G}^T {\mathbf{P}_\mathbf{v}}^{t+dt} \tag{3.11}$$

without adding state variables for $\mathbf{P_v}$, we design a prediction-correction algorithm (Algorithm. 1).

Algorithm 1 HeamodynamicModel() function

1: Apply the known pressure ${\mathbf{P}_\mathbf{v}}^t$ and find the velocities without constraint $\tilde{\mathbf{s}}^{t+\Delta t}$ solving $\mathbf{K}\Delta\tilde{\mathbf{s}}^{t+\Delta t} = \mathbf{F} - \mathbf{G}^T {\mathbf{P}_\mathbf{v}}^t$.

2: Use (3.11) which gives $\Delta\mathbf{s}^{t+\Delta t} = \Delta\tilde{\mathbf{s}}^{t+\Delta t} - \mathbf{K}^{-1}\mathbf{G}^T({\mathbf{P}_\mathbf{v}}^{t+\Delta t} - {\mathbf{P}_\mathbf{v}}^t)$ (adding and retrieving ${\mathbf{P}_\mathbf{v}}^t$). If ${\mathbf{P}_\mathbf{v}}^{t+\Delta t}$ meets the constraint (3.8), then

$$\mathbf{G}\Delta\tilde{\mathbf{s}}^{t+\Delta t} - \mathbf{G}\mathbf{K}^{-1}\mathbf{G}^T({\mathbf{P}_\mathbf{v}}^{t+\Delta t} - {\mathbf{P}_\mathbf{v}}^t) = \mathbf{F}_D - \mathbf{D}{\mathbf{P}_\mathbf{v}}^{t+\Delta t}.$$

3: Solve separately for each ventricle the equation $\mathbf{KA} = \mathbf{G}^T$ with $\mathbf{A} = [\mathbf{A}_L, \mathbf{A}_R]$ to get $\mathbf{B} = \mathbf{G}\mathbf{K}^{-1}\mathbf{G}^T = \mathbf{G}\mathbf{A}$ without inverting the stiffness $\mathbf{K}$.

4: Compute the unknown pressure

$${\mathbf{P}_\mathbf{v}}^{t+\Delta t} = (\mathbf{D} - \mathbf{B})^{-1}\left(\mathbf{F}_D - \mathbf{B}{\mathbf{P}_\mathbf{v}}^t - \mathbf{G}\Delta\tilde{\mathbf{s}}^{t+\Delta t}\right).$$

5: Correct the velocity such as

$$\Delta\mathbf{s}^{t+\Delta t} = \Delta\tilde{\mathbf{s}}^{t+\Delta t} - \mathbf{A}({\mathbf{P}_\mathbf{v}}^{t+\Delta t} - {\mathbf{P}_\mathbf{v}}^t).$$

3.6 Boundary Conditions

Two types of boundary conditions were defined to prevent rigid body motion. First, the heart mesh is attached at the level of the four valve annuli limiting the ventricles. To allow some valve motion, linear springs connect the valve vertices to their reference position. We defined a unique stiffness matrix $\mathbf{K} = k_b\mathbf{Id}$ where k_b is the isotropic stiffness. Therefore the force for each node is defined as $F_i = \mathbf{K}(Q_i - P_i)$ where P_i is the initial position and Q_i is the current position. A value of $50Pa$ was chosen for the stiffness k_b so as to allow a small movement of the valves. This constraint has a noticeable impact on the motion of the myocardium, but not as much on the global indices of the volume and pressure. The same constraint can be applied on the apex if necessary. Second, we defined a fixed pericardium surface surrounding the myocardium which limits the ventricle displacements: each time a epicardium vertex hits the pericardial surface, a force is applied preventing the penetration. The pericardial surface was defined as an offset surface of the epicardium situated at a fixed distance ($\sim 2mm$) from the epicardium at end-diastolic time point and efficient collision detection was implemented in SOFA. This collision constraint enables to limit the radial body motion but does not impact the global volume or pressure evolution.

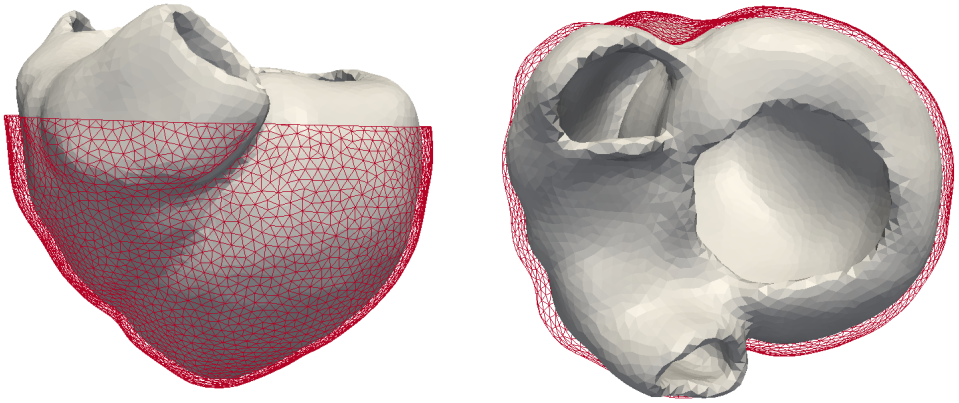

Figure 3.6: Representation of the myocardium mesh and its pericardium.

3.7 Simulations Results

The simulations were performed on a laptop PC with a Intel Core Duo processor at 2.80Hz and took around 10 minutes per cardiac cycle for meshes with approximately 80,000 tetrahedra. The time steps were set depending on the cardiac cycles and the number of images (for instance $dt = 7.75ms$ for 30 images and a heart period of 0.93s). A sensitivity study on the mesh quality and the time step showed that the chosen values lead to a good trade-off between computation time and accuracy. We also managed to recover the volume and pressure curves that clearly contain the four phases, as shown in Fig. 3.7.

With this example, the power developed by the heart can be computed as $P = \Delta V_L \, \Delta P_{vL} \approx 1.3W$ which is in the range of $[1W, 2W]$ usually referenced in the literature. Moreover, effects of preload (increase of the atrial pressure), afterload (increase of the aortic pressure) and inotropy (increase of the contraction rate) on Pressure-Volume loops were studied. Fig. 3.8 shows the results of these tests, which are in agreement with Klabunde (2011).

3.8 Discussion

The implementation of the BCS model in the SOFA platform differs from the one of (Chapelle et al., 2012b) in several ways. In our approach, the fiber stresses and stiffness at each node are not added as state variables but are solved separately from the position and velocity variables with a weaker coupling. This allows us to have a better conditioned system of equations that is solved efficiently with regular linear solver such as pre-conditioned conjugated gradient. Furthermore, we have linearized the strain relation $e_{1D} = e_s + e_c$ in the active components and solved the valve model with a prediction-correction approach which requires 2 additional solutions of the linear system of equations per time step. Also, fast assembly of the stiffness matrix associated with passive hyperelastic material was reached with the MJED method. Finally, we added a pericardial constraint to limit the displacement of epicardium vertices. Efficient and interactive simulations were made possible thanks to the adoption of the simulation platform SOFA. The simulation time is short enough so that

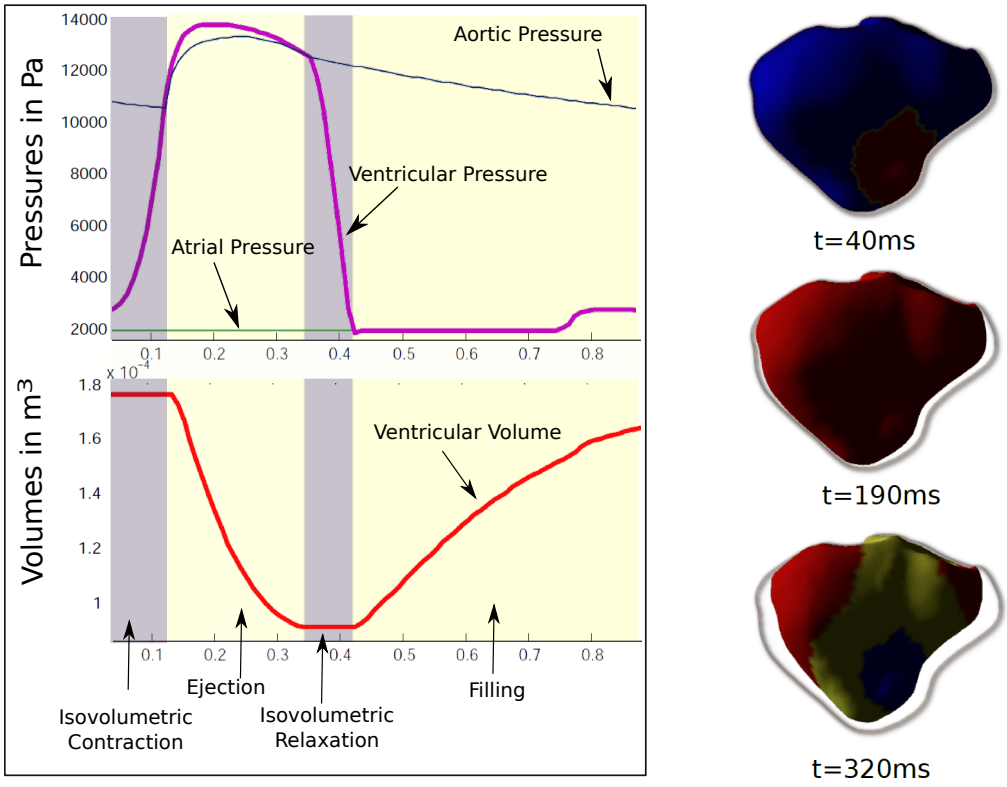

Figure 3.7: (Left) Resulting pressure and volume curves for the left ventricle, for one heart cycle. (Right) Resulting geometry at different times of the cycle overlaid with the initial mesh (in shadow). The color map indicates the potential wave, solutions of the electrophysiological node.

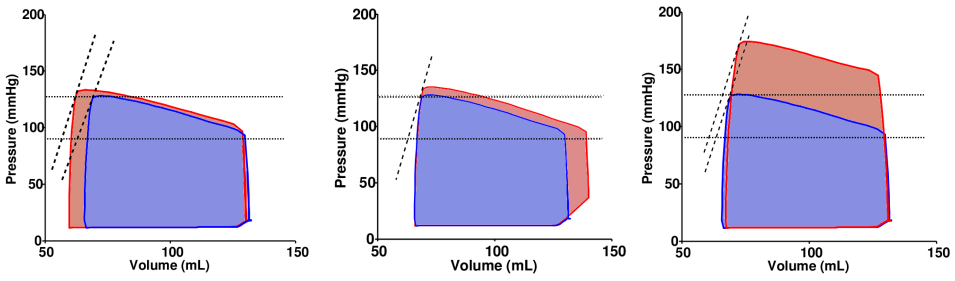

(a) Inotropy (b) Preload (c) Afterload

Figure 3.8: Independent increase of inotropy, preload and afterload (red loop), in comparison with the normal loop (blue). Horizontal dotted lines represent normal aortic systolic and diastolic pressures while dashed lines represent the slopes of the end-systolic pressure-volume relationship.

numerous parameter estimation techniques can be considered. However, a more precise convergence analysis on all the components of the model still needs to be done and would give precious information on the accuracy of the implementation. Finally, several cardiac therapy simulations are made possible with SOFA interactivity, such as Cardiac Resynchronization Therapy or cardiac Radio-Frequency Ablation (Mansi et al., 2009; Pernod et al., 2011).

Chapter 4

Automatic Global Calibration of the Model

Contents

Based on: an extended version of the published conference paper (Marchesseau et al., 2012c) split into two journal papers (Marchesseau et al., 2012a) that describes the calibration technique, its synthetic validation and its first application on volunteer data; and (Marchesseau et al., 2012d) which tests the calibration on pathological cases and compares the results with volunteer controls.

Patient-specific cardiac modelling can help in understanding pathophysiology and predict therapy effects. This requires the personalization of the geometry, kinematics, electrophysiology and mechanics. We use the Bestel-Clément-Sorine (BCS) electromechanical

model of the heart, which provides reasonable accuracy with a reduced parameter number compared to the available clinical data at the organ level. We propose a preliminary specificity study to determine the relevant global parameters able to differentiate the pathological cases from the healthy controls. To this end, a calibration algorithm on global measurements is developed. This calibration method was tested successfully on 6 volunteers and 2 heart failure cases and enabled to tune up to 7 out of the 14 necessary parameters of the BCS model, from the volume and pressure curves. This specificity study confirmed domain-knowledge that the relaxation rate is impaired in post-myocardial infarction heart failure and the myocardial stiffness is increased in dilated cardiomyopathy heart failures.

4.1 Introduction

The simulation becomes patient-specific after several levels of personalization: geometrical (a computational mesh is built from patient-specific anatomical images (see Fig. 1.1), kinematic (the motion of the cardiac structure is estimated from cine-MR images (McLeod et al., 2012; Sermesant et al., 2006)), electrophysiological (the depolarization and repolarization times are extracted from electrocardiograms (Relan et al., 2011a)) and mechanical. The focus of this chapter is on the latter personalization level, which consists in optimizing mechanical parameters of the model so that the simulation behaves in accordance to patient-specific datasets (images and other signals).

The latter inverse problem has been tackled by different authors. For instance, Xi et al. (2011) and Liu and Shi (2009) estimate the passive material stiffness with data assimilation methods while Wang et al. (2009) use Sequential Quadratic Programming. Moireau and Chapelle (2011a) as well as Chabiniok et al. (2011) estimate the contractility parameters using Reduced Unscented Kalman Filtering. Sundar et al. (2009) and Delingette et al. (2012) rather use adjoint data assimilation methods.

These methods are efficient to estimate some model parameters from the local motion and therefore open the possibility to help diagnosis and therapy planning. However, such algorithms are dependent on the initial range of parameter values since it is often necessary to be close to the solution for the algorithm to converge towards a meaningful local solution. The choice of the parameters to estimate and their initial calibration have therefore a great impact for the personalization. Moreover, these methods gives a distribution of the parameters along the myocardium which is almost impossible to analyze in order to classify or understand the pathologies. A global estimation of the parameters based on the global indices used in the clinical domain can therefore gives additional guidance to the cardiologists.

Our main contribution tackles this initialization issue: we propose a simple and efficient method to automatically calibrate the parameters from the ventricular volume evolution over the cardiac cycle. It has been applied successfully for the calibration of mechanical parameters from 7 healthy cases. Our proposed method is based on the Unscented Transform algorithm and requires only one iteration with multiple simulations performed in parallel for calibrating typically 4 or 5 parameters selected from a sensitivity analysis.

Then, the developed calibration algorithm, tested on 7 volunteers cases and 2 heart failure cases managed to tune 7 out of the 14 BCS model parameters with 12% relative errors. These results lead to a preliminary specificity study to determine which of the 7 parameters are specific for the classification of the two heart failure cases.

In this chapter, we first give the results of the sensitivity analysis that we performed

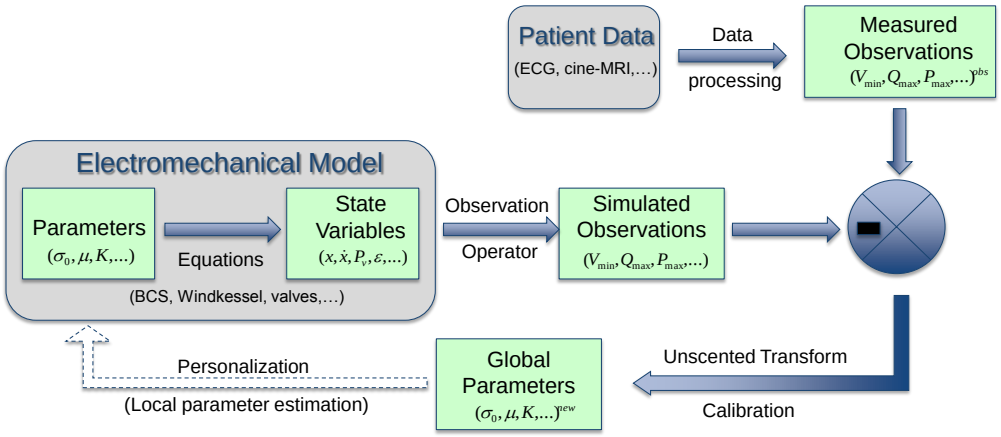

Figure 4.1: Complete electromechanical personalization pipeline. Our contribution does not deal with the local personalization step.

in order to select the most relevant parameters and observations that characterize a cardiac cycle. Then, the calibration algorithm is described and validated on synthetic data before being tested on real cases. A first analysis gives the results of the calibration on healthy cases where volume curves only are taken into account while a second study intends to calibrate more parameters from volume and pressure curves on healthy and pathological cases. We finally compare the resulting parameters in a specificity study.

4.2 Sensitivity Analysis

We propose in this chapter a calibration method of the model parameters. A first step is to select the main parameters that can be estimated given the available data. To this end, we study the influence of each active, passive and heamodynamic model parameter on the volume, the outward flow ($q = -dV/dt$) and the pressure in the ventricle. This required about 160 simulations. The results are given here only for the left ventricle since the right ventricle has a similar behaviour. Only the first cycle is presented in order to have a coherent comparison between parameters. The sensitivity analysis is performed with null initial velocities for two reasons: first, the cycle starts with the isovolumetric contraction phase so the initial velocity is small and second, the temporal samplings of the MRI datasets are too sparse (only 30 images for 0.93s) to precisely estimate the initial velocity. The results are shown for one volunteer geometry, similar results were found on different geometries. The variation of the parameters was chosen after a trial and error approach in order to obtain a physiologically realistic behaviour. The used minimum and maximum values are presented in Table 4.1. Results of the sensitivity analysis on the volume, pressure and flow curves are presented below.

4.2.1 Active parameters

The active parameters mainly influence the volume curves in terms of amplitude, slopes or duration of the phases. Some of them also influence the pressure curves. Relevant curves are presented in Fig. 4.2 for the volume and Fig. 4.3 for the pressure.

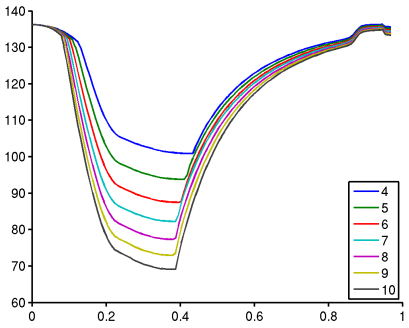

(a) Volume: σ_0

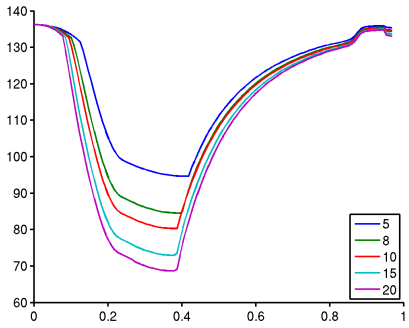

(b) Volume: k_{ATP}

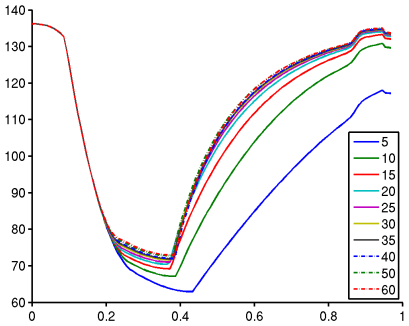

(c) Volume: k_{RS}

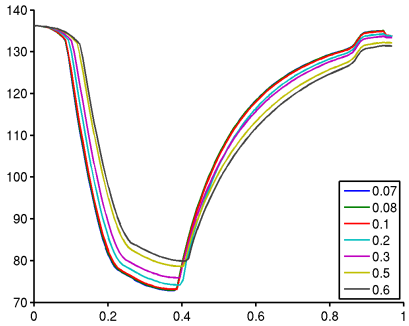

(d) Volume: μ

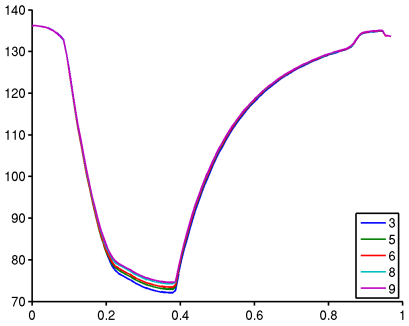

(e) Volume: k_0

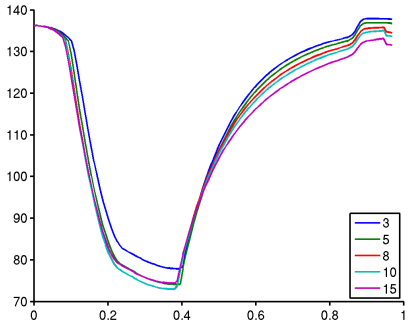

(f) Volume: E_s

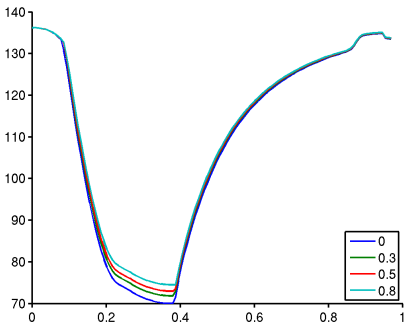

(g) Volume: α

Figure 4.2: Volume evolution (in mL) over time (in s) for the left ventricle, with varying active parameters.

Table 4.1: Ranges of parameter values explored in the sensitivity analysis.

Notation	Parameter Name	Min - Max
σ_0 (MPa)	Max Contraction	$4-10$
k_0 (MPa)	Max Stiffness	$3-9$
k_{ATP} (s^{-1})	Contraction Rate	$5-20$
k_{RS} (s^{-1})	Relaxation Rate	$5-60$
E_s (MPa)	Linear Modulus	$3-15$
α	Cross-bridges Unfasten Rate	$0-0.8$
μ (MPa.s)	Viscosity	$0.07-0.6$
c_1 (kPa)	Mooney Rivlin Modulus	$7-20$
c_2 (kPa)	Mooney Rivlin Modulus	$7-20$
K (MPa)	Bulk Modulus	$6-25$
τ (s)	Wind. Charact. Time	$0.4-2$
R_p ($MPa.m^{-3}.s$)	Wind. Periph. Resistance	$30-300$
Z_c ($MPa.m^{-3}.s$)	Wind. Charact. Resistance	$1-10$
L ($kPa.s^2.m^{-3}$)	Wind. Total Art. Inertance	$1-100$

From these curves, we can conclude that the maximum contraction σ_0 and the contraction rate k_{atp} act together to increase the ejection fraction and change both the relaxation and the contraction slopes while the relaxation rate k_{rs} only influences the relaxation phase. The linear modulus E_s and the viscosity parameter μ modify the slopes and enable a complete cycle. Finally both the maximum stiffness k_0 and the cross-bridges unfasten rate α have a small influence on the ejection fraction. Similar conclusions can be drawn for the pressure curves: when a parameter acts on the ejection fraction it also acts on the maximum pressure, the pressure slopes are dependent on the same parameters as the volume slopes.

4.2.2 Passive Parameters

No significant differences in terms of pressure or volumes curves can be noticed between the two Mooney-Rivlin parameters c_1 and c_2, therefore the influence of only one of them is given in Fig. 4.4. Mooney Rivlin first modulus c_1 influences the ejection fraction and the maximum of pressure. The bulk modulus K greatly acts on the relaxation phase. Moreover, when those parameters are too large, the end-diastolic volume decreases. K controls the quasi-incompressibility of the myocardial motion, the higher K the closer to incompressibility the motion. We noticed that incompressibility is an important factor to recover some torsion during the isovolumetric phases.

4.2.3 Heamodynamic Model Parameters

Since the list of parameters that influence the heamodynamic constraint is important, we consider here only the Windkessel parameters, that mainly act on the aortic pressure. The atrial pressure is supposed to be known, this pressure only impacts the fast filling period. We can also vary the initial and the asymptotic aortic pressures, but they only translate the resulting pressure curves. Therefore we use default values from the literature (Schäffler and Schmidt, 1999).

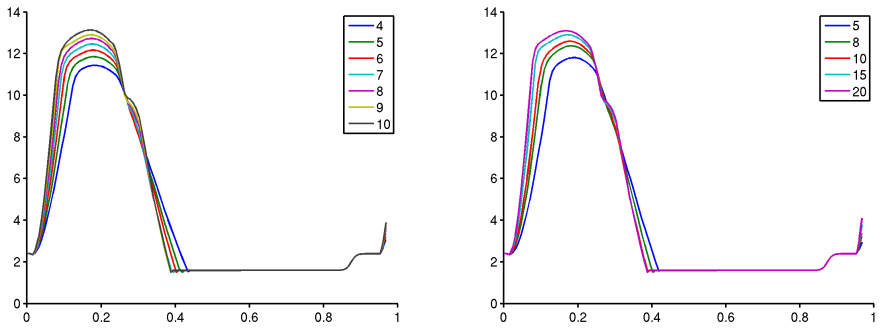

(a) Pressure: σ_0 (b) Pressure: k_{ATP}

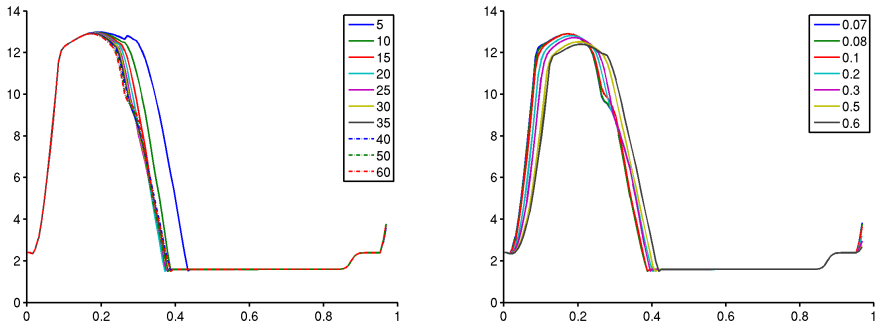

(c) Pressure: k_{RS} (d) Pressure: μ

Figure 4.3: Pressure evolution (in *kPa*) over time (in *s*) for the left ventricle, with varying active parameters.

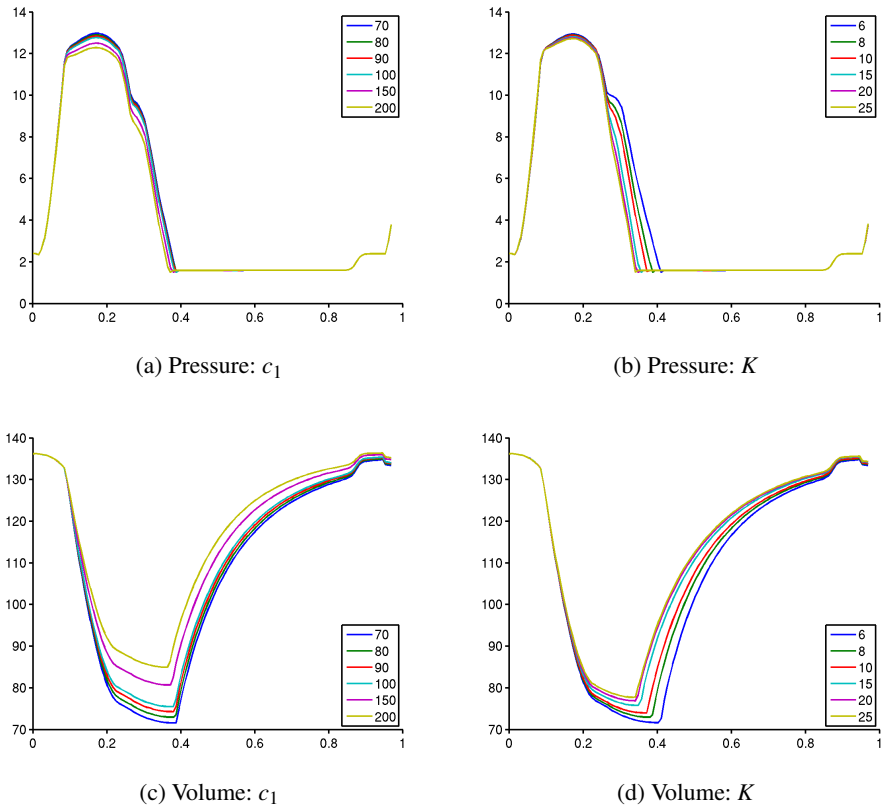

(a) Pressure: c_1

(b) Pressure: K

(c) Volume: c_1

(d) Volume: K

Figure 4.4: Pressure (in *kPa*) and volume (in *mL*) evolution over time (in *s*) for the left ventricle, with varying passive parameters.

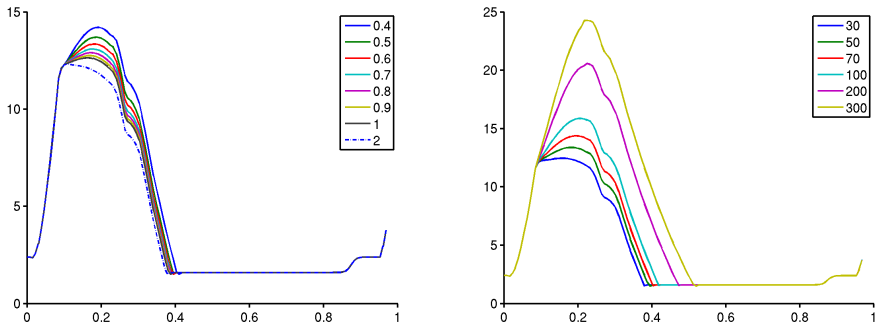

(a) Pressure: τ

(b) Pressure: R_p

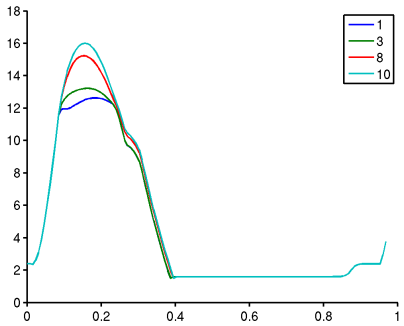

(c) Pressure: Z_c

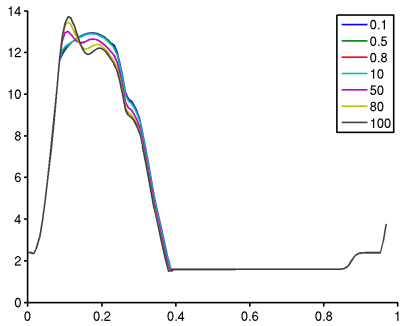

(d) Pressure: L

Figure 4.5: Pressure evolution (in *kPa*) over time (in *s*) for the left ventricle, with varying Windkessel parameters.

Results are presented in Fig. 4.5 on the pressure curves only. The peripheral resistance R_p strongly acts on the maximum pressure but also on the length of the isovolumetric relaxation. The characteristic time τ influences the maximum of pressure whereas the characteristic resistance Z_c and the total arteria inertance L change the shape of the pressure during the ejection. The isovolumetric factors K_{isoC} and K_{isoR} tend to flatten the volume during the contraction and the relaxation respectively, and decrease the flow toward zero (as shown in Fig. 4.6).

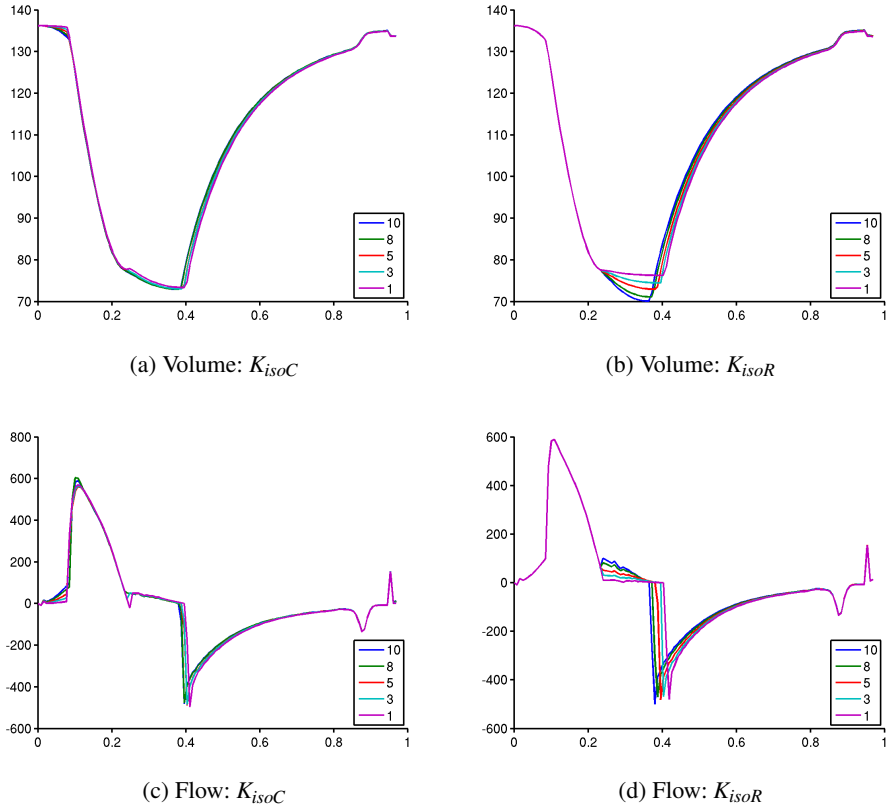

(a) Volume: K_{isoC}

(b) Volume: K_{isoR}

(c) Flow: K_{isoC}

(d) Flow: K_{isoR}

Figure 4.6: Volume (in mL) and outward flow (in $mL.s^{-1}$) evolution over time (in s) for the left ventricle, with varying isovolumetric factors. The local minimum of the flow at the end of the cycle represents the beginning of the fast filling.

The effects of parameter interactions on the minimum volume V_{min} was also studied. Fig. 4.7 shows that the proposed sensitivity analysis holds at various operating points. Therefore the performed sensitivity analysis enables to draw conclusions on the selection of the most influential parameters.

4.3 Unscented Transform Algorithm

From this qualitative study of the main model parameters, we determine a strategy to automatically assess the model parameters from the volume and flow curves. Since our goal is to calibrate and not to personalize the model, the method has to be fast and require minimal implementation. We chose the ventricular volume curves as main observation to perform

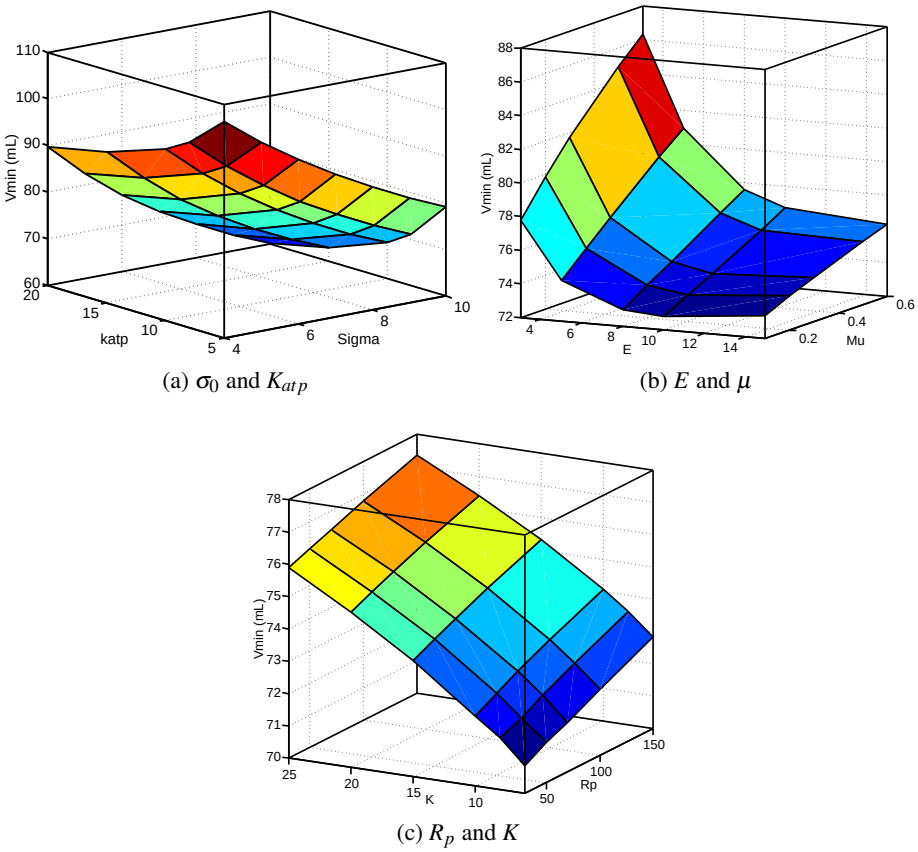

(a) σ_0 and K_{atp}

(b) E and μ

(c) R_p and K

Figure 4.7: Effects of parameter interactions on V_{min}. Varying two parameters in a grid leads to a similar global trend.

the calibration as they are important physiological indices and can be captured by few quantities: the minimum volume V_{min} (which could also be the ejection fraction since the maximum volume is constant over all cases), the maximum and minimum of the flow (q_{max} and q_{min} respectively). Moreover, if the pressure curves are available, indices on the pressure are also considered.

4.3.1 Unscented Transform Algorithm

To calibrate the model, we use the algorithm derived from the Unscented Transform (Julier and Uhlmann, 1997). The proposed algorithm finds a set of parameters that minimizes the difference between the measured observation $\mathbf{Z}^{obs}$ and the predicted observation $\bar{\mathbf{Z}}$. It is explained as follows: Let $\mathbf{Z}$ be the vector of observations and $\mathbf{X}$ the parameter vector which has mean $\mathbf{X}^0$, covariance $\mathbf{C}_X$ and dimension n. We set the covariance as $\mathbf{C}_X = \mathbf{Cov}(\mathbf{X},\mathbf{X})$ by estimating the minimal and the maximal value of each parameter with a trial and error approach. We compute observations $\mathbf{Z}_{i\varepsilon}$ from the $2n+1$ sets of parameters $\mathbf{X}_{i\varepsilon} = [x_1, x_2, ..., x_i + \varepsilon s_i, ...]$ around the mean value $\mathbf{X}^0$ where $\varepsilon \in \{-1, 0, 1\}$ and s_i is an uncertainty function of the covariance $s_i = \gamma\sqrt{\mathbf{C}_{Xi}}$, with γ the scaling parameters. The mean observation is set as $\bar{\mathbf{Z}} = \sum_{i,\varepsilon} \omega_{i\varepsilon}\mathbf{Z}_{i\varepsilon}$ with some weights $\omega_{i\varepsilon}$ described by Wan and Van Der Merwe (2000). Finally we derive the covariance matrix as:

$$\mathbf{Cov}(\mathbf{X},\mathbf{Z}) = \sum_{i\varepsilon} \omega_{i\varepsilon}(\mathbf{X}_{i\varepsilon} - \mathbf{X}^0)\,(\mathbf{Z}_{i\varepsilon} - \bar{\mathbf{Z}})^T \tag{4.1}$$

The new set of parameters $\mathbf{X}^{new}$ found to match the observations $\mathbf{Z}^{obs}$ is

$$(\mathbf{X}^{new} - \mathbf{X}^0) = \mathbf{Cov}(\mathbf{X},\mathbf{Z})\,\mathbf{Cov}(\mathbf{Z},\mathbf{Z})^{-1}\,(\mathbf{Z}^{obs} - \bar{\mathbf{Z}}) \tag{4.2}$$

where

$$\mathbf{Cov}(\mathbf{Z},\mathbf{Z}) = \sum_{i\varepsilon} \omega_{i\varepsilon}(\mathbf{Z}_{i\varepsilon} - \bar{\mathbf{Z}})\,(\mathbf{Z}_{i\varepsilon} - \bar{\mathbf{Z}})^T. \tag{4.3}$$

This algorithm is very simple to implement and runs in one iteration to give $\mathbf{X}^{new}$. Another simulation is necessary to obtain the resulting observation $\mathbf{Z}^{new}$. The algorithm is illustrated in Fig. 4.8.

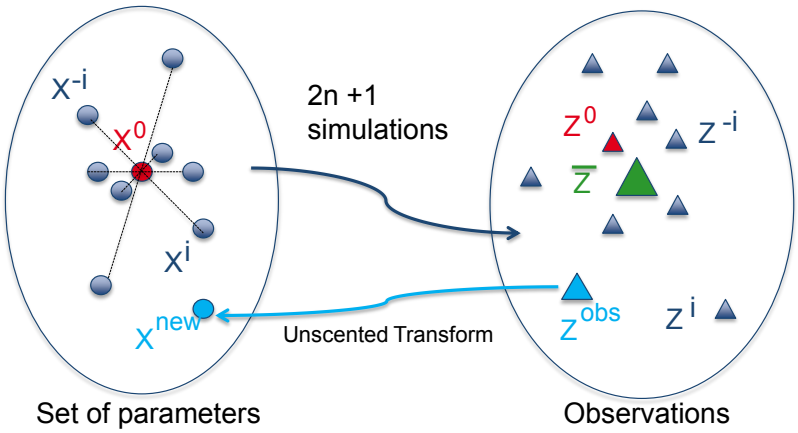

Figure 4.8: Schematic representation of the Unscented Transform algorithm

4.3.2 Qualitative and Quantitative Parameter Selection: Volume Curves Only

Sixteen parameters in total may be estimated: $(\sigma_0, k_{rs}, k_{atp}, k_0, \alpha, \mu, E_s)$ active parameters, (K, c_1, c_2) passive parameters and $(R_p, \tau, Z_c, L, K_{isoC}, K_{isoR})$ for the valve model. Since it is not reasonable to try to estimate all of them at once, we decide to set some of them to a standard value and estimate the remaining ones. The selection was made from the sensitivity analysis results and confirmed by a Singular Value Decomposition (SVD) of the covariance matrix $\mathbf{Cov}(\mathbf{X},\mathbf{Z})$ between all 16 parameters and the three observations $[V_{min}, q_{max}, q_{min}]$. Then, for each vector $\mathbf{X}_{i\varepsilon}$, the observations $\mathbf{Z}_{i\varepsilon}$ are computed (which corresponds to 33 simulations). The Singular Value Decomposition leads to $\mathbf{Cov}(\mathbf{X},\mathbf{Z}) = \mathbf{USV}^T$ where $\mathbf{U}$ is a 16×16 unitary matrix whose columns are called the left singular vectors and represent the eigenvectors of $\mathbf{Cov}(\mathbf{X},\mathbf{Z})\mathbf{Cov}(\mathbf{X},\mathbf{Z})^T$. Four parameters were therefore selected.

Selection from the Sensitivity Analysis

From the curves presented earlier, we fixed k_{atp} because its impact on the observations is coupled with the impact of the maximum contraction σ_0. The same conclusions follow for the passive parameters which all act in the same direction, therefore we only estimated the bulk modulus K. We noticed that the linear modulus E_s and the viscosity parameter μ have similar behaviour, we therefore estimated only μ. We fixed the cross-bridges unfasten rate α and the maximum stiffness k_0 which do not have an impact as strong as the other parameters. Finally the peripheral resistance R_p was also estimated since it acts significantly on the slopes and ejection fraction. Not considering the other valve model parameters since no data is usually available on the pressure, we were left with the following five parameters $(\sigma_0, k_{rs}, \mu, K, R_p)$ to estimate.

Selection from the Singular-Value Decomposition

The Singular-Value Decomposition (SVD) led to left singular vectors representing the eigenvectors of $\mathbf{Cov}(\mathbf{X},\mathbf{Z})\mathbf{Cov}(\mathbf{X},\mathbf{Z})^T$. The first three singular vectors only were considered (since there were only three observations). They depended mainly on the four parameters (σ_0, K, R_p, μ) and slightly on k_{rs}. This analysis led us to try both $\mathbf{X} = \mathbf{X4} = [\sigma_0, \mu, K, R_p]$ and $\mathbf{X} = \mathbf{X5} = [\sigma_0, K, R_p, \mu, k_{rs}]$ for the automatic calibration which is coherent with the previous selection of parameters provided by the sensitivity analysis.

4.3.3 Parameter Selection: Volume and Pressure Curves

The calibration algorithm was then used to compare the estimated parameters between volunteer and heart failure cases. Both volunteer and pathological data include the MRI sequences. Moreover, the heart failure cases data includes the pressure curves, therefore all 6 observations were available: the minimum volume V_{min}, the extrema of the outward flow q_{min} and q_{max}, the maximum pressure P_{max} and the extrema of its derivative dP/dt_{min} and dP/dt_{max}. Volunteer data included only MR images, so only the volume evolution is available. Therefore standard pressure indices were imposed on the volunteers so that the same calibration technique could be performed on control and pathological cases. From this comparison, conclusions can be extracted on which parameter is specific to the type of disease. Results of this study are presented in Sec. 4.5. The calibration of the *APD* enabled a better

fit of the cardiac phases but is not considered here for the specificity analysis. When pressure curves are available, more parameters can be estimated. k_{rs}, k_{atp} as well as the stiffness parameter c_1 were chosen since they greatly influence the pressure slopes.

4.3.4 Computational Considerations

Before running the proposed algorithm, a few manual steps were performed on one volunteer case. First, γ and the weights $\omega_{i\varepsilon}$ have to be adjusted. They both depend on the dimension n and on a parameter α which represents the spread of the sigma points around $\mathbf{X}^0$ and is set to 10^{-1} (Wan and Van Der Merwe, 2000). Then, the covariance matrix $\mathbf{C}_X$ and the initial value $\mathbf{X}^0$ had to be defined. They were computed from a trial and error approach using a uniform distribution with minimum and maximum values given in Table 4.1. These values correspond to the limits of the parameters that led to physiologically correct curves (e.g including the four cardiac phases). Once calibrated on one volunteer, the same values were used on all the cases. To obtain the n parameters from this algorithm, $2n+1$ independent simulations are required. To check the results, another simulation is performed and the resulting observations are compared to the data. When dealing with real data, a time shift is estimated *a posteriori* since the simulation does not start exactly at the same time and phase of the cycle as the time series of images. This time shift is computed in order to minimize the mean square difference between the volumes over time in the data (V^{obs}) and the ones after estimation of the parameters (V^{new}). We record this time shift since it is required for the personalization technique based on images as well. Finally, in order to fit the end-diastolic volume or pressure, the atrial pressure is manually adjusted.

4.4 Results

For this work, our database was first made of 7 healthy cases acquired at King's College London and made available to the community for the STACOM challenge 2011. Later, we also used 2 pathological cases also acquired at King's College London, having LBBB heart failure. In addition, one has a severe dilated cardiomyopathy and the other is a post-myocardial infarction heart failure.

For all cases, the kinematic motion was estimated using the iLogDemons algorithm which allowed to compute the real volume curves. Furthermore, Ensite data was acquired on the pathological cases allowing to have a personalized electrophysiology and real pressure curves.

4.4.1 Synthetic Validation

First, tests on synthetic data were performed to verify the effectiveness of the method when using the volume curves only. We simulated a cardiac cycle with known parameters and extracted the resulting ventricular volume curve as detailed in Appendix C. The application of the calibration method on this synthetic volume curve led to 4 or 5 parameters supposed to produce the same volume curve. Indeed, a good match was found with the volume curve and its derivative as shown in Fig. 4.9. The mean relative error between the data Z^{obs} and the observations obtained after parameter calibration Z^{new} was less than 1%. No differences were noticeable between the estimation of 4 parameters or 5 parameters.

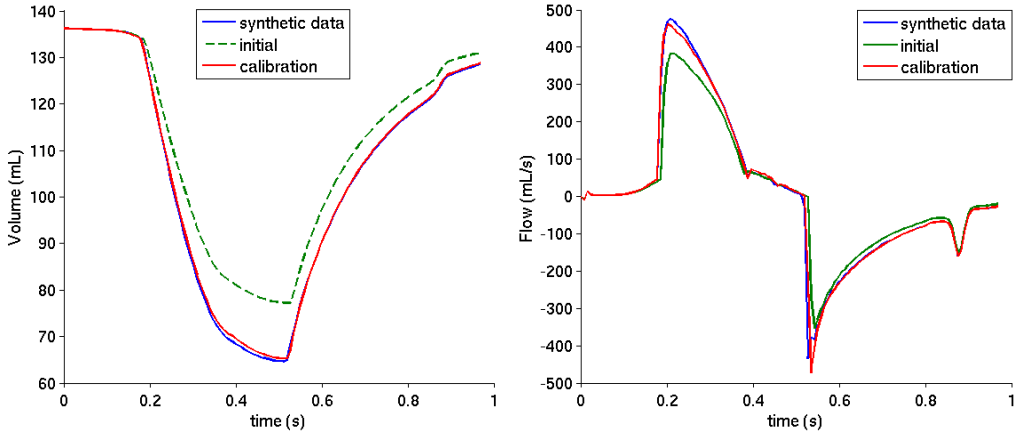

Figure 4.9: Results of the calibration technique on synthetic data on the volume evolution in mL(top) and the outward flow function in $mL.s^{-1}$ (bottom).

Therefore, this calibration technique from the volume curve allows to estimate 4 (or 5) influential parameters after performing 9 (or 11) independent simulations (that can be launched in parallel). Hence, this technique is fast and is suitable to be applied on a large database of patients. Table 4.2 compares the parameters used to simulate the data and the estimated ones. It shows that the solution is not unique due to parameter observability issues and possible correlation between the parameters that lead to the non-uniqueness of the solution for these observations. More observation would be required to constrain the uniqueness of the parameters.

Table 4.2: Parameters values found by the calibration algorithm on synthetic data for 4 parameters.

	σ (MPa)	K (MPa)	R_p (MPa)	μ (MPa.s)
Data	10	10	80	0.2
X4	9.5	12.9	83	0.3

4.4.2 Results on Healthy Volunteers: Volume Curves Only

A first real cases study was performed on the 7 healthy hearts provided by the STACOM challenge. The electrophysiological model was simulated with standard values of the conductivity and the anisotropic ratio. From the kinematic personalization, we registered all images on the end diastolic image. Then, image transformations were applied to the end-diastolic tetrahedral mesh to estimate the volume of the ventricles over time and then the observation vector $\mathbf{Z}^{obs}$. The calibration required launching 9 (or 11) simulations around the mean parameter vector $\mathbf{X}^0 = [7, 13, 100, 0.28]$ and 4 (or 5) parameters were then estimated based on the Unscented Transform algorithm. Fig. 4.10 shows the measured, reference and estimated volume curves on case 3. More results can be found on Fig. 4.11 and Fig. 4.12. Fig. 4.13 shows two views of the estimated cardiac motion overlapped with the MRI sequence at different times of the cycle. The meshes seem to follow reasonably well the

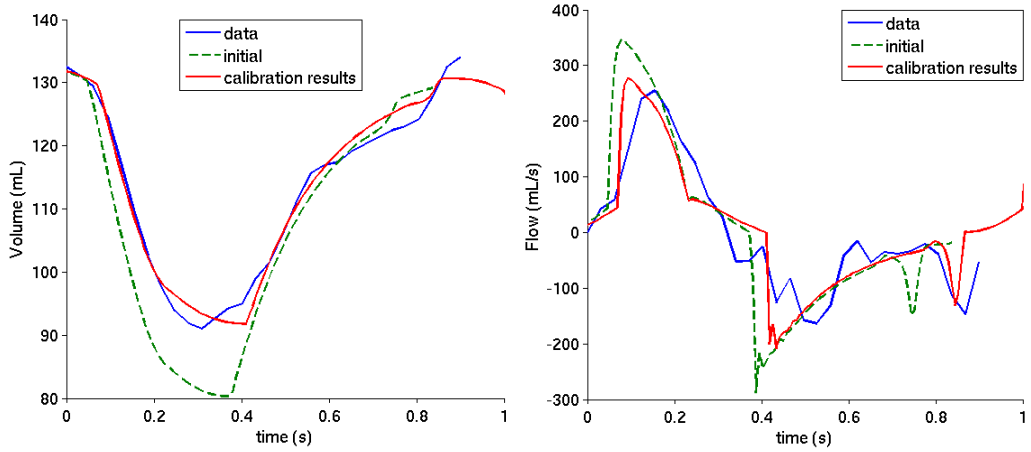

Figure 4.10: Results of the calibration technique on real data for one healthy volunteer #3. (Left) Volume evolution in mL. (Right) Flow evolution in $mL.s^{-1}$.

images at each phase of the cardiac cycle. Differences may be explained by segmentation errors on the first image, by registration errors or model errors.

Trying to estimate 4 or 5 parameters in all of the cases showed that the results are either similar, or better with 4 parameters than with 5. Therefore only the variation of 4 parameters was studied. Errors between the real observations $\mathbf{Z}^{obs}$ and the simulated observations $\mathbf{Z}^{new}$ are given in Table 4.3.

Table 4.3: Relative errors (in %) between simulated results $\mathbf{Z}^{new}$ and real data $\mathbf{Z}^{obs}$ on the 7 healthy cases

Volunteers	1	2	3	4	5	6	7	Mean	Min	Max
V_{min}	0.35	3.51	0.83	0.79	1.09	1.38	1.31	1.26	0.35	3.51
q_{max}	3.06	20.99	8.57	21.37	11.5	12.1	5.36	14.29	3.06	21.37
q_{min}	0.31	4.12	27.41	6.48	27.58	16.92	5.81	15.18	0.31	27.58

For all cases, the match is excellent for the minimum volume and hence the ejection fraction, but less good ($\simeq 15\%$) for the slopes. A second iteration of the algorithm did not lead to any improvement therefore the given match is the best possible with this method. Errors can be explained in several ways. First, the real volume curve extracted from the images contains registration errors; then, errors on the geometry, the fibers and electrophysiology add to these results. Finally, the choice of the calibrated parameters is not unique and influences the results.

4.4.3 Results on Pathological Cases: Volume and Pressure Curves

The proposed calibration algorithm was then applied on six of the seven volunteers (one volunteer case was taken out of the study due to an unrealistic kinematic personalization that created issues when calibrating both the volume and the pressure curves) and the two Left Bundle Branch Block (LBBB) cases. A synthetic pressure was given for the healthy cases in order to estimate as many parameters as for the pathological cases from which the real pressure curves are known. We therefore performed the calibration

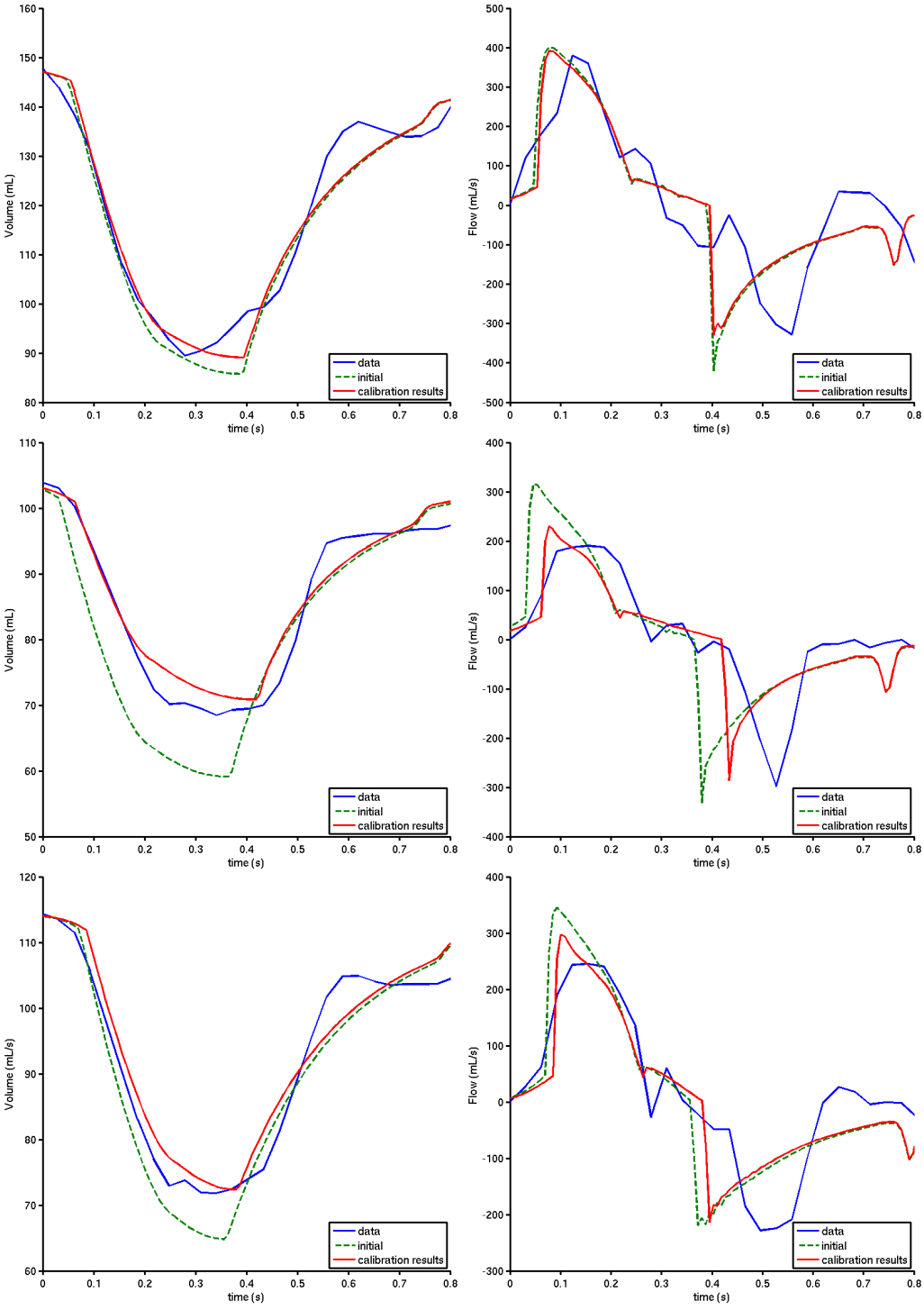

Figure 4.11: Results of the calibration technique on real data for volunteers #1, #2, #4 from top to bottom.

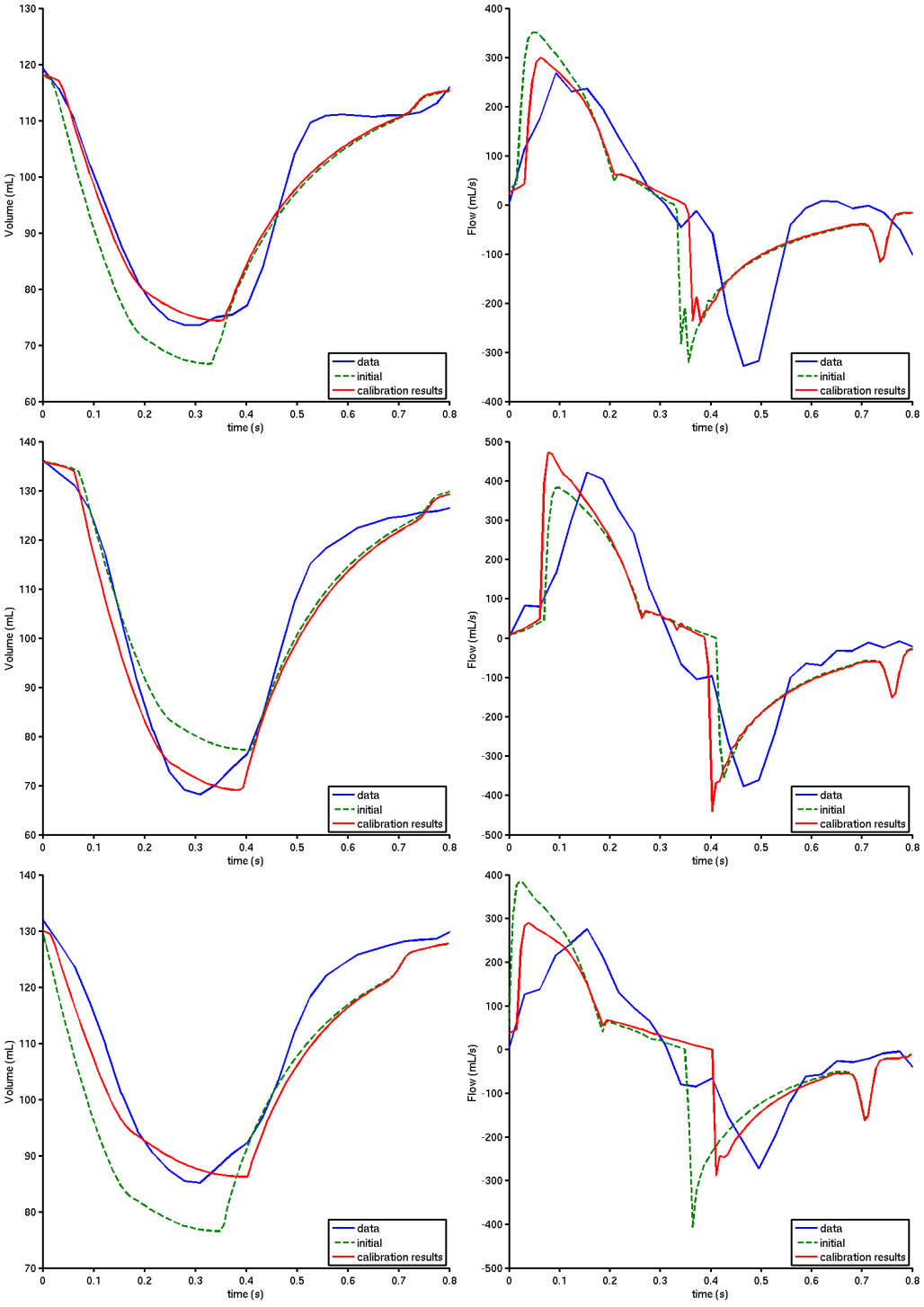

Figure 4.12: Results of the calibration technique on real data for volunteers #5, #6, #7 from top to bottom.

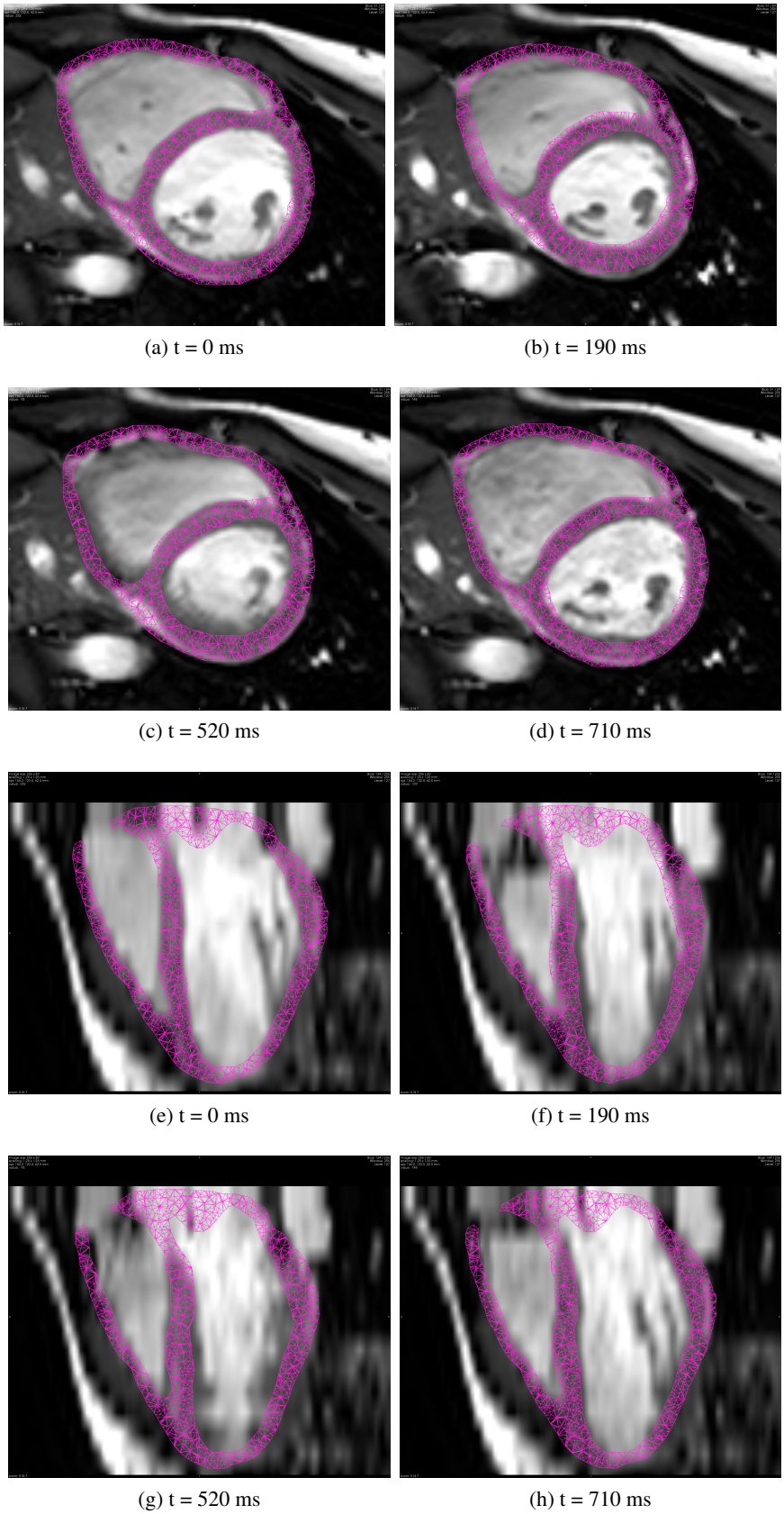

(a) t = 0 ms (b) t = 190 ms

(c) t = 520 ms (d) t = 710 ms

(e) t = 0 ms (f) t = 190 ms

(g) t = 520 ms (h) t = 710 ms

Figure 4.13: Short axis and long axis views of the simulated mesh on top of the MR images at different moments of the cardiac cycle (heart period = 930 ms) for case 3.

for the parameter vector $\mathbf{X} = [\sigma_0, k_{atp}, k_{rs}, \mu, c_1, K, R_p]$ with initial value of the parameters $\mathbf{X}^0 = [7, 15, 35, 0.28, 80, 13, 100]$. A calibration on the left ventricle only was performed due to the difficulty to segment and register the right ventricle which leads to noisy volume curves. The relative errors between the real observations $\mathbf{Z}^{obs}$ and the simulated observations $\mathbf{Z}^{new}$ are shown on Fig. 4.14, before and after calibration. Fig. 4.15 shows the measured, reference and estimated volume and pressure curves of the LBBB post-MI HF case while Fig. 4.17 shows the results for the LBBB DCM case. A comparison of the simulated mesh and the MRI sequence for the LBBB post-MI HF case is presented Fig. 4.16. It shows that the calibration gives satisfactory results and can therefore be used for the preliminary specificity study.

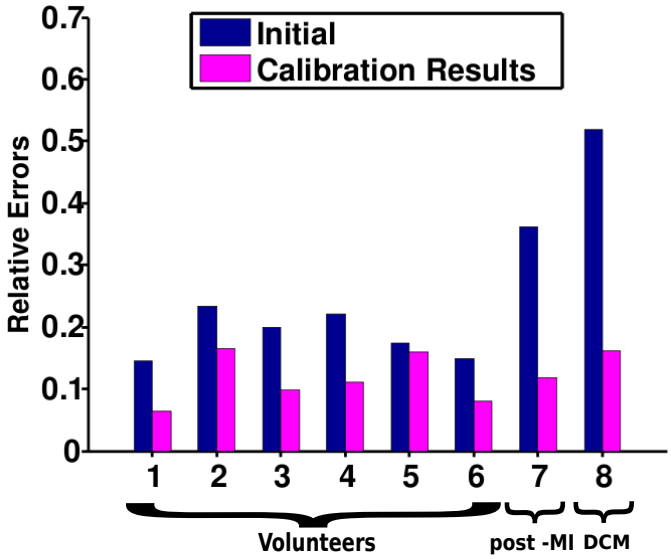

Figure 4.14: Relative errors on the observations of the 6 volunteers and the two LBBB cases.

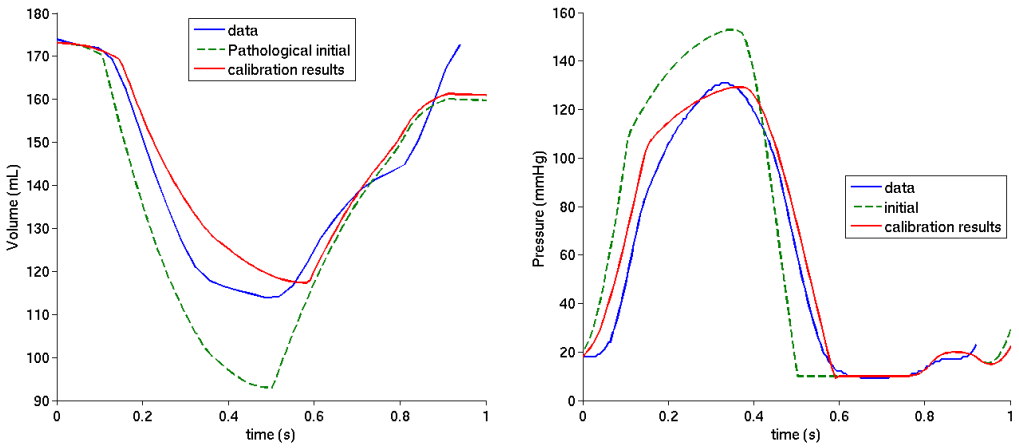

Figure 4.15: Results of the calibration technique on real data for post-MI HF case. (Left) Volume evolution in *mL*. (Right) Pressure evolution in $mmHg$.

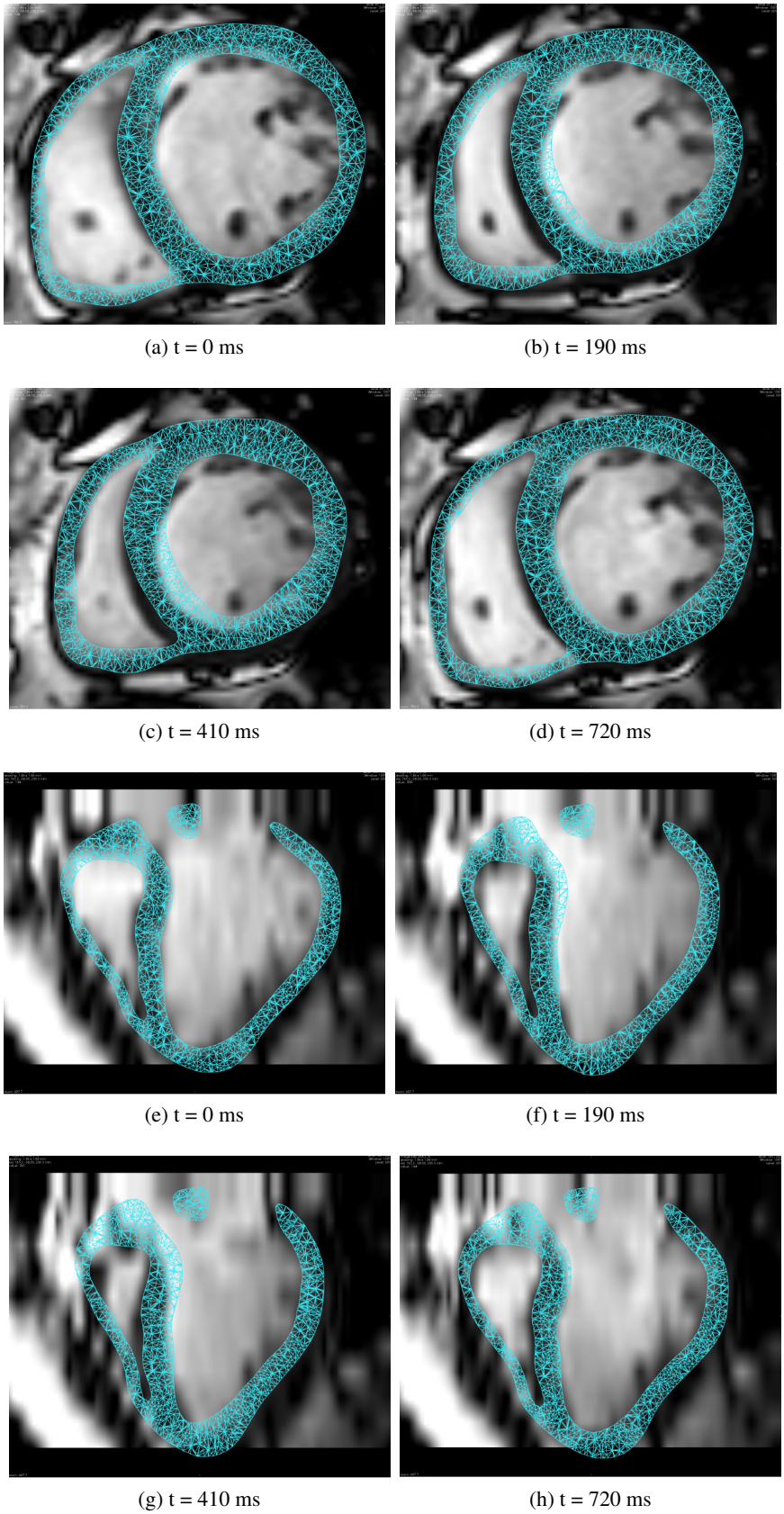

(a) t = 0 ms (b) t = 190 ms

(c) t = 410 ms (d) t = 720 ms

(e) t = 0 ms (f) t = 190 ms

(g) t = 410 ms (h) t = 720 ms

Figure 4.16: Short axis and long axis views of the simulated mesh on top of the MR images at different moments of the cardiac cycle (heart period = 930 ms) for LBBB post-MI HF case.

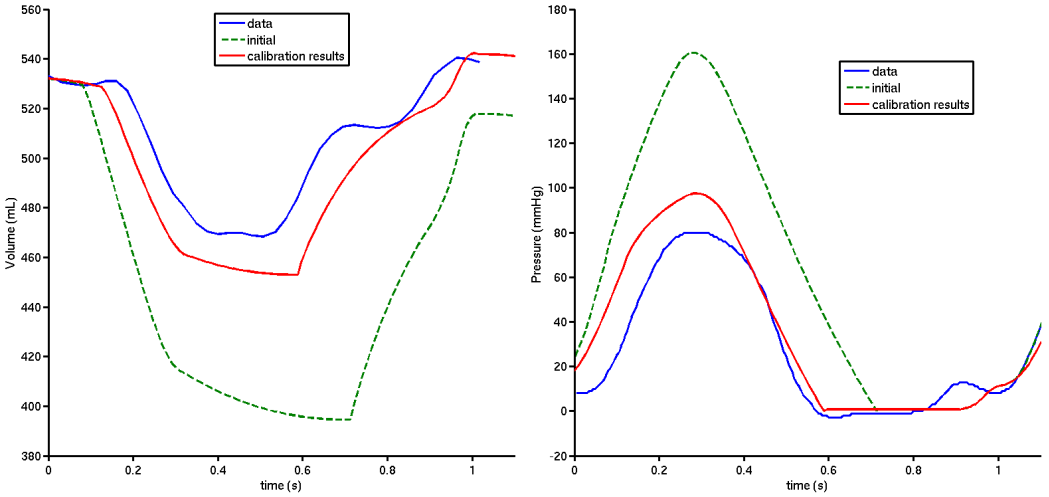

Figure 4.17: Results of the calibration technique on real data for DCM HF case. (Left) Volume evolution in *mL*. (Right) Pressure evolution in *mmHg*.

4.4.4 Evaluation of Registration Error Influence

We tried to evaluate the error in the registration technique to understand whether the model could actually match the data better than shown on Figures 4.10, 4.11 or 4.12. For this purpose, we created synthetic images (as done by (Prakosa et al., 2011)) from a real sequence, using the deformed meshes resulting from a simulation (see Fig.4.18). This tech-

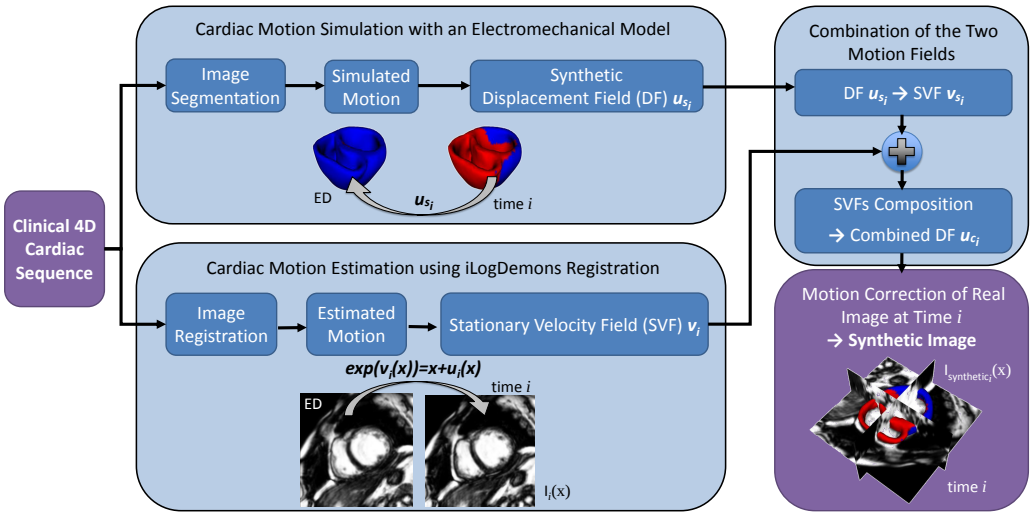

Figure 4.18: Synthetic 4D Cardiac Sequence Generation Pipeline. A clinical 4D sequence is used as an input to create a synthetic 4D sequence in which the myocardium motion follows a prescribed simulated displacement field. A cardiac E/M model simulates the cardiac contraction using a cardiac mesh created from the myocardium segmentation at ED. iLogDemons registration method is applied to all images in the real clinical sequence to register them to the End diastolic reference image. The combined simulated and registration motion are used to deform the real clinical images in order to create the synthetic cardiac sequence.

nique creates new cardiac cine-MRI sequences combining the deformation field computed

by the simulation and the deformation field computed by the image registration of the real sequence. We then registered this new sequence with the iLogDemons algorithm, and extracted the volume curves from the resulting registered meshes. We expect to have similar curves since images are created from the same electromechanical model of the heart. The comparison between the initial simulated volume curve and the one computed after registration is given in Fig. 4.19. The relative error is about 25% for both slopes and 3% for V_{min}. These errors indicate that the model may not be able to better match these registered volume curves. This can be due to registration errors as well as modelling errors.

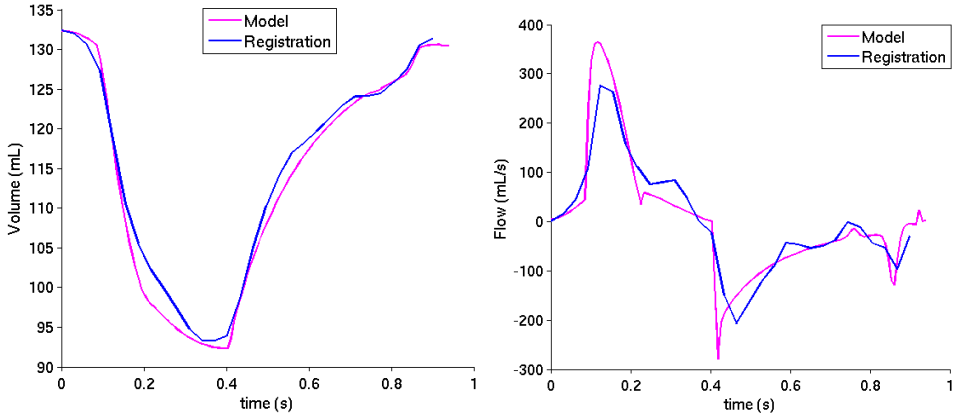

Figure 4.19: Comparison between the volume variation computed from the simulation and the one estimated from registered images (in mL).

4.5 Preliminary Specificity Analysis

A box plot in Fig. 4.20 presents the results of all volunteer cases on parameter values normalized by $\mathbf{X}^0$ through their five-number summaries: the smallest value, lower quartile, median (red), upper quartile, and largest value. We can easily see that for some model parameters, the values obtained for the pathological cases are outliers compared to the values of the volunteers. In more details, it shows that the post-MI HF case has a reduced peak contractility and an impaired relaxation (reduced relaxation rate). It is in agreement with medical knowledge about myocardial infarction impact on diastole, for instance such decrease of the relaxation rate was evaluated in ischemic dog hearts (Williams et al., 1980) and confirmed on human hearts in (Otto, 2012). The dilated cardiomyopathy patient with heart failure has also a reduced peak contractility with a much higher myocardial stiffness. This is also in agreement with the literature, where such differences in myocardial stiffness have been observed in DCM patients (Bortone et al., 1989). We also observe a smaller aortic resistance in this case, which is probably due to the patient's medical treatment pre-acquisition (vasodilator).

Therefore this preliminary study could assess
- the small relaxation rate k_{rs} as a characteristic of post-MI heart;
- the high stiffness c_1 and bulk modulus K as a possible clue of severe dilated cardiomyopathy;
- the small contractility σ_0 as a possible indication of heart failures.

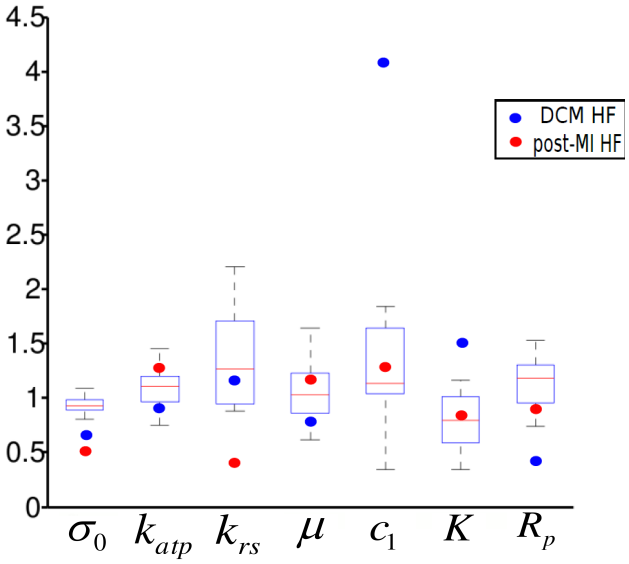

Figure 4.20: Box plot showing the median and variance of the parameters for seven healthy cases. The values are normalized by the mean parameter $\mathbf{X}^0$. The red and blue dots represent the parameters of the pathological cases.

The simulated Pressure-Volume diagrams are presented Fig. 4.21 and demonstrate the clear differences between volunteer cases and the heart failure cases.

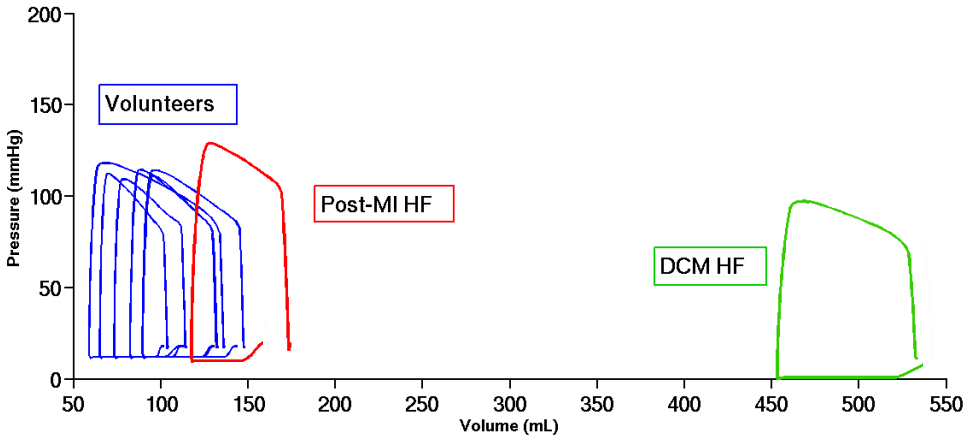

Figure 4.21: Simulated Pressure-Volume diagrams after calibration.

4.6 Discussion

In (Marchesseau et al., 2012a) we proposed an innovative calibration method of an electromechanical cardiac model. The complete model depends on 14 parameters that act on the active, passive and constraint components. The calibration based on Unscented Transform allowed us to give a fast initialization of 4 or 5 parameters, leaving the other 10 or 9 fixed to standard values. The choice of these 4 (or 5) parameters was made based on a sensitivity analysis on the volume variation and were confirmed by Singular-Value Decom-

position analysis. Since the calibration requires only to run several simulations in parallel to estimate these parameters followed by one additional simulated cycle to verify the results, it can easily be used as a preprocessing step before the application of more sophisticated personalization algorithms.

In (Marchesseau et al., 2012d), we extended this work. The calibration based on the Unscented Transform allowed us to tune 7 global parameters from volume and pressure curves, with a mean relative error of 11%. Moreover, the method gives good results using the same initial value $\mathbf{X}^0$ and the same sigma points for all the cases, which decreases the preprocessing time and enables a comparison of the calibrated parameters. However, results for the pathological cases could be improved by a better choice of the initial value $\mathbf{X}^0$. Studying more cases would help in defining the proper initial values in the different pathological cases.

The creation of a synthetic image sequence allowed us to measure the intrinsic error in estimating volume curves over time. Since this error is of the same order of magnitude as the one after model calibration on healthy cases, we can conclude that we could recover well the volume curve on the studied cases. Furthermore, the calibration provided consistent and plausible range of values for the parameters.

A preliminary study showed that results on pathological cases versus control cases were coherent with medical knowledge of the studied diseases. We can therefore give a first set of specific parameters to characterize these heart failure cases. In our cases, a small relaxation rate was found specific to ischemic heart failures, and a high passive stiffness was specific to a severe dilated cardiomyopathy. Moreover, the results confirmed that a small contractility is expected in heart failure cases. Additional pathological cases and observation quantities are required to further develop and validate the specificity study.

Moreover, volume and pressure curves provide basic information about the cardiac cycle. A larger set of parameters could be personalized by adding global or even regional motion indices such as radial, longitudinal or circumferential displacements or strains in the ventricles or AHA segments (defined by the American Heart Association).

Chapter 5

From Global Calibration to Local Personalization

Contents

Based on: This chapter explains the personalization strategy submitted in Marchesseau et al. (2013a).

Patient-specific cardiac modelling can help in understanding pathophysiology and predict therapy planning. However it requires to combine functional and anatomical data in order to build accurate models and to personalize the model geometry, kinematics, electrophysiology and mechanics. Personalizing the electromechanical coupling from medical images is a complex challenge. We use the Bestel-Clément-Sorine (BCS) electromechanical model of the heart, which provides reasonable accuracy with a reduced number of parameters compared to the available clinical data at the organ level. We propose a personalization strategy from cine MRI data in two steps. We first estimate global parameters

with an automatic calibration algorithm based on the Unscented Transform which allows to initialize the parameters while matching the volume and pressure curves. In a second step we locally personalize the contractilities of all AHA zones of the left ventricle using the Reduced Order Unscented Kalman Filtering on regional volumes. This personalization strategy was validated synthetically and tested successfully on 8 healthy and 3 pathological cases.

5.1 Introduction

In this chapter, the Bestel-Clément-Sorine cardiac model Bestel et al. (2001), further improved by Chapelle et al. (2012b) is used. It showed a good compromise between complexity and accuracy Marchesseau et al. (2012c), and a good predictive power under different pacing conditions Sermesant et al. (2012). The personalization of such mechanical models has been tackled by different approaches. Variational assimilation methods Delingette et al. (2012); Sainte-Marie et al. (2006) were used to locally estimate the active parameters (contractility, contraction and relaxation rates), Sequential Quadratic Programming Wang et al. (2009) to estimate the passive material stiffness, while Reduced Order Unscented Kalman Filtering aimed at estimating the contractility parameters Chabiniok et al. (2011); Moireau and Chapelle (2011b).

These methods have already led to promising results to estimate some model parameters from heart motion and therefore open the possibility to help cardiologists in planning their therapy. In this chapter we chose to tackle this issue in a different way. We propose to estimate the regional contractilities of the left ventricle based on measured *regional volumes* which has the advantages to smooth the registration errors and to be available on commercial softwares. We apply this strategy on a database consisting of eigh healthy subjects and three heart failure patients. To this end, we first calibrate the mechanical model using the Unscented Transform method proposed in Marchesseau et al. (2012a) from the left volume curve that we extract from the motion registered from cine MRI data. This allows a better initialization before further local personalization since we use sequential methods which are dependent on the intial values. Then we apply the Reduced Order Unscented Kalman Filtering (using Verdandi[1]) on the regional volumes measured on the LV endocardium. This strategy was successfully tested synthetically for contractility estimation and scars tissue detection, and on real cases.

5.2 Mechanical Personalization Strategy

Our BCS model depends on 14 global parameters that need to be estimated. To this end, we propose to first assess global values for the parameters using the Unscented Transform algorithm Julier and Uhlmann (1997) from global observed quantities (endocardial volume) as described in Marchesseau et al. (2012c); and then to use the ROUKF (Reduced Order Unscented Kalman Filter) personalization algorithm Moireau and Chapelle (2011b) implemented in Verdandi Chapelle et al. (2012a) from local measurements to assess more precisely the contractility per region (see Fig.5.1 for a representation of this pipeline).

[1] Verdandi is an opensource data assimilation library available at http://verdandi.gforge.inria.fr/. Chapelle et al. (2012a)

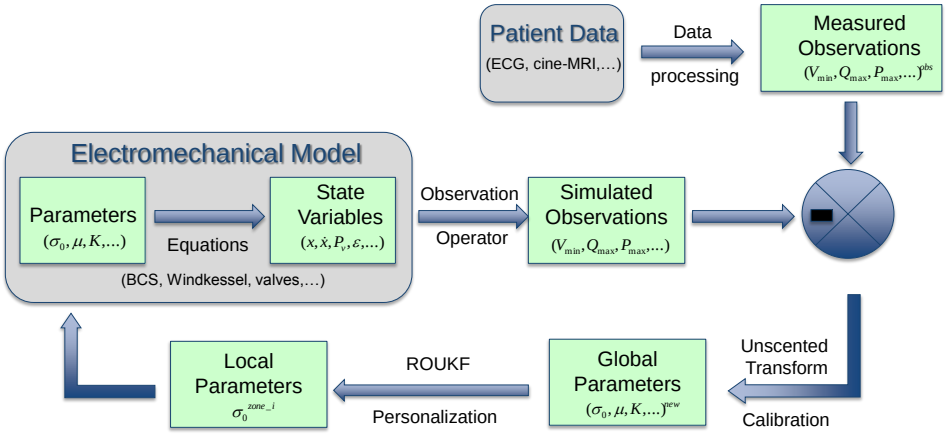

Figure 5.1: Personalization pipeline: combining the electromechanical model and the data to calibrate then personalize the parameters.

5.2.1 ROUKF Personalization Algorithm

Let us suppose that the mechanical parameters are well initialized from the calibration algorithm, the parameters can then be locally (regionally) estimated using a more advanced algorithm that deals with much larger dimensional systems. We use in this chapter a type of Kalman filter which belongs to the sequential data assimilation methods.

Data Assimilation Principles

Data assimilation methods intend to estimate state variables of the considered system using measurements. State variables consist usually of the trajectory (positions, velocities ,...) but can in fact include model parameters or other dynamical variables such as regional strains for instance. A model is therefore represented by a dynamical system governing the state variable $\mathbf{X}$ that includes the parameters of the model:

$$\begin{cases} \dot{\mathbf{X}} = \mathscr{A}(\mathbf{X}, t) \\ \mathbf{X}(0) = \mathbf{X}_0 + \xi_X \end{cases} \tag{5.1}$$

where $\mathscr{A}$ is a non-linear operator, $\mathbf{X}_0$ the *a priori* value for initial conditions and ξ_X the uncertainties in the initial conditions.

The available measurements are described through a linear observation operator $\mathbf{H}$. The observations are therefore modeled by the application of this operator:

$$\mathbf{Z} = \mathbf{H}\mathbf{X} + \chi \tag{5.2}$$

where χ is the observation noise.

Two types of assimilation methods exist: the sequential and the variational approaches. In the variational approach, a cost function is iteratively minimized after gathering measurements over a period of time. In the sequential approach, a new estimation of the state is performed each time a new measurement is available through statistical analysis. Both approaches have shown promising results in cardiac personalization: Billet (2010); Delingette et al. (2012); Sainte-Marie et al. (2006) that use the variational approach to estimate the contractility parameters or Xi et al. (2011); Chabiniok et al. (2011) that preferred the sequential approach). We use in this chapter the Unscented Kalman Filter in its reduced form,

derived in Moireau and Chapelle (2011b) since we only estimate the parameters.

Unscented Kalman Filtering

The Unscented Kalman Filter can be seen as an iterative Unscented Transform described in Chapter 4. It is based on three steps at each discrete time n, for the state vector $\mathbf{X}$ which consists in the state values (positions, velocities, ...) and the parameters θ.

- **Sampling**: Creates the sigma-points given an interpolation rule leading to $\mathbf{I}$, using a state error covariance matrix $\mathbf{P}$:

$$\hat{\mathbf{X}}_n^{(i)+} = \hat{\mathbf{X}}_n^+ + \sqrt{\mathbf{P}_n^+}\mathbf{I}^{(i)} \tag{5.3}$$

  were $\mathbf{X}^{(i)}$ is the ith component of vector $\mathbf{X}$.

- **Prediction**: Estimates the next state as the mean of the states simulated with the sigma-points, and the next covariance as the covariance of the states simulated with the sigma-points:

$$\begin{cases} \hat{\mathbf{X}}_{n+1}^- = E_\alpha\left(\mathbf{A}_{n+1|n}\left(\hat{\mathbf{X}}_n^{*+}\right)\right) \\ \mathbf{P}_{n+1}^- = Cov_\alpha\left(\mathbf{A}_{n+1|n}\left(\hat{\mathbf{X}}_n^{*+}\right)\right) \end{cases} \tag{5.4}$$

  where the mean E_α and the covariance Cov_α are calculated with the weights α_i of the sigma-points, and noting $\mathbf{X}^*$ the concatenation of the vectors $\mathbf{X}^{(i)}$.

- **Correction**: Updates the state vector and its covariance given the new sigma-points and corresponding observations using the new observation operator $\mathbf{H}$ and the covariance of the noise $\mathbf{W}$ through the following calculations:

$$\begin{cases} \hat{\mathbf{X}}_{n+1}^{(i)-} = \hat{\mathbf{X}}_{n+1}^- + \sqrt{\mathbf{P}_{n+1}^-}\mathbf{I}^{(i)} \\ \mathbf{Z}_{n+1}^{(i)} = \mathbf{H}_{n+1}\hat{\mathbf{X}}_{n+1}^{(i)-} \\ \mathbf{P}_\alpha^{X\tilde{Z}} = Cov_\alpha\left(\mathbf{X}_{n+1}^{*-}, \mathbf{Z}_{n+1}^*\right) \\ \mathbf{P}_\alpha^{\tilde{Z}} = \mathbf{W}_{n+1} + Cov_\alpha\left(\mathbf{Z}_{n+1}^*, \mathbf{Z}_{n+1}^*\right) \\ \hat{\mathbf{X}}_{n+1}^+ = \hat{\mathbf{X}}_n^- + \mathbf{P}_\alpha^{X\tilde{Z}}(\mathbf{P}_\alpha^{\tilde{Z}})^{-1}\left(\mathbf{Z}_{n+1} - E_\alpha\left(\mathbf{Z}_{n+1}^*\right)\right) \\ \mathbf{P}_{n+1}^+ = \mathbf{P}_{n+1}^- - \mathbf{P}_\alpha^{X\tilde{Z}}(\mathbf{P}_\alpha^{\tilde{Z}})^{-1}(\mathbf{P}_\alpha^{X\tilde{Z}})^T \end{cases} \tag{5.5}$$

Reduced Order Unscented Kalman Filtering

We aim, in this chapter, at estimating only the p parameters of the model. Therefore, we only generate $p+1$ sigma-points and the covariance $\mathbf{P}$ is reduced to the parametric space of dimension p. Its rank is therefore p much smaller that the dimension of the space d. We suppose that we can manipulate covariance matrices in the factorized form:

$$\mathbf{P} = \mathbf{L}\mathbf{U}^{-1}\mathbf{L}^T \tag{5.6}$$

where $\mathbf{U}$ is an invertible matrix of rank p and represents the main uncertainties of the system. A new derivation of the algorithm can therefore be performed without computing the full covariance matrix $\mathbf{P}$, as shown in Moireau and Chapelle (2011b); Moireau et al. (2008).

5.2.2 Observation Extraction from the Images

We suppose in this chapter that the deformed meshes registered from the cine-MRI are the only available measurements. Several types of observations can then be extracted from these meshes. Since the registration method focuses only on the visible contours in the image, we cannot expect the trajectory of all the points in the myocardium to be accurate, we will therefore only consider the points on the endocardial surfaces. Three types of observations can be derived directly from this:

Volume curve

First, for the calibration, the volume of the Left Ventricle is computed over time, giving the three required observations ($V_{min}, dV/dt_{min}$ and dV/dt_{max}). These observations are easily computed using the topology of the endocardium as explained in Marchesseau et al. (2012a). However it is not sufficient to recover the motion of the whole myocardium.

Positions on the Surface

The most complete observation include the positions of all the points on the endocardial surface. The estimation tries therefore to match the motion point-wise. The advantage of what we call the Surface-Points Estimation is that the observation operator $\mathbf{H}$ is straightforward, filled with 1 values on each coordinates of the surface nodes and 0 values otherwise. The main drawback is that there is no guarantee that the registration tracks displacements of material points, but rather apparent displacements of the contours, inducing therefore errors on the observations (well known aperture problem in Computer Vision). There exists observation operators Chabiniok et al. (2011) that filter this aperture issue taking into account distances between the surface contours. These methods give promising results but are not directly applicable for clinical context due to their computation times.

Regional Volumes

To tackle this issue, we suggest to use regional volumes as observations. To this end, we project the AHA volumetric segments (Fig.5.2) on the surfaces (LV endocardium and/or epicardium and/or RV endocardium depending on the needs), and calculate the volume formed by this surface and the barycenter of the LV endocardium over time. Not only does this method allow to capture the motion of the surface locally without smoothing tracking errors, but it also leads to a small number of observations to match, decreasing this way the computation time. Moreover, regional volumes are used by clinicians as a pathological index Baxley and Joseph Reeves (1971).

5.2.3 Error Measurements

In order to evaluate the errors between the estimated motion from the registration and the simulated motion, several error measurements are used. First, the result of the calibration algorithm compares the simulated volume curve $V^{simu}(t)$ to the registered volume curve $V^{obs}(t)$ using the standard root mean square difference:

$$\bar{\varepsilon}_V = \sqrt{\frac{\sum_{t=0}^{N_{steps}} \left(V^{simu}(t) - V^{obs}(t)\right)^2}{N_{steps}}} \tag{5.7}$$

where N_{steps} is the number of images in the MRI sequence. Then, after personalizing the model from regional volumes, we compare the simulated regional volumes $V_i^{simu}(t)$ to the

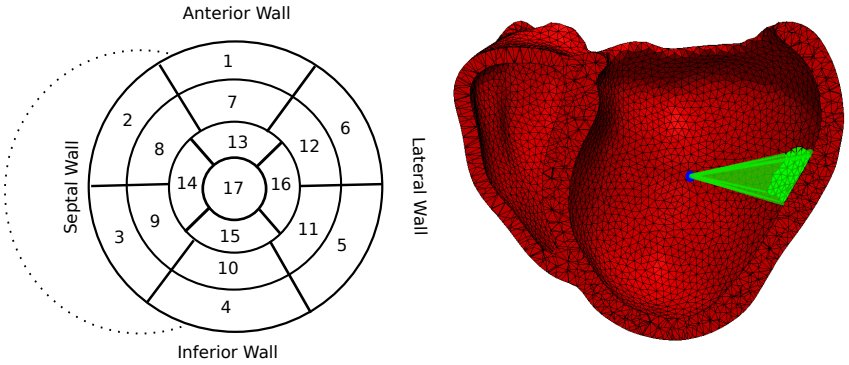

Figure 5.2: (Left) Bull's eye plots of the AHA 17 segment division (View from the apex). (Right) Example of Regional Volume.

registered ones $V_i^{obs}(t)$ normalized by the area of the AHA surface S_i to obtain a mean square difference for each regional volumes that we average:

$$\bar{\varepsilon}_{RegVol} = \frac{1}{N}\sum_{i=0}^{N}\frac{1}{S_i}\sqrt{\frac{\sum_{t=0}^{N_{steps}}\left(V_i^{simu}(t)-V_i^{obs}(t)\right)^2}{N_{steps}}}. \tag{5.8}$$

It is also interesting to record the distance error between the regional volumes at end-systole where it is maximal:

$$E_{RegVol} = \frac{1}{N}\sum_{i=0}^{N}\frac{\left|V_i^{simu}(T_{max})-V_i^{obs}(T_{max})\right|}{S_i}. \tag{5.9}$$

These errors give a good indication on how well the simulated motion match the registered one on the left endocardium. For a more global index that takes all the surfaces into account (including epicardium and right endocardium), we define a symmetric distance on the contours Ω as:

$$\begin{aligned}\varepsilon_C =& \frac{1}{2}\frac{\sum_{k=0}^{N_{points}} dist(\Omega^{simu}-\mathbf{P}_k^{obs})}{N_{points}} \\ &+ \frac{1}{2}\frac{\sum_{k=0}^{N_{points}} dist(\Omega^{obs}-\mathbf{P}_k^{simu})}{N_{points}}\end{aligned} \tag{5.10}$$

with a mean value over time noted $\bar{\varepsilon}_C$ and a value at end-diastole E_C.

5.3 Results

For this work, our database was made of eight healthy cases acquired at King's College London and made available to the community for the STACOM challenge 2011. Furthermore, we were provided with three pathological cases acquired at INSERM institute, selected for Cardiac Resynchronisation Therapy.

For all cases, the kinematic motion was estimated using the TDFFD algorithm which allowed to compute the real volume curves. Furthermore, Ensite data was acquired on the pathological cases allowing to have a personalized electrophysiology but no data on the pressure was available.

5.3.1 Selection of Adequate Observations

We tested the ROUKF algorithm to estimate the contractility for 6 zones of the left ventricle (combining the AHA segments as shown in Fig.5.3) on synthetic data, using two types of observations: the surface points and the regional volumes on the LV endocardium. To this end, the observations were created with a forward simulation of the model with different values of the contractility for each of these zones. The resulting deformed meshes are

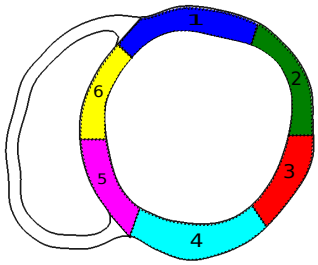

Figure 5.3: Division of the myocardium into 6 regions for the left ventricle and 1 for the right ventricle, combining the standard AHA zones. (View from apex)

compared with the ground truth on Fig.5.4 where we can see that both methods give an excellent match. In this case, since there are no errors on the data nor on the model, the only errors are due to the estimated parameters. The resulting estimated parameters are

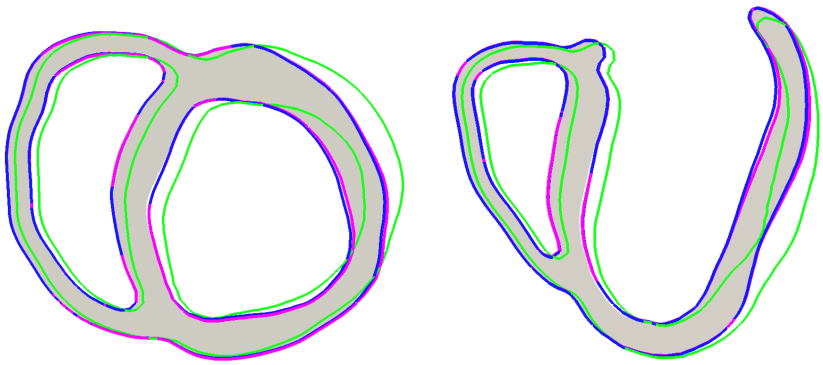

Figure 5.4: Comparison of the deformed meshes on short axis view from the base (left) and long axis (right) plane. Grey surfaces represent the ground truth, green contours the initial simulation, pink the estimated contours using regional volumes and blue the estimated contours using surface points. Since no clear difference can be made from the pink and blue contours, we conclude that both techniques give similar results and manage to match the ground truth.

given in Fig.5.5 for the two estimations and compared with the reference value. We can see that the parameters are better estimated with the regional volumes. To understand why observing regional volumes leads to better parameters than observing all the points of the surface, we evaluate the errors on these two types of observations (Surface Point error and Regional Volumes error) while varying the contractility of one zone around its ground truth value. Fig.5.6 gives the resulting mean errors. We can see that the Regional Volumes error has only one minimum whereas the Surface Points error has a non-smooth variation leading to several local minima in which the estimated parameters may be "trapped" in the filtering procedure. Of course, observability is enhanced when using pointwise displacements, hence

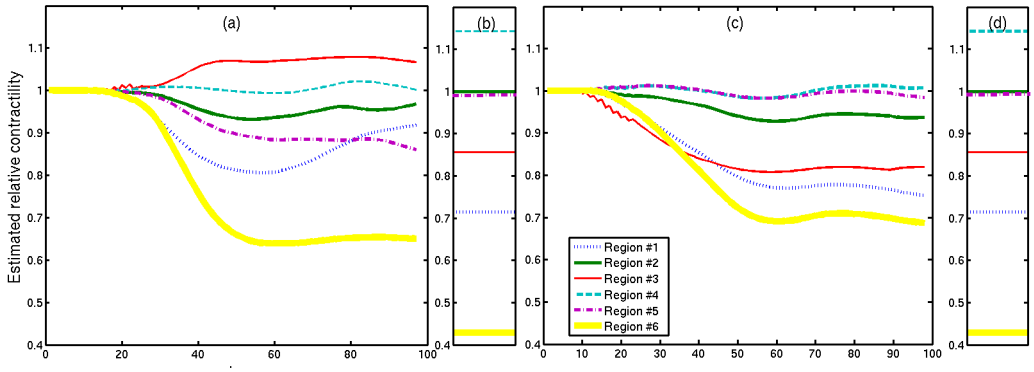

Figure 5.5: (a) Regional contractility estimation using observations on all the surface points. (b)(d) Reference values of the contractility. (c) Regional contractility estimation using observations on the regional volumes in the LV endocardium.

we conjecture that a finer tuning of the filtering method would overcome this difficulty, see Imperiale et al. (2011).

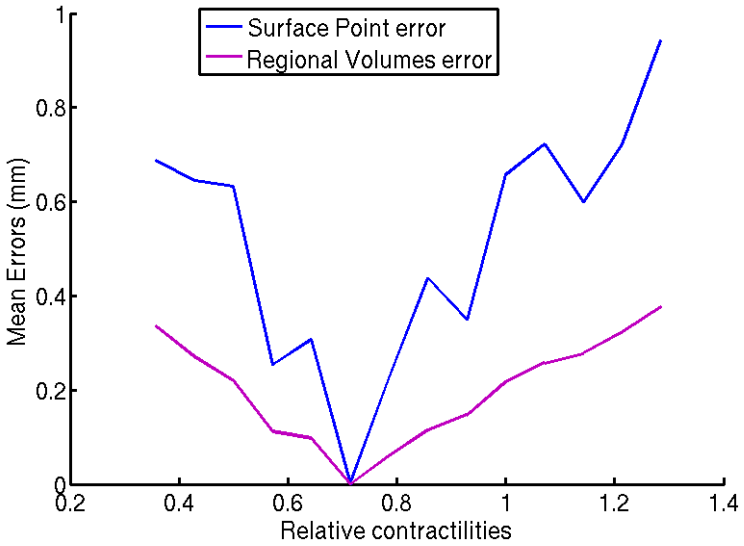

Figure 5.6: Comparison of the errors using the two types of observations, for various contractilities.

5.3.2 Detection of Infarcted Tissue

In this section, we test the ability of a personalized model to detect regions of low contractility, for instance due to presence of scars following an infarct. In order to evaluate the detection power of the proposed personalization based on regional volumes, a set of tests were performed using synthetic data. Forward simulations with varying size of scar tissue (from 300 tetrahedra to 2000 tetrahedra out of the 65 000 tetrahedra for the full myocardium) were performed to create the observations. The relative contractility was set to 0.3 for the scar zone and 1 for the rest of the myocardium. Before using the personalization algorithm, random noise was added on the regional volumes to obtain observations closer to what would be observed with real data. Moreover, to calibrate the ROUKF algorithm,

the expected maximum error must be set. To make this test realistic, an error of 0.5mm was allowed. This explains why the initial relative contractility of 0.3 cannot be reached. Resulting volumes curves compared to synthetic ones are shown in Fig.5.7.

The estimated contractilities obtained for the scars zone are presented Fig.5.8 for the var-

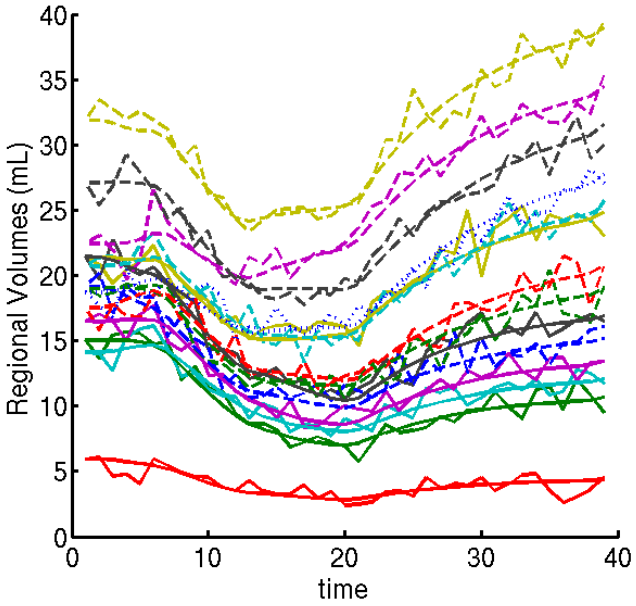

Figure 5.7: Regional Volumes simulated with 0% noise (smooth curves) and 10% noise (non-smooth curves).

ious sizes and noise amplitudes. We note that the noise does not influence the estimation of the parameter for scars zone larger than 1300 tetrahedra (as represented in Fig.5.8) but makes the detection impossible for smaller zones.

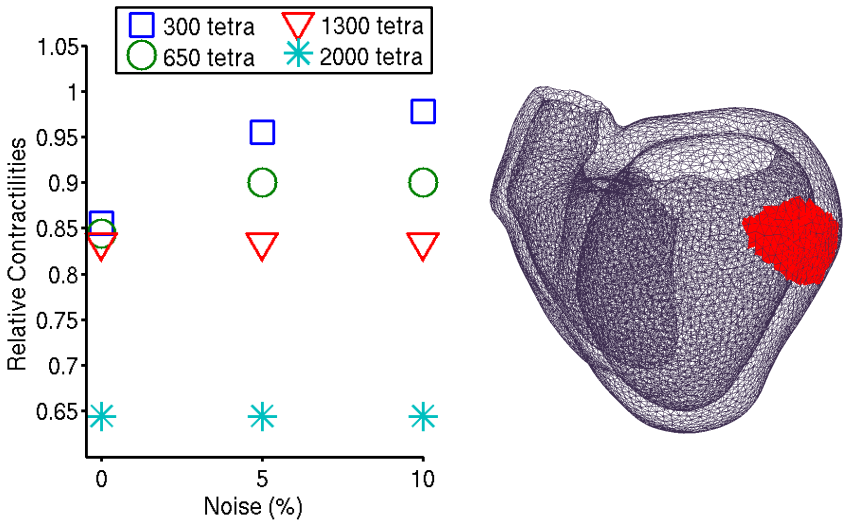

Figure 5.8: (Left) Estimated contractilities on the scars zones for different sizes of the zones and different noise. (Right) Representation of a scar zone of 1300 tetrahedra.

5.3.3 Real Cases Personalization

Personalizing real cases requires three steps:

- Selecting the region that has the smallest displacement (basal area or apex) in order to constraint this region as a boundary conditions.
- Performing a calibration of 4 parameters (including contractility) for the left ventricle, based on the volume curve.
- Running the ROUKF algorithm using regional volumes on the LV endocardium in order to estimate the 17 regional contractilities of the LV.

This pipeline was applied on 3 pathological cases and 8 healthy volunteers and enabled to draw preliminary conclusions on pathological cases versus healthy controls. Results of the full personalization strategy are detailed here for the pathological Case #1, then error measurements and estimated contractilities are given on all cases.

Results of the full personalization strategy are detailed here for the pathological Case #1, then error measurements and estimated contractilities are given on all cases.

Results for Case #1

First, volume curves resulting from the calibration are given in Fig.5.9. The mean error on the volume $\bar{\varepsilon}_V$ decreases from 17mL to 4mL giving therefore a good initialization.
Second, the results of the full personalization are given in Fig.5.10 where we compare the

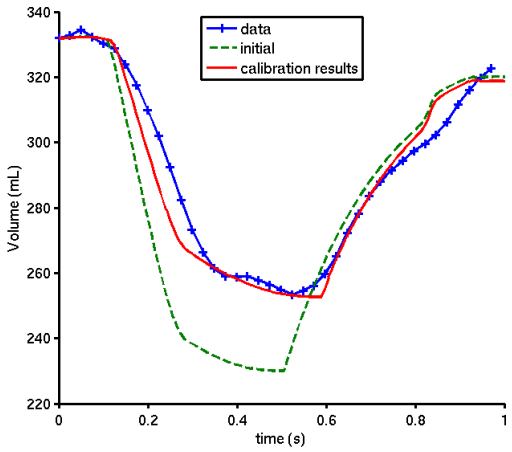

Figure 5.9: Case #1: Volume evolution before (green) and after (red) calibration compared with real value extracted from the registration (blue).

deformed mesh to the registered mesh and the images at end-systole, or in Fig.5.11 for the full cycle. The distance error on the contours ε_C is represented Fig.5.12 at end-diastole and shows how close the model follows the registered motion. The mean distance error on all the surface decreases from 2.8 mm to 2.1 mm which is a reasonable error given the image resolution (1.25 mm x 1.25 mm) and the fact that we only try to match the left endocardium.

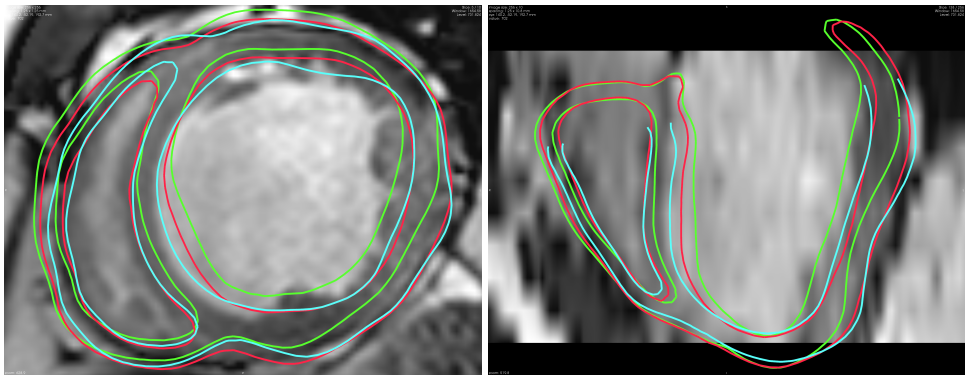

Figure 5.10: Short axis and long axis view of the end-systolic phase. Comparison of direct model with the initial parameters (green), direct model with the estimated contractilities on all left ventricle AHA zones using the regional volumes on the LV endocardium (red) and registered mesh (blue).

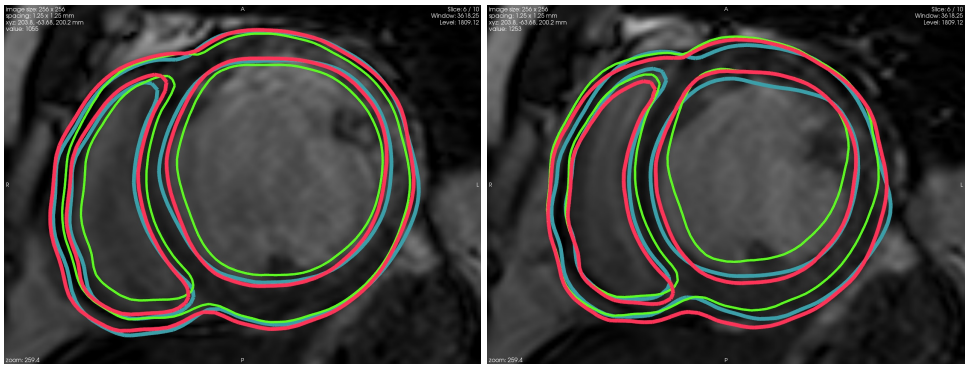

(a) 120 ms (b) 360 ms

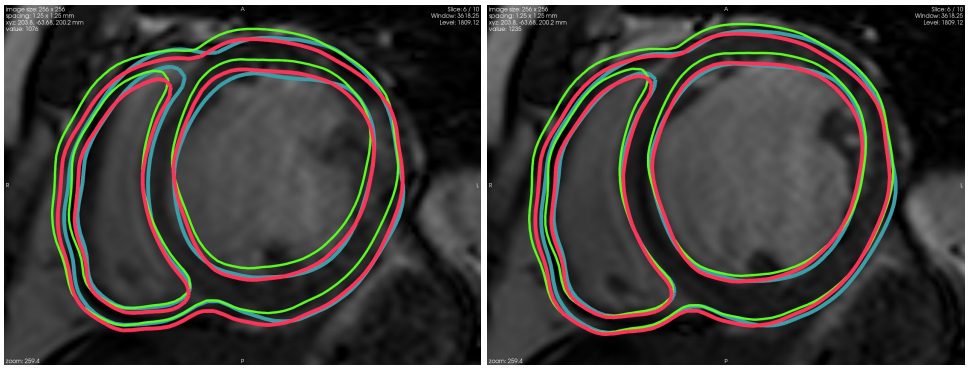

(c) 500 ms (d) 740 ms

Figure 5.11: Short axis view of the deformed meshes at various times of the cardiac cycle. Comparison of direct model with the initial parameters (green), direct model with the estimated contractilities on all left ventricle AHA zones using the regional volumes on the LV endocardium (red) and registered mesh (blue).

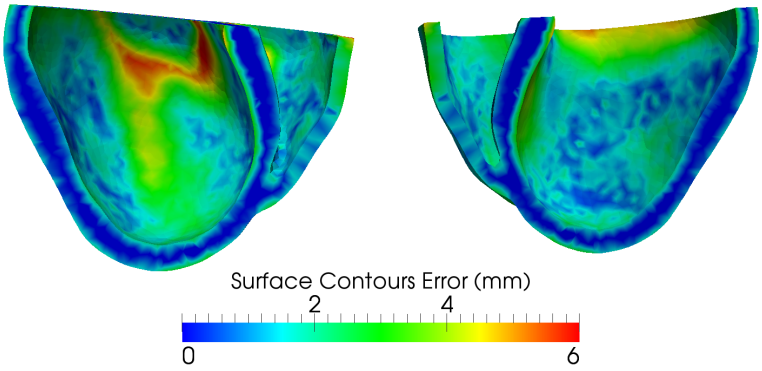

Figure 5.12: Case #1: Evaluation of the distance error on the contours of the surface at end-systolic phase (E_C). The basal area is cropped since we do not take the corresponding observations into account.

Registered and simulated regional volume curves are compared Fig.5.13. The mean relative error on the regional volumes (normalized by the surface area) decreases from $\bar{\varepsilon}_{RegVol} = 1.1\ mm$ with initial parameters to $\bar{\varepsilon}_{RegVol} = 0.6\ mm$ after personalization which proves a very good improvement. Finally, Fig.5.14 gives the estimated relative contractili-

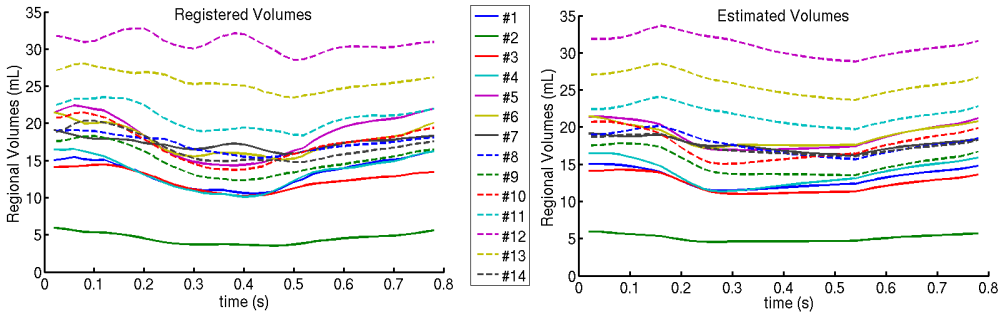

Figure 5.13: Case #1: (Left) Registered regional volumes on the LV endocardium. (Right) Estimated regional volumes.

ties along the personalization steps and shows that the estimation converges before the end of the personalization.

Error Measurements

In order to evaluate the accuracy of the personalized motion, we compute the errors previously defined on all the tested cases, before and after personalization. Fig.5.15 presents in (a) the resulting errors on the regional volumes $\bar{\varepsilon}_{RegVol}$ which is what is actually minimized during the personalization, as well as its value at end-systole (b). Finally, as an indicator of the global motion on all the surfaces, the distance error on the contours $\bar{\varepsilon}_C$ is given in (c). We can see that the personalization decreases the errors in all the cases and that the mean error on the regional volumes in pretty low (0.7mm) which is smaller than a pixel size. However, the error on the total surface still needs to be improved including observations from the right ventricle and the epicardium.

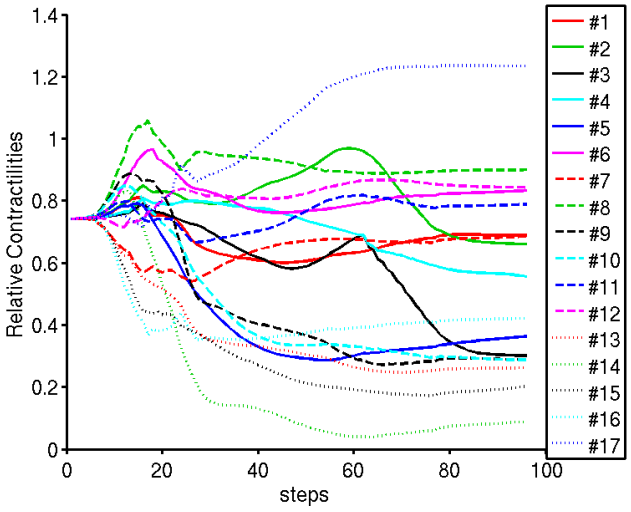

Figure 5.14: Case #1: Evolution of the estimated relative contractilities along the personalization steps. We note a mean relative contractility of 0.55. Contractility of zone #17 might be overestimated since it corresponds to the apex which is constrained by our boundary conditions.

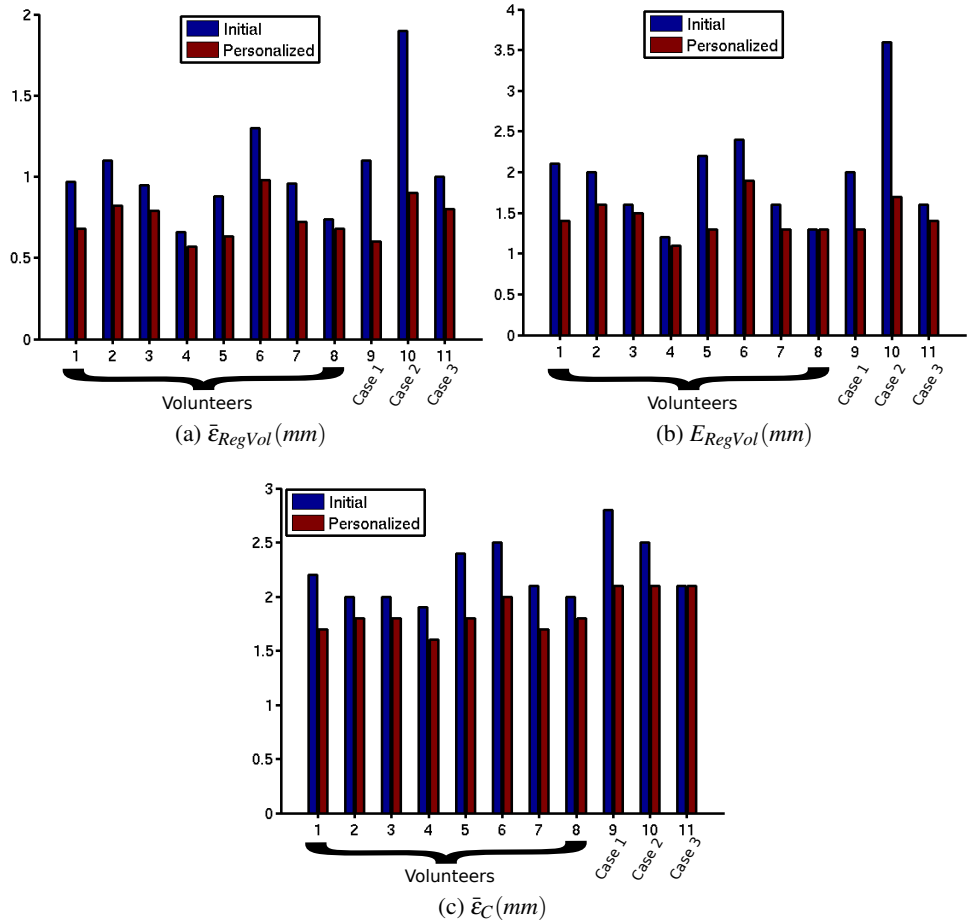

(a) $\bar{\varepsilon}_{RegVol}(mm)$ (b) $E_{RegVol}(mm)$

(c) $\bar{\varepsilon}_{C}(mm)$

Figure 5.15: Errors between the simulation and the registration before (in blue) and after (in red) personalization.

5.4 Preliminary Specificity Study

Our database consisting of 8 healthy controls and 3 pathological cases selected for the Cardiac Resynchronization Therapy (with therefore a small ejection fraction and a long QRS) allows to draw preliminary conclusions. First, from the global volume curves, a calibration was performed to initialize 4 parameters. The resulting parameters are presented in Fig.5.16. We can see from this graph that the Computational Biophysical Model Personalized for case 1 (CBMP#1) and case 2 (CBMP#2) exhibit a smaller global contractility than the healthy controls, and that the Computational Biophysical Model Personalized for the third case (CBMP#3) exhibits what seems to be a global contractility closer to the normal range, and a very high Bulk Modulus, meaning that the model of the myocardium muscle is stiffer in this case than the model describing the healthy cases. This could be explained by the fact that this patient has a different etiology than the first two cases (idiopathic cardiomyopathy) and, more importantly, has regurgitations at both the mitral and aortic valves. Furthermore, this patient presents significant atrial volumes, with an increased pulmonary artery pressure. This leads to a smaller inflow than outflow as shown in Fig.5.17. A

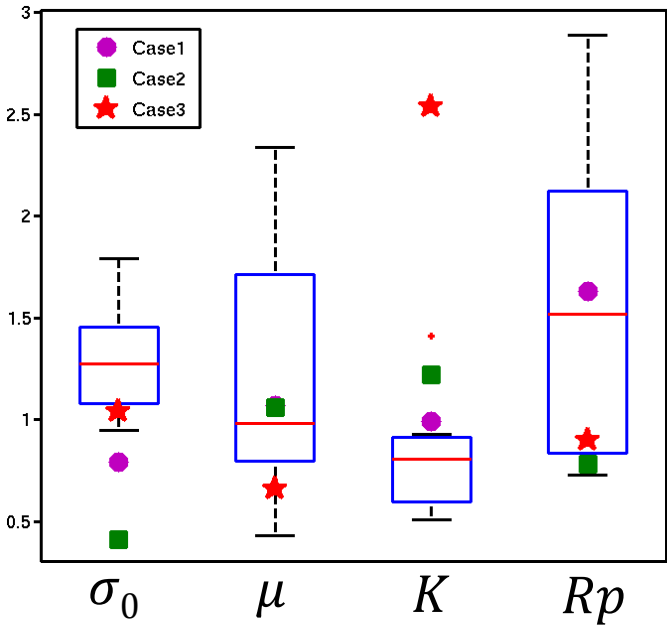

Figure 5.16: Estimated global parameters for the 3 pathological cases compared to the healthy controls(box plot). σ_0 is the global contractility, μ the friction parameter, K the Bulk modulus related to the stiffness of the passive myocardium and R_p the peripheral resistance in the aorta.

comparison of the regional contractilities obtained from the personalization method that we propose leads to consistent observations (see Fig.5.18). Indeed, the personalized regional contractilities of the first two cases are much smaller on all the regions than the controls. Moreover, CBMP#3 exhibits regional contractilities closer to the contractilities of healthy hearts for most regions. Some of the estimated contractilities however are extreme (zone 7 has a very small contractility while 17 has a very high contractility) which could indicate local dysfunctions. The study of the covariance on the parameters showed that our confidence on the contractilities of zones 1 to 6 and zone 17 is 4 times smaller than on the other zones due to the boundary constraints on the base and the apex that we set.

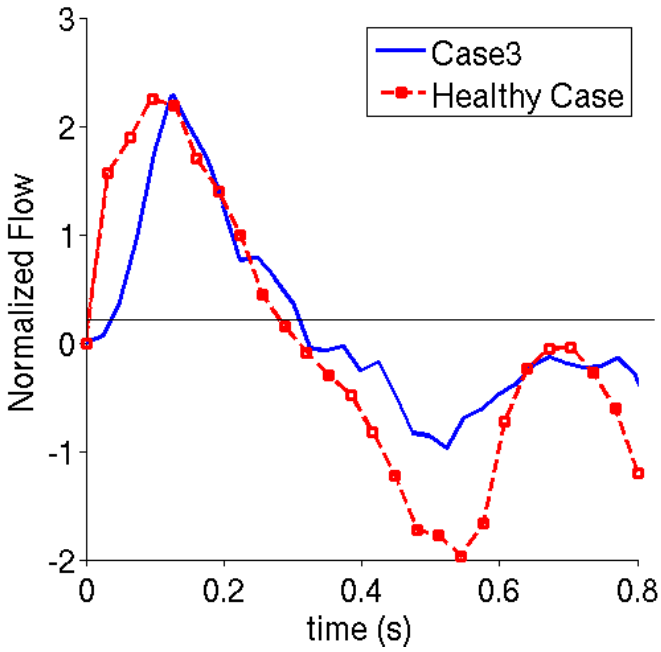

Figure 5.17: Registered flow curves for the pathological case 3 compared to one healthy case, showing an impared relaxation.

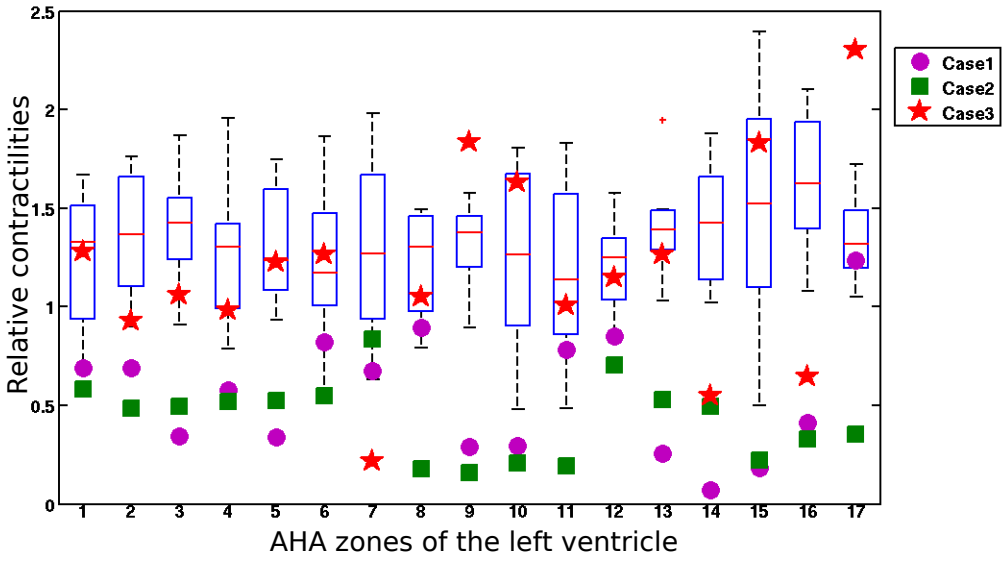

Figure 5.18: Estimated regional contractilities for the 3 pathological cases compared to the healthy controls (box plot).

5.5 Discussion

5.5.1 Personalization from Regional Volumes

In this paper we proposed patient-specific modelling of the heart based on regional volumes. Tests performed on synthetic data proved that this choice of observations was relevant to estimate regional contractilities and detect scar tissue as long as the size of the scar zone is not too small. The advantage of such an approach is to smooth the input observations in order to match the motion of the left endocardium. This method proved to be robust and can be used at a large scale. Indeed, although the regional volumes were rather different for pathological cases and healthy volunteers, we managed to estimate the regional contractilities and have a good final match on the motion. Finally estimating the regional volumes gives precious indices on the synchronization of the AHA zones which could be further studied for therapy planning.

5.5.2 Analysis of Real Case Personalizations

Our database of 3 pathological cases and 8 volunteers allows to draw some conclusions. First, the personalized computational biophysical models that intend to characterize these pathological cases exhibit different global contractility and/or stiffness. Our results on the calibration and on the regional personalization are consistent and show that CBMP#1 and CBMP#2 display a similar behavior (small estimated global and regional contractilities with normal estimated stiffness), while CBMP#3 is clearly different. First, CBMP#3 exhibits a reasonable global contractility parameter while showing a high stiffness which seems to explain its small ejection fraction and its small filling flow. Second, CMBP#3 estimated regional contractilities are for most of them similar to healthy cases with localized akinetic regions confirmed by the clinicians. In addition, this case, with a different etiology, was the one not responding to the CRT. Our personalization pipeline therefore gives results in agreement with the clinical interpretation of the images.

5.5.3 Limitations of the Personalization Pipeline

The proposed approach includes several processing and computational steps that are subject to uncertainties. First, we relied on image segmentation and tracking which are challenging due to the limited intensity constrast of the myocardium, and the aperture problem. Then, with the calibration, 4 global parameters could be assessed and the remaining 10 were set to their standard values which were chosen after a trial and error approach on one healthy case, or from the literature (more details and values can be found in (Marchesseau et al., 2012d)). Data on ventricular pressure would help the parameter estimation compared to using literature values that can be far from the actual patient condition. Second, boundary conditions play a significant role in the myocardium motion and hemodynamics, therefore they need to be assessed carefully. Our model includes a pericardium that constrains the outward radial motion and some elastic constraint that can be applied on the apex (which is either outside the field of view of the images, or barely moving) and on the basal area around the valves. However, the pre-load and the after-load were not personalised in this article which probably impacts the estimation of the parameters. For instance, modelling the regurgitations observed on the third pathological case could help in obtaining parameters closer to the actual intrinsic tissue properties of this patient. Finally, a time registration

between the real data and the simulation is necessary and influences as well the results of the personalization.

5.5.4 Perspectives

Our method only intends to recover the motion of the left endocardium. To improve the results of the personalization, or estimate more parameters such as the regional stiffness for instance, one may include the regional volumes calculated from the epicardium and intend to recover the thickening and shrinking of the muscle or estimate the parameters related to the boundary conditions. Using measurements on the regurgitation would also improve the personalization since our heamodynamic model that represents the pressure constraint (Marchesseau et al., 2012a) can include regurgitation by estimating the iso factor K_{iso}. Alternatively, we could couple this heamodynamic constraint with a lumped-flow model as used by (Koon et al., 2010). Moreover, we could divide the endocardium in different zones than the standard AHA zones in order to obtain more precise results. Applying this method on a larger database could also lead to better assessment of the parameters specificity of the personalized models. Finally, the proposed method could also help in testing the acute response to pacing by simulating it on the personalised model.

5.6 Conclusion

This paper proposes a personalization strategy made of a global calibration and the application of the Reduced Order Unscented Kalman Filter to estimate regional contractilities based on regional volumes using a complete model of the heart. The personalization of 3 pathological cases and 8 volunteers shows the robustness of this strategy and opens up possibilities to study the specificity of the estimated physiological parameters to the etiology and the response to CRT. The use of regional volumes allows to smooth registration errors and to find a good compromise between the physiological behavior of the model and the accuracy of the personalization.

Chapter 6

Conclusions and Perspectives

Contents

Each chapter of this manuscript contains conclusions on the performed work and perspectives. We now conclude on the main achievements of this PhD work. Then, we describe the collaborative projects in which we participated. Finally, we suggest possible improvements related to this work.

6.1 Main Contributions

6.1.1 Implementation of the BCS Model

We decided to have our own implementation of the existing Bestel-Clément-Sorine model for several reasons. Indeed, using SOFA platform allows fast computation, interactivity and modularity. Fast computation is necessary in order to be able to test many personalization methods, but also for the foreseen clinical applications. For surgery training or interactive therapy planing, a real-time simulator would be ideal. We have not reached this point but we manage to run a cycle in less that 20 minutes (with a time step of 7ms). Modularity

enables to modify components of the model without any change in the other components. Since modelling the cardiac mechanics is still an open challenge, this is a valuable asset.

However, implementing the complete model in a modular way is a fairly challenging task. As explained in Chapter.3, boundary conditions, pressure constraints and so on had to be written in a "SOFA forcefield" way. In particular, to solve the dynamical system under constraint (and therefore take into account the four cardiac phases), a complex prediction-correction algorithm has been considered as an alternative to Lagrangian Multipliers not available on SOFA.

SOFA allowed finally to include a pericardium as a boundary to the model, which is as far as we know, one of the most realistic boundary condition implemented in the cardiac modelling community.

The model is now used inside (Prakosa et al., 2012) and outside of Asclepios team (see Sec.6.2.3).

6.1.2 MJED Method for Hyperelasticity

We proposed an innovative and generic method to discretize hyperelastic materials on finite elements meshes. The MJED method has been successfully tested on all known hyperelastic materials. The widely used linear elastic simplification for soft tissue modelling is no longer necessary. The source codes of this method were already made available on SOFA and used within the SOFA community (Courtecuisse et al., 2010; Peterlík et al., 2011).

We first applied the MJED method to liver surgery simulation and reach real-time interaction using only CPU. Moreover, we performed rheological experiments to find the parameters and confirm the accurate behavior of the liver model under deformation (see Appendix A). Finally, the MJED method was used as the passive part of the cardiac electromechanical model.

6.1.3 Calibration of the Mechanical Model

We proposed an automatic method to estimate the global parameters of the electromechanical model from simple indices of the volume and pressure curves after performing a complete sensitivity analysis. This method was applied successfully on several healthy and pathological cases from the same initial value. Not only did the calibration allow to initialize parameters before a local personalization and replaces therefore the widely used manual calibration, but it also led to a preliminary specificity study. We could therefore compare the mechanical parameters between control (volunteer) cases and pathological cases and reached conclusions in agreement with literature and medical knowledge. It could therefore be easily applied in the medical context to classify the pathologies for instance. This method was used by Prakosa et al. (2012) which intends to estimate the electrophysiological properties of the pathological cases.

6.1.4 Personalization of the Mechanical Model

We proposed a personalization strategy in two-steps. First, the calibration algorithm was applied to globally estimate the main mechanical parameters from volume and pressure curve. Second, a more complex data assimilation algorithm was used to estimate regional contractilities on the left ventricle based on registered regional volumes. This strategy proved to be robust to the various motion tracking algorithm since it enables to smooth the input

data. We applied this personalization method on 3 pathological cases and 8 healthy controls and manage to recover the myocardium deformation with reasonable accuracy. Moreover, a comparison of the estimated contractilities allowed to draw preliminary conclusions on non-responders to CRT.

6.2 Collaborative Work

This PhD work was partially funded by two European projects, and was performed in collaboration with several research teams, universities and hospitals.

6.2.1 Liver Surgery Simulation: PASSPORT Project

The PASSPORT project (PAtient Specific Simulation and PreOperative Realistic Training for liver surgery)[1] is a collaborative project made of several European surgical teams, research teams in surgical simulation and companies in surgical instrumentation. PASSPORT for Liver Surgery aims at offering a patient-specific simulator that would be used for surgical training or surgery planning. The "Virtual liver", developed in the Open Source SOFA platform will include modelling combining anatomical, mechanical, biological preoperative functions as well as realistic appearance.

In this project, our goal was to model the mechanical behavior of the liver. For this we had to find a good compromise between accuracy and computation time since the simulator has to work in real-time for surgery training (see Appendix A). The MJED method was developed to deal with the real time issue, a visco-poro-hyperelastic model of the liver was proposed as one of the most complete and accurate model. Finally, a collaboration with the University of Strasbourg (FRANCE) enabled to validate the model and the implementation from real experiments on 60 pig livers. This work led to two publications (Marchesseau et al., 2010b) and (Marchesseau et al., 2010c), deliverable and presentations for the annual meetings.

6.2.2 Cardiac Resynchronization Therapy: euHeart Project

The euHeart Project[2] (integrated cardiac care using patient-specific cardiovascular modelling) is a European Project that aims at building patient-specific model of the heart in order to treat cardiovascular diseases. Integrating the computing tools in the medical environment is the leading goal of euHeart which is an acting project. This is why 17 industrial, clinical and academic partners worked together to acquire data, process the data, build and simulate models, personalize the models, virtually test the therapy, validates results with data.

In this project, our goal was to build patient-specific models of the myocardium so as to be able to plan Cardiac Resynchronization Therapy. To this end, we used data from King's College London and INSERM in Rennes, UPF Barcelona processed the data so as to give us a mesh and registration. We also collaborated with INRIA Rocquencourt to design data-assimilation algorithms based on the Verdandi library. A collaborative paper (Tobon-Gomez et al., 2012a) summarizes some advances made by all the partners (of the WP5 work package) on CRT planning, and we published two papers in collaboration with KCL

[1] http://www.passport-liver.eu/Homepage.html
[2] http://www.euheart.eu/

(Marchesseau et al., 2012c,d) and submitted one paper also in collaboration with UPF and INSERM (Marchesseau et al., 2013a).

6.2.3 Cardiac Model: cMAC2 Challenge

In the scope of the STACOM challenge 2012 [3], and in particular the Motion Tracking Challenge, synthetic 3D ultrasound images were created and then distributed to the challengers. To create these images, a collaboration between Philips Research Medisys, CHU (hospital) in Caen, and Asclepios team was made. The electromechanical model of the heart that we implemented on SOFA was used to deform initial meshes, given various electrical patterns and changing mechanical parameters so as to synthetically create pathological cases. The deformation fields extracted from the simulations were then applied to real image sequences in order to create new image sequences. The realistic results proved that the model manages to represent healthy cases as well as pathological cases. Craene et al. (2012) explains the process for the creation of the synthetic data.

6.3 Perspectives

6.3.1 Model Improvements

Although the implemented model includes several important physiological features (a pericardium, a valve model to deal with blood flow, two ventricles, passive hyperelasticity, the fiber elasticity and the Sterling effect), several improvements can be performed. For instance, for now, the pericardium is a fixed surface that prevents the myocardium from leaving the allowed space. However, images clearly show that the pericardium has an elastic behavior, we could therefore include some elasticity in this component.

Furthermore, the current heamodynamic model that represents the blood flow during the four cardiac phases could be improved in two ways. First, fluid dynamics could be simulated in SOFA for a more physiological behaviour. Unfortunately, current methods for fluid dynamics are computationally expensive so this solution may not be doable in the scope of CRT planning. Second, we could use the CircAdapt model presented by Arts et al. (2005) which links flow and pressure of all the left ventricle to those of the right ventricle through a complete circulation model. This would lead to a more coherent way of determining the atrial and venous input pressures.

The modelling of the mechano-electrical feedback would also be an interesting improvement. We could also think of explicitly modelling the valves (Mansi et al., 2012) in order to simulate pulmonary regurgitation or mitral surgery. We would also gain in using a more complex electrophysiological model. Finally, the simulation greatly depends on the fiber fields, it is therefore crucial to improve the generation of the fibers(Lombaert et al., 2011).

6.3.2 Calibration of the Model

Only the left ventricle is calibrated using the proposed calibration algorithm for two reasons. First, the endocardial pressures are rarely available for the right ventricle since it is an invasive measurement. Moreover, the simulated and the registered volumes are close

[3] http://www.physense.org/stacom2012/

enough for the left ventricle so that simple indices such as the minimum of the volume and the slopes were sufficient to match the volume. However, this is not true for the right ventricle. The registration is very challenging for the right ventricle and so is the segmentation which is post-processed to add a wall thickness. Therefore the volume extracted from the registration is not smooth enough to be represented by the chosen indices. A better choice of indices should be defined in order to calibrate the right ventricle as well.

The calibration intends to match the volume and the pressure curve but gives no guarantee about the movement of the myocardium. We could improve this technique taking into account global measurements of the motion, such as the maximum radial strain, or the maximum longitudinal deformation ... It would probably ease the personalization which deals with the movement.

Finally, the same initialization is used for all cases. This has the advantage of making the calibration automatic, but also the drawback that pathological cases could be better calibrated if the initialization was closer to the real data. It could be interesting to study more pathological cases and more pathologies in order to determine an initialization set per pathology.

6.3.3 Personalization of the Model

In the proposed study, the left endocardium only is personalized based on its regional volumes. Although the results are promising, more parameters (other than contractility) could be estimated if more observations were taken into account. For instance, it could be interesting to measure the local thickness of the muscle in order to estimate passive parameters, or even longitudinal, radial and circumferential regional displacements.

During this study, we faced issues concerning the motion tracking. Indeed, even if the regional volumes smooth the input data, a bad tracking of one region can lead to a non-physiological volume curve which is impossible to match and may prevent the complete personalization. Therefore, the selection of the regional volumes to match influences the results and it would be interesting to adapt the algorithm and to assess confidence measure at each regional volume to take into account the registration uncertainties. It would also be interesting to study the impact of the registration algorithm on the estimated parameters.

Finally, a large database of pathological and healthy cases should be studied in order to draw significant conclusions that could then help in predicting responders versus non-responders, or pacing location.

6.3.4 Effects of the Therapy

Our goal in this thesis has been to make every steps of the personalization pipeline automatic for its application in the medical practice. We made significant progress towards this goal and we hope that it will soon be applied on a larger scale. However, we have not yet studied the effects of the therapy (Cardiac Resynchronization Therapy for instance) on the patient-specific models. This is definitely the next step to reach so as to be able to optimize the leads configuration of the pacemaker, or select potential responders to the therapy. Moreover, it would be interesting to predict the remodelling after the therapy. However, a modification of the current model might be necessary before this can be considered.

6.4 Conclusion

Through this thesis study, we showed that important advances have been made in the patient-specific biomechanical modelling of the heart. The results we obtained are promising and we hope that after further future improvements, such models and personalization methods could be used in a clinical environment. Although our research was focused mainly on Cardiac Resynchronization Therapy, the same pipeline of methods can be used for other types of cardiac disorders. However, more research work is required to tackle the issues we faced at each step of this work flow (segmentation, registration, modelling ...) before its integration in the medical practice.

List of Publications

The presented work led to several published and submitted publications as a first author and a co-author.

Book Chapters

- *This book chapter (in French) summarizes the existing methods to personalize electromechanical models of the heart from various types of data.*
  Marchesseau, S., Sermesant, M., Billet, F., Delingette, H., and Ayache, N. (2013b). Personnalisation de modèles électromécaniques du coeur par assimilation de données cliniques hétérogènes. In *Analyse d'images cardiaques et thoraciques*. Hermes. In French, Under Review

- *This chapter details the various components of SOFA platform and gives examples of biomechanical applications including heart modelling.*
  Faure, F., Duriez, C., Delingette, H., Allard, J., Gilles, B., Marchesseau, S., Talbot, H., Courtecuisse, H., Bousquet, G., Peterlik, I., et al. (2012). SOFA: A Multi-Model Framework for Interactive Physical Simulation. *Soft Tissue Biomechanical Modeling for Computer Assisted Surgery*, pages 283–321

Journal Papers

- *A strategy to personalize electromechanical models of the heart from regional volumes is proposed in this paper and applied on 8 healthy and 3 pathological cases.*
  Marchesseau, S., Delingette, H., Sermesant, Cabrera-Lozoya, R., Tobon-Gomez, C., Lekadir, K., Figueras, R., Frangi, A., Rhode, K., Duckett, S., Rinaldi, C., Razavi, R., Leclercq, C., Donal, E., Hernandez, A., Garreau, M., Moireau, P., Chapelle, D., and Ayache, N. (2013a). Personalization of a Cardiac Electromechanical Model using Reduced Order Unscented Kalman Filtering from Regional Volumes. *Submitted to Medical Image Analysis*

- *In this paper we apply the calibration method to healthy and pathological cases in order to compare the estimated global parameters in a specificity analysis.*
  Marchesseau, S., Delingette, H., Sermesant, M., Sorine, M., Rhode, K., Duckett, S., Rinaldi, C., Razavi, R., and Ayache, N. (2012d). Preliminary Specificity Study of the Bestel-Clément-Sorine Electromechanical Model of the Heart using Parameter Calibration from Medical Images. *Journal of the Mechanical Behavior of Biomedical Materials*

- *The full methodology of the proposed calibration method and its validation with synthetic and healthy cases is provided in this paper.*
  Marchesseau, S., Delingette, H., Sermesant, M., and Ayache, N. (2012a). Fast Parameter Calibration of a Cardiac Electromechanical Model from Medical Images based on the Unscented Transform. *Biomechanics and Modeling in Mechanobiology*, pages 1–17

- *In this paper we propose a new fast finite element method to compute hyperelastic materials and apply it to real-time liver surgery simulation.*
  Marchesseau, S., Heimann, T., Chatelin, S., Willinger, R., and Delingette, H. (2010b). Fast porous visco-hyperelastic soft tissue model for surgery simulation: application to liver surgery. *Progress in Biophysics and Molecular Biology*, 103(2-3):185–196

- *A method to perform fast simulations of the cardiac electrophysiology and its coupling with mechanics is provided in this paper.*
  Talbot, H., Marchesseau, S., Duriez, C., Sermesant, M., Cotin, S., and Delingette, H. (2012b). Interactive Electromechanical Model of the Heart for Rehearsal in the Context of Cardiac Resynchronization Therapy. *Interface Focus*

- *This paper proposes a new approach to generate synthetic cardiac images from an electromechanical model of the heart.*
  Prakosa, A., Sermesant, M., Delingette, H., Marchesseau, S., Saloux, E., Allain, P., Villain, N., and Ayache, N. (2012). Generation of Synthetic but Realistic Time Series of Cardiac Images Combining a Biophysical Model and Clinical Images. *IEEE Trans. Med. Imaging*

- *This paper details the latest progress in CRT planning, from the segmentation to the personalized simulation involving all partners of workpackage 5 in euHeart project.*
  Tobon-Gomez, C., Duchateau, N., Sebastian, R., Marchesseau, S., Donal, E., De Craene, M., Pashaei, A., Relan, J., Steghofer, M., Lamata, P., Camara, O., Delingette, H., Duckett, S., Garreau, M., Hernandez, A., Rhode, K. S., Sermesant, M., Ayache, N., Leclercq, C., Razavi, R., Smith, N., and Frangi, A. F. (2012a). Understanding the mechanisms amenable to CRT response: from pre-operative multimodal image data to patient-specific computational models. *Medical & Biological Engineering & Computing*

Conference Papers

- Marchesseau, S., Delingette, H., Sermesant, M., Rhode, K., Duckett, S., Rinaldi, C., Razavi, R., and Ayache, N. (2012c). Cardiac Mechanical Parameter Calibration based on the Unscented Transform. In *Proc. Medical Image Computing and Computer Assisted Intervention (MICCAI'12)*, volume 7511 of *LNCS*. Springer

- Marchesseau, S., Heimann, T., Chatelin, S., Willinger, R., and Delingette, H. (2010c). Multiplicative Jacobian Energy Decomposition Method for Fast Porous Visco-Hyperelastic Soft Tissue Model. In *Proc. Medical Image Computing and Computer Assisted Intervention (MICCAI'10)*, volume 6361 of *LNCS*, pages 235–242, Beijing, China. Springer

- Craene, M. D., Allain, P., Gao, H., Prakosa, A., Marchesseau, S., Hilpert, L., Somphone, O., Delingette, H., Makram-Ebeid, S., Villain, N., D'hooge, J., Sermesant, M., and Saloux, E. (2012). Synthetic and Phantom Setups for the Second cardiac Motion Analysis Challenge (cMAC2). In *Proc. MICCAI Workshop on Statistical Atlases and Computational Models of the Heart: Imaging and Modelling Challenge (STACOM12)*, LNCS. Springer

Abstracts

- Talbot, H., Marchesseau, S., Duriez, C., Courtecuisse, H., Relan, J., Sermesant, M., Cotin, S., and Delingette, H. (2012a). Interactive Electromechanical Model of the Heart for Patient-Specific Therapy Planning and Training using SOFA. *Virtual Human Project (VPH)*

- Marchesseau, S., Delingette, H., Sermesant, M., Rhode, K., Duckett, S., Rinaldi, C., Razavi, R., and Ayache, N. (2012b). Calibration of a Cardiac Electromechanical Model using the Unscented Transform from Medical Images. *Cardiac Physiome Workshop 2012*

Deliverable

- Marchesseau, S., Delingette, H., Peterlik, I., Cotin, S., and Faure, F. (2010a). Technical report on first results on new sofa modules development. Technical Report PASSPORT WP6: D 6.1

Awards

- Young Scientist Award at MICCAI conference 2012.

Appendix A

Fast poro-visco-hyperelastic model for liver surgery simulation

Based on: (Marchesseau et al., 2010c) and (Marchesseau et al., 2010b) that present a new poro-visco-hyperelastic model of the liver that can be simulated in real-time thanks to the MJED method. This appendex describes the model and the results published in those two papers. The MJED method describes in 3.3 is not repeated here.

Understanding and modeling the liver biomechanics represents a significant challenge due to its complex nature. Our contribution tackles this issue in the context of real time surgery simulation where a compromise between biomechanical accuracy and computational efficiency must be found. We describe a realistic liver model including hyperelasticity, porosity and viscosity that is implemented within an implicit time integration scheme. To optimize its computation, we introduce the Multiplicative Jacobian Energy Decomposition *(MJED) method for discretizing hyperelastic materials on linear tetrahedral meshes which leads to faster matrix assembly than the standard Finite Element Method. Visco-hyperelasticity is modeled by Prony series while the mechanical effect of liver perfusion is represented with a linear Darcy law. Dynamic mechanical analysis has been performed on 60 porcine liver samples in order to identify some visco-elastic parameters. Finally, we show that liver deformation can be simulated in real-time on a coarse mesh and study the relative effects of the hyperelastic, viscous and porous components on the liver biomechanics.*

A.1 Introduction

The simulation of soft tissue deformation has attracted a growing interest in the past 15 years both in the biomechanics and the medical image analysis communities. Indeed, medical image modalities such as MRI, CT or echography can describe with millimeter accuracy the anatomical shape of soft tissues but also their deformation through time series of images such as cine-MRI or echocardiography. Modeling *in silico* the deformation of soft tissues is of high interest in particular for the following applications: surgical gesture training (Delingette and Ayache, 2004), therapy planning (Hawkes et al., 2005), physically-based image registration (Veress et al., 2005) as well as medical imaging diagnostics.

We focus here on the simulation of liver deformation in the context of surgery training.

The overall objective is to build a simulator that can ease the training of young medical residents to perform some gestures specific to minimally invasive surgeries such as laparoscopy, endoscopy, interventional radiology, etc. In such cases, it is imperative that soft tissue deformation be simulated in real-time, *i.e.* at 25 frames per second which is the standard rate used in cinema since The Lumière brothers. Obviously with such performance, the simulation algorithms used in surgical simulators can also be used for surgery planning or even computer animation. However, in surgery simulation, there are additional constraints of numerical stability during the occurrence of contact between soft tissue and (virtual) surgical instruments. Because those instruments are controlled by a human operator, large compression or extension of tissue can occur, sometimes leading to non physical behavior such as inverted elements.

Because soft biological tissue behavior is rather complex and also not well characterized, its simulation in real-time is a very challenging task. The liver for instance is a porous material which typically undergoes large displacements, large deformations and is also strongly visco-elastic (more details in section A.3). Early approaches for modeling the soft tissue behavior assumed a linear elastic behavior (Cotin et al., 2000) discretized on finite elements which naturally leads to solving a linear system of equations whose inverse could eventually be precomputed (James and Pai, 1999).

Since linear elastic materials are not suited for large displacements, several authors in computer animation have proposed corotational elastic models (Müller et al., 2002; Nesme et al., 2005) where linear elastic stiffness matrices are rotated for each element. Those corotational models however do not minimize a strain energy and therefore are not the discretization of a continuum formulation. Also, their behavior is very restricted to material linearity.

To simulate realistic soft tissue deformation, several authors have employed hyperelastic materials minimizing a continuum strain energy. For real-time computation, early approaches have been based on St Venant Kirchhoff materials (Delingette and Ayache, 2004) which exhibit a linear stress-strain relationship. Significant speed-up can be obtained by using reduced basis of deformation (Barbič and James, 2005) or by grouping expressions on edges, triangles and tetrahedra (Picinbono et al., 2003) when discretized on linear tetrahedra. Those approaches are however limited to this specific material which has the drawback of not behaving well under compression.

For general hyperelastic materials, several authors have relied on the Finite Volume Method (Teran et al., 2003) to simulate soft-tissue deformation with explicit time integration schemes. Similarly, Miller et al. (2006) have proposed the *Total Lagrangian Explicit Dynamic* (TLED) algorithm for which elastic forces are based on the reference configuration unlike the *Updated Lagrangian* method widely used in commercial FEM code. This approach has been combined with Prony series to model visco-elasticity and has been implemented on Graphics Processing Units (GPU) (Taylor et al., 2009) to reach real-time computations. However the main limitation of this approach is that it relies on explicit time integration schemes which greatly simplifies the update at each time step but requires small time steps to keep the computation stable especially for stiff materials. Furthermore, with explicit schemes it is necessary to iterate multiple times to propagate applied forces from a node to the whole mesh.

In this article, we first introduce the *Multiplicative Jacobian Energy Decomposition* (MJED): a general algorithm to implement hyperelastic materials based on total Lagrangian FEM with implicit time integration schemes. An optimized approach to build the stiffness

matrix is proposed which is used to solve a linear system of equations at each time step. Our algorithm allows to perform some matrix precomputations thanks to a decomposition of the strain energy isolating the determinant of the deformation gradient J and the combination of shape vectors with fourth order elasticity tensors. Furthermore, a specific regularization of the stiffness matrix allows to cope with highly compressed elements.

A second contribution of this article is to propose a realistic biomechanical model of the liver which combines hyperelasticity, viscoelasticity as well as porelasticity. The viscoelasticity of our liver model is based on Prony series whose parameters have been experimentally estimated through a dynamic strain sweep testing. Furthermore, those parameters have been validated by reproducing *in silico* the experiments performed on liver samples. Finally, we take into account the porous medium of the liver parenchyma through a poroelastic model which computes the fluid pressure and the resulting applied pressure on the solid phase.

A.2 Modeling of the liver

The goal of this work is to construct a physically-realistic mechanical model of the liver that is suitable for the simulation of hepatic surgery. As such, the model should be as accurate as possible, but efficient enough to allow its application in real-time scenarios.

The first challenge is to characterize the mechanical behavior of the liver through rheology tests on liver tissue. For instance, Yamada (1970) has estimated the liver behavior in compression with an elastic modulus varying from 7.8 to 42kPa. Dependence of hepatic tissue elastic modulus with frequency was proposed in 2002 by Ottensmeyer (2002) and in 2005 by Valtorta and Mazza (2005), contributing in this way to consider liver tissue as viscoelastic. More recently, this dependence between liver mechanical modulus and frequency was reinforced thanks to the development of *in vivo* imaging-based elastography systems. A comparison between *in vivo* ultrasound-based transient elastography and *in vitro* rheometry has been proposed by Oudry et al. (2009). In Figure A.1, we show how our frequency dependent mechanical measurements of liver tissues compares with the literature. For large displacements, the non-linear behavior of the liver was first analyzed by Liu and Bilston (2002): liver tissue was considered as non linear beyond 0.2% strain. Kerdok (2006) in her thesis has proposed a global mechanical model of the liver based on ex-vivo perfused porcine livers.

Based on this literature survey of liver biomechanics, we propose to model hepatic tissue as hyperelastic and viscous. Moreover, porous properties which are due to the large amount of extracellular fluid in the liver, as explained in (Kerdok, 2006), are considered here. Figure A.2 shows schematically how these three components are related within a physically-based model. The porosity model acts in parallel to the visco-hyperelastic components and introduces the fluid pressure as an additional state variable. In the next sections, the individual components and underlying variables are described in details.

A.3 Visco-hyperelasticity based on Prony series

To model accurately the viscoelasticity of the liver, Rayleigh damping cannot be used. Instead, we propose to rely on Prony series (Taylor et al., 2009) which consists in adding to the hyperelastic stress tensor $\mathbf{S}_v$ some time dependent stresses. This time dependence is given

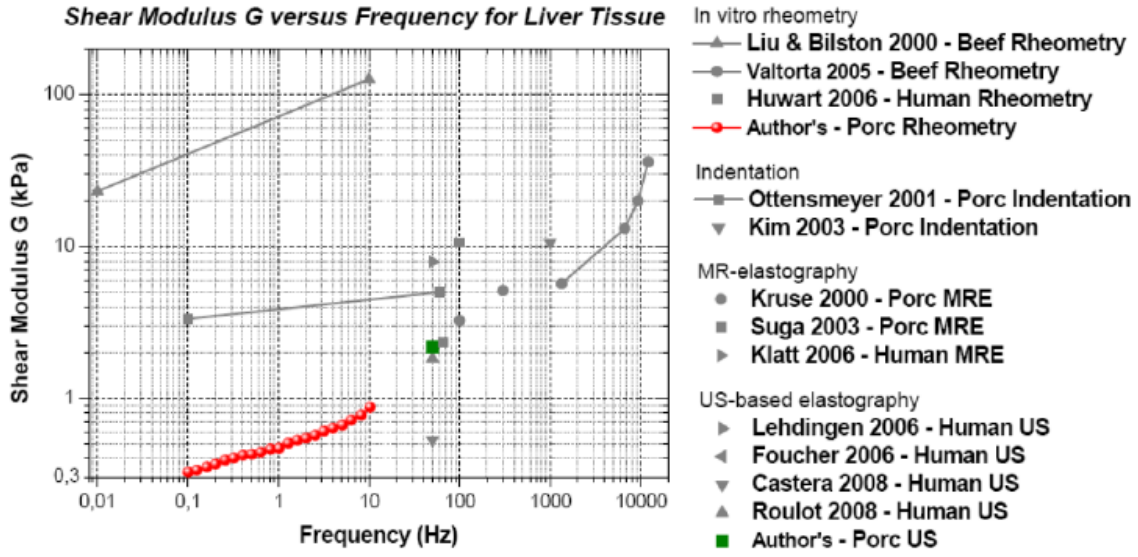

Figure A.1: Comparison between our Dynamic Mechanical Analysis results (bottom red curve) and values obtained in the literature.

by $\alpha(t) = \alpha_\infty + \sum_i \alpha_i e^{-t/\tau_i}$ with the condition $(\alpha_\infty + \sum_i \alpha_i) = 1$. The visco-hyperelastic SPK tensor $\mathbf{S}_v$ can be written as:

$$\begin{array}{c} \mathbf{S}_v = \int_0^t \alpha(t-t') \frac{\partial \mathbf{S}_h}{\partial t'} dt' = \mathbf{S}_h - \sum_i \gamma_i \\ \text{where} \quad \gamma_i = \int_0^t \alpha_i (1 - e^{(t'-t)/\tau_i}) \frac{\partial \mathbf{S}_h}{\partial t'} dt' \end{array} \tag{A.1}$$

After a discretization over time this results in the recursive formula:

$$\gamma_i^n = a_i \mathbf{S}_h^n + b_i \gamma_i^{n-1} \text{ where } a_i = \frac{\Delta t \alpha_i}{\Delta t + \tau_i} \text{ and } b_i = \frac{\tau_i}{\Delta t + \tau_i}$$

Δt is the time step used for discretization and has to be the same as the time step for any solvers during the simulation.
To combine the Prony series with our optimized hyperelastic formulation, we need to compute the total second Piola-Kirchoff stress tensor $\mathbf{S}_h^n$. This is done by computing the inverse deformation gradient :

$$\mathbf{S}_h = \nabla\phi^{-1} \left(\sum_{k=1}^{n} (f^{k\prime}(J) g^k(\tilde{I}) J \nabla\phi^{-T} + f^k(J) \nabla\phi \mathbf{S}_h^k) \right) \tag{A.2}$$

where $\nabla\phi^{-1} = \left(\sum_{l=1}^{4} P_l \otimes \frac{\partial J}{\partial Q_l} \right) / J$.

The visco-hyperelastic nodal forces are therefore related to the hyperelastic ones by $F_{v,i}^n = F_{h,i}^n + V_0 \nabla\phi \sum_i \gamma_i^n D_i$. Moreover, once we have γ_i^{n-1} the stiffness matrix is also slightly updated from its hyperelastic formulation $\mathbf{K}_{h,ij}^n$:

$$\mathbf{K}_{v,ij}^n = \mathbf{K}_{h,ij}^n \left(1 - \sum_k a_k \right) - V_0 D_j^T \left(\sum_k b_k \gamma_k^{n-1} \right) D_i \mathbf{Id}$$

Adding the viscous properties through the Prony series does not have a significant impact on the total computation times despite the evaluation of the time dependent stresses γ_i^n and $\nabla\phi^{-1}$.

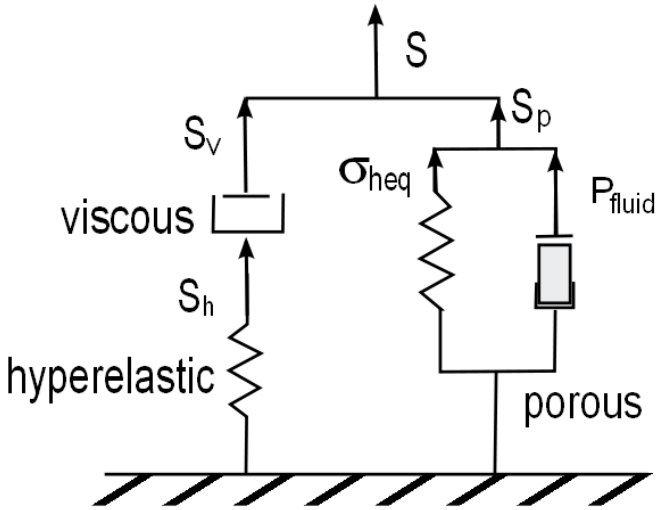

Figure A.2: Representation of the constitutive model combining viscosity, hyperelasticity and porosity.

A.4 Poro-elasticity

We propose to model the liver as a fluid-filled sponge following Kerdok's model (Kerdok, 2006). The proportion of free-fluid (blood, water...) in the liver parenchyma in the reference configuration is set to a constant f_w, $1-f_w$ represents the initial ratio of the solid phase (hepatic cells...). In such case, the volumetric part of the liver material (resistance to volume change) is governed by how much the volume change (measured by J) differs from $1-f_w$. Thus, we introduce the effective volumetric Jacobian $J^* = (f_w + J - 1)/f_w$, and define the volumetric Cauchy stress following Hencky's elasticity (Xiao and Chen, 2002):

$$\sigma_{Heq} = K_0 \, f_w \, ln(J^*)$$

where K_0 is the bulk modulus of the material. With this model, when J get close to $1-f_w$, the solid phase of the liver is completely compressed and the resulting stress is infinite. To avoid instabilities due to this infinite stress, we substitute σ_{Heq} when $J \leq J_0$ by its tangent curve at J_0 (see Figure A.3). We set $J_0 = 1 - f_w + K_0/K_{lim}$ where K_{lim} is a bulk modulus and represents the slope of the tangent.

The fluid phase of the liver also applies some volumetric stresses due to the transient response of the fluid through the porous liver parenchyma. A straightforward way of modeling the porous behavior is through the linear Darcy's law. In this setting, variation of fluid pressure P_{fluid} is governed by the variation of volume change and a diffusive process:

$$\frac{1}{K_{lim}} \dot{P}_{fluid} = \kappa \nabla^2 P_{fluid} - \frac{\dot{J}}{J} \tag{A.3}$$

where κ is the permeability parameter. In Kerdok's model, the permeability κ is a function of J, but we propose to keep it constant to decrease its computational cost.

Finally, the total Cauchy stress response in the volumetric part is defined by summing the solid and the fluid terms: $\sigma_p = \sigma_{heq}\mathbf{Id} - P_{fluid}\mathbf{Id}$.

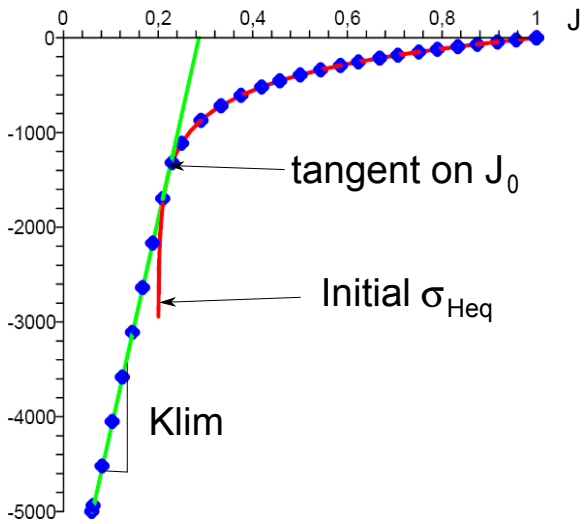

Figure A.3: Representation of the static Cauchy stress before and after substitution. (Red) Initial stress, (Green) Tangent curve, (Blue dots) New stress. Here $f_w = 0.8$.

The Cauchy stress is translated as a poro-elastic force and then added to the visco-hyperelastic forces:

$$F_{p,i} = -\sigma_p \left(\frac{\partial J}{\partial Q_i} \right)^T V_0$$

The additional stiffness matrices due to the porous behavior are given as:

$$\mathbf{K}_{p,ij} = V_0 \left(\frac{\partial \sigma_p}{\partial J} \left(\frac{\partial J}{\partial Q_j} \right)^T \left(\frac{\partial J}{\partial Q_i} \right) + \sigma_p \frac{\partial^2 J}{\partial Q_j \partial Q_i} \right)$$

The regularization strategy of the volumetric term described in section 3.3.1 iii) is applied to the stiffness matrix $\mathbf{K}_{p,ij}$.

The poro-elastic equation A.3 is integrated with an Euler semi-implicit method at the same frequency and with the same time step as the mechanical equation. The diffusive part of Darcy's law is discretized implicitly as a constant stiffness matrix and at each time step a linear system of equation involving nodal fluid pressures is solved with a conjugated gradient method with a maximum number of iterations (to limit computational cost). Note however that the term $\dot{J}/J$ discretized explicitely may undergo large variation and thus limits the maximal value of the global time step.

A.5 Small deformation dynamical testing on porcine liver: experimental materials and methods

To calibrate the visco-elastic parameters of our liver model, tests were performed on porcine livers. Dynamic viscoelastic behavior of hepatic tissue was investigated using *in vitro* Dynamic Mechanical Analysis (DMA) in rotating shear. Tests were carried out on liver cylindrical shaped samples coming from five adult pigs (weighting between 25 and 35kg). Immediately after hepatectomy performed on anesthetized animals, entire livers were stored

in an insulated container at 6C surrounded by ice. Cylindrical hepatic samples of 20 mm diameter and 4 mm thick were cut and tested within 6 hours post-mortem time. To avoid mechanical difference due to samples localization, 4 samples were tested for each of right, middle and left liver lobe. Hepatic tissue is considered as isotropic. At least 60 samples were tested (5 animals x 3 lobes x 4 samples).

Dynamic Strain Sweep tests and Dynamic Frequency Sweep tests were performed on a dedicated stress-controlled AR2000 (TA-Instruments, New Castle, DE, USA) rheometer in a parallel-plate configuration represented in Figure A.4. A pre-compression of 5mN was applied and sand paper was fixed to the rheometer plates to insure grip with tested sample.

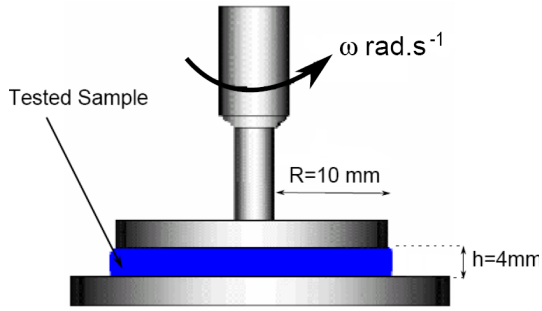

Figure A.4: Schematic representation of the testing device in a plate-plate configuration. Lower plate is fixed whereas upper is sinusoidally rotating

- Dynamic Strain Sweep

Those tests aim at giving linearity limit of the material elasticity. The sweep covers strain range from 0.01% to 20% which is sufficient according to the literature. Storage and loss shear moduli, noted respectively G' and G'' can be extracted from the experiments. In Figure A.5 the storage modulus is given for two samples and at two different temperatures. The linearity domain extends up to 1% to 2% of deformation.

- Dynamic Frequency Sweep

The upper plate rotates with a sinusoidal momentum and forces a sinusoidal deformation shifted with a phase δ. Such a device allows frequency sweep from 0.1 to 4Hz. Experiments were carried out in the linear viscoelastic strain range of the samples ($\gamma_0 = 0.1\%$). Storage and Loss shear moduli, as well as complex shear modulus G^* were calculated from the formulas:

$$G'(\omega) = cos\delta \ \frac{\sigma_0}{\gamma_0} \ , \ G''(\omega) = sin\delta \ \frac{\sigma_0}{\gamma_0} \tag{A.4}$$

and the complex modulus $G^*(\omega) = G'(\omega) + iG''(\omega)$ where σ_0 and γ_0 are the amplitude of the sinusoidally varying shear stress and strain respectively and δ the phase difference between stress and strain. We display the mean curves in Figure A.5, obtained from the 60 tested samples.

From these results the Dynamic Modulus G can be obtained as a function of the frequency or function of the time, and the viscoelastic behavior can be modeled after fitting a generalized Maxwell model with two modes of relaxation to those measurements:

$$G(t) = G_0(g_\infty + g_1 e^{-t/\tau_1} + g_2 e^{-t/\tau_2}) \tag{A.5}$$

where G_0 $g_\infty = G_\infty$ is called the equilibrium modulus, g_1, g_2, τ_1, τ_2 are parameters such as $g_\infty + g_1 + g_2 = 1$. The parameters are given in Table A.1. From Figure A.1, we can see

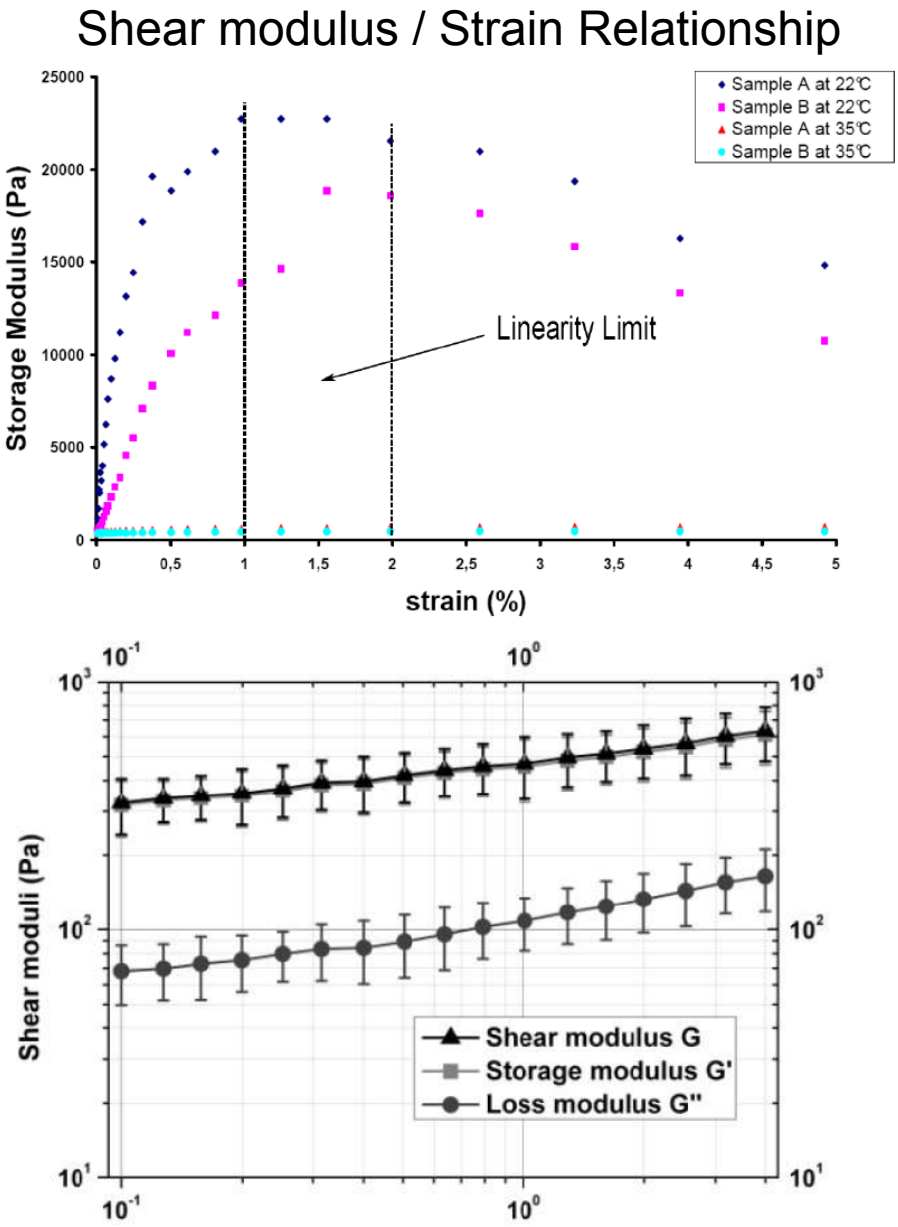

Figure A.5: Experimental Dynamic Mechanical Analysis results in terms of shear, storage and loss moduli for in vitro hepatic tissue samples. (Top) Strain Sweep tests, (Bottom) Frequency Sweep tests.

$G_0(Pa)$	$g_1(Pa)$	$\tau_1(s)$	$g_2(Pa)$	$\tau_2(s)$
770	0.235	0.27	0.333	0.03

Table A.1: Values of the parameters identified from the DMA Tests

that the estimated shear modulus is significantly lower that those measured by other authors on human or bovine livers at the same frequency range. However, when comparing with other measurements performed on porcine livers at higher frequencies with image-based elastography, they seem to be coherent.

A.6 Model Parameter fitting from experiments

From the rheological experiments described in the previous section, we derive the shear modulus G_0 required in the hyperelastic term (e.g. Boyce Arruda material) and the Prony series parameters required in the viscous term. To check that those parameters are indeed valid, we propose in this section to compare *in silico* simulations with the performed *in vitro* rheological tests. First, we check that the linearity domain for our hyperelastic materials matches the ones observed in the dynamic strain sweep experiments. We simulate a cylinder in extension in SOFA for several longitudinal stresses and estimate the associated strains. The stress/strain curves are shown in Figure **??** for two materials. It can be seen that the linearity limit corresponds to the one given by experiments ($1\% - 2\%$). Second,

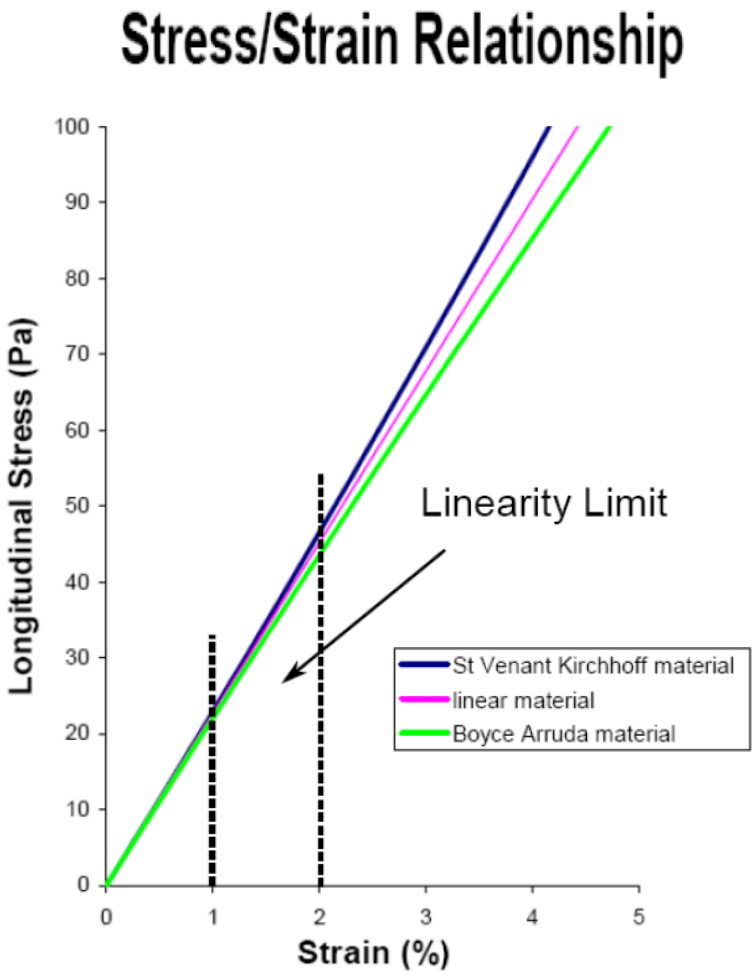

Figure A.6: Longitudinal stress/strain curves obtained with a cylinder for Boyce Arruda and St Venant Kirchhoff materials.

dynamic frequency sweep tests have been simulated using similar geometries and boundary conditions than the DMA tests (see FigureA.7). An oscillating torque (amplitude M) is applied on a small cylinder (radius $r = 10mm$, height $h = 4mm$) at various frequencies ω. The amplitude of the torque is chosen so as to stay in the linear domain. The angle of rotation θ of the cylinder is measured as a function of time. This angle describes a sinusoidal curve which follows the torque amplitude with a shifted phase δ. Specific constraint is applied on the top cylinder nodes to enforce a pure rotation of those nodes (as to reproduce the pure grip of sand paper).

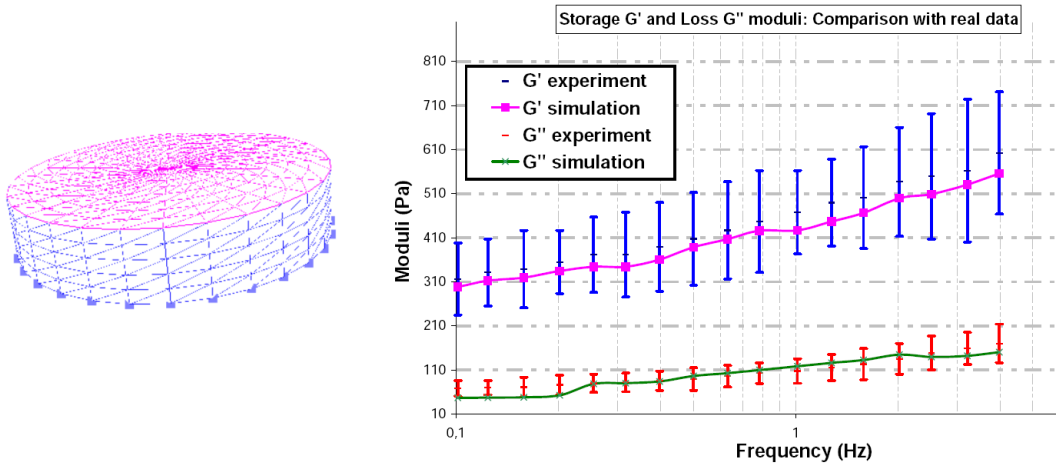

Figure A.7: (Left) Cylinder used for the simulation of shear deformation. (Pink) Rotating top nodes. (Blue triangles) Cylinder with parameters of the liver. (Blue dots) Fixed points.(Right) Comparison of the simulated values with the data obtained by DMA testing. The moduli are given on a x-log scale. The material is St Venant Kirchhoff, similar values are found for other materials.

Applying the classical formulas:

$$\sigma(t) = \frac{2M}{\pi r^3} \text{ and } \gamma(t) = \frac{r\theta(t)}{h}$$

and equations A.4 we can estimate the values of the Storage and Loss moduli to be compared with experimental data. It can be seen in Figure A.7 that the simulation manages to capture the viscous behavior of the liver for small deformations with a mean relative error of 5%. Given the fit errors and the standard deviation of the values obtained with the DMA tests, this mean error is reasonably good.

A.7 Poro-hyperelasticity simulation

We have implemented the porous component in our model using parameters based on Kerdok's (Kerdok, 2006) experimental data as shown in Table A.2.

In order to qualitatively check the accuracy of our implementation, we simulated a liver composed of two components: Boyce and Arruda hyperelasticity and porosity. The gravity is uniformly applied on the liver while several points of a plane are fixed (representing the ligament and veins). The simulated fluid pressure field during the deformation is shown in

fw	$K_0(Pa)$	$K_{lim}(kPa)$	$\kappa(m^4/Ns)$
0.5	400	2.2	20

Table A.2: Values of the parameters used for porosity component

Figure A.8 as a color map, ranging from dark blue (initial pressure) to red (highest pressure). Highest pressure in the fluid occurs when the liver is compressed either by the gravity

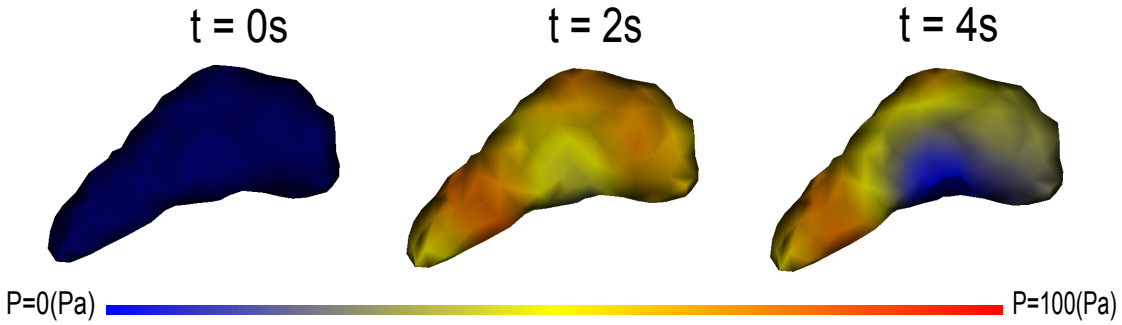

Figure A.8: Pressure field of the porous component on a liver under gravity

pressure (diffusion starts at the top) or by elastic reaction (diffusion starts at the bottom).

A.8 Complete Liver Model

To describe the influence of each component in the complete model, several simulations were performed using the same liver mesh (1240 vertices and 5000 tetrahedra), same parameters, under the same constant gravity force, and with Boyce Arruda material (Arruda and Boyce, 1993), at the fifth order. The liver mesh has been segmented from a CT scan image and meshed with the GHS3D software. An Euler implicit time integration scheme is used with a time step of 0.07s, the linear equations being solved with a conjugated gradient algorithm (number of iterations limited to 200). As boundary conditions, several nodes of the liver are fixed along the vena cava and suspensive ligament. The liver deforms under the action of gravity such as to overpass the linearity limit of the material. All computations were performed on a laptop PC with a Intel Core Duo processor at 2.80 GHz (simulations are available in the video clip).

(i) Influence of the viscous component
Adding viscosity to hyperelasticity increases the amplitude of the oscillations as the material becomes less stiff. Contrary to essentially hyperelastic model, the final state is really different from the initial state (see Figure A.9). Indeed, the use of Prony series leads to a multiplication of the SPK tensor by $1-\sum a_k$ at infinte time. Moreover, since the initial oscillations are larger, the stabilization takes more time (140s instead of 120s). The frame rate is around 9 FPS against 10 FPS for hyperelasticity alone. We did not reach the ideal 25FPS needed for real-time interaction. However the implicit integration scheme allows larger time step (0.3s for instance) which speeds up the simulation and makes user interactions efficient. High amount of extension and compression are possible which may be somewhat unrealistic, therefore the porous component is necessary to control the amount of viscosity.

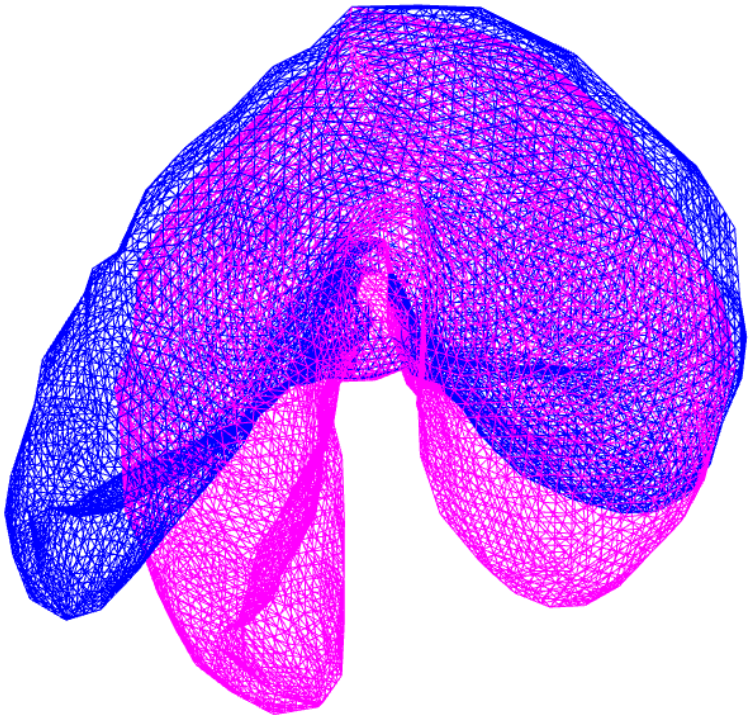

Figure A.9: Addition of viscosity to hyperelasticity: Comparison of the maximum amplitudes and final states. (Black) Initial position, (Blue) Hyperelastic liver, (Pink) Visco-hyperelastic liver.

(ii) Influence of the porous component
Adding porosity to visco-hyperelasticity prevents the liver from having unrealistic large deformations. The maximum amplitude is in between the hyperelasticity alone and the visco-hyperelasticity. The deformation is no longer isotropic and changes over time. The addition of this component decreases the computational efficiency (6 FPS) since a semi-implicit integration scheme is used for the porous component. Because of the fast variation of the explicit term $\dot{J}/J$, the time step has to be decreased to 0.15s. On our laptop PC, the simulation is still fluid enough to allow user interactions.

A.9 Discussion

We have proposed an innovative method to discretize hyperelastic materials on finite element meshes. The MJED method is fully general and requires from the user to provide a decomposition of the strain energy into simple terms. With this formulation, a number of precomputations can be performed to speed-up the assembly of stiffness matrices.

For the complete liver model, Boyce Arruda material was chosen based on Kerdok's observations (Kerdok, 2006) that the parenchyma is best represented by a 8-chain rubber like elastic model. But alternative materials such as Mooney Rivlin or Ogden could be also employed whereas Costa material is better suited for cardiac modeling. In the future, we are planning to perform additional strain sweep static tests in order to better characterize the hyperelastic behavior of the liver. One improvement of our model would be to add the influence of the Glisson capsule which acts as a membrane surrounding the liver parenchyma. However rheological experiments of that capsule are difficult to perform because it is really thin. Another avenue of research would be to couple the liver perfusion model with the simulation of blood flow inside the two liver veinous systems.

We have also shown in section A.6 that some parameters of the liver model can be identified based on dynamic mechanical testing. Model personalization is an important issue to create patient-specific simulations and we believe that ultrasound elastometry could be used for *in vivo* characterization of liver visco-elasticity.

For full user interaction, it is required to reach at least 25 FPS. For our visco-hyperelastic liver model, we were still able to have a reasonable interaction despite a frame rate of 10 by increasing the time step to 0.3s. Note that using implicit time integration schemes really helped getting a realistic behavior whereas using explicit schemes with much lower time steps and large frame rate lead to very damped motion. For instance, the same hyperelastic model implemented with an explicit Runge Kutta 4 solver could not stay stable after the first interaction even for a small time step (0.01s), and reaching only 11 FPS.

There are several ways to improve the computational efficiency (besides applying Moore's law). First, the porosity computation could be computed in parallel from the mechanical computation. Second, the assembly of stiffness matrices and the solution of linear systems of equations could be done on the GPU as already done by several authors (Taylor et al., 2009). Finally, the projection on reduced basis as shown in (Barbič and James, 2005) could decrease the size of the linear system to be solved at each time step.

Despite those advances, a lot of research needs to be done to achieve a realistic liver surgery simulation including the modeling of liver contact with neighboring structures, the influence of breathing and cardiac motion, the simulation of hepatic resection, bleeding and suturing.

Appendix B

MJED Method Calculation

To apply the MJED method described in Sec. 3.3, we need to go through complex matrix and tensor calculation.

B.1 MJED method

The strain energies $W_h^k = f^k(J)g^k(\tilde{I})$ are derived with respect to the points Q_i to obtain nodal forces, (described previously in equations 3.3) and the terms are summed up for each k. To get this first derivative, we use the same calculations as made by Delingette (2008).

$$\text{Combining } \nabla\phi = \sum_{i=1}^{4} Q_i D_i^T \text{ and } \mathbf{S}_h^k = 2\frac{\partial g^k(\tilde{I})}{\partial \mathbf{C}}$$

we obtain:

$$\frac{\partial g^k(\tilde{I})}{\partial Q_i} = D_i^T\ \mathbf{S}_h^k\ \nabla\phi^T \quad \text{and from} \quad \frac{\partial f^k(J)}{\partial Q_i} = f^{k'}(J)\ \frac{\partial J}{\partial Q_i} \tag{B.1}$$

where the derivative of the Jacobian is expressed as

$$\frac{\partial J}{\partial Q_i} = \frac{1}{6V_0}((Q_j - Q_l) \wedge (Q_k - Q_l))^T \tag{B.2}$$

we get nodal forces that only require the inputs $f^k, f^{k'}, g^k$ and $\mathbf{S}_h^k$:

$$F_{h,i} = -V_0 \sum_{k=1}^{n} \left(f^{k'}(J) g^k(\tilde{I}) \left(\frac{\partial J}{\partial Q_i} \right)^T + f^k(J) \nabla\phi\ \mathbf{S}_h^k\ D_i \right) \tag{B.3}$$

To obtain the stiffness matrix, we need to derive twice the strain energy, or to derive the transpose of the force. We start by deriving the first term of the force: $f^{k'}(J)\frac{\partial J}{\partial Q_i} g^k(\tilde{I})$. We obtain three terms:

$$\begin{cases} \mathbf{G}^k = \left(\frac{\partial f^{k'}(J)}{\partial Q_j}\right)^T \frac{\partial J}{\partial Q_i} g^k(\tilde{I}) \\ \mathbf{H}^k = f^{k'}(J) \frac{\partial^2 J}{\partial Q_j \partial Q_i} g^k(\tilde{I}) \\ \mathbf{I}^k = f^{k'}(J) \left(\frac{\partial g^k(\tilde{I})}{\partial Q_j}\right)^T \frac{\partial J}{\partial Q_i} \end{cases} \tag{B.4}$$

which are easily written using equation (B.1) and the second derivative of the Jacobian:

$$\frac{\partial^2 J}{\partial Q_j \partial Q_i} == \frac{1-\delta_{ij}}{6V_0} \begin{bmatrix} 0 & -c_3 & c_2 \\ c_3 & 0 & -c_1 \\ -c_2 & c_1 & 0 \end{bmatrix} \tag{B.5}$$

with δ_{ij} the Kronecker delta and $\mathbf{c} = (c_1, c_2, c_3)$ the edge vector opposing $\mathbf{Q}_i$ and $\mathbf{Q}_j$.
Let consider the second term of the force: $f^k(J) D_i^T \ \mathbf{S}_h^k \ \nabla\phi^T$. As D_i is constant, that also leads to three additional terms:

$$\begin{cases} \lambda^k = \left(\frac{\partial f^k(J)}{\partial Q_j}\right)^T D_i^T \ \mathbf{S}_h^k \ \nabla\phi^T \\ \mathbf{M}^k = f^k(J) \ D_i^T \ \mathbf{S}_h^k \ \left(\frac{\partial \nabla\phi^T}{\partial Q_j}\right)^T \\ \mathbf{R}^k = f^k(J) \left(\frac{\partial \mathbf{S}_h^k}{\partial Q_j} D_i\right)^T \nabla\phi^T \end{cases} \tag{B.6}$$

Computation of λ^k and $\mathbf{M}^k$ is straightforward using the definition of $\nabla\phi$ which gives $\frac{\partial \nabla\phi}{\partial Q_j} = \mathbf{Id} D_j^T$ and equation (B.1). $\mathbf{R}^k$ is more complex and in the remainder the $.^k$ notation is dropped to simplify notations and derive the expression component wise. We seek to determine a matrix whose elements are $\frac{\partial \mathbf{S}_{ab}}{\partial Q_j^v}$ where a, b and v are in $[1..3]$. Including the matrix $\mathbf{C}$ in the chain rule we express this term as:

$$\frac{\partial \mathbf{S}_{ab}}{\partial Q_j^v} = \sum_{m,n=1}^{3} \frac{\partial \mathbf{S}_{ab}}{\partial \mathbf{C}_{mn}} \frac{\partial \mathbf{C}_{mn}}{\partial Q_j^v}$$

But, using $\frac{\partial \mathbf{C}_{mn}}{\partial Q_j^v} = \sum_{u=1}^{4} [Q_u^v \ D_j^m \ D_u^n + Q_u^v \ D_u^m \ D_j^n]$ and $\nabla\phi_{mn} = \sum_{u=1}^{4} Q_u^m \ D_u^n$ and noticing moreover that $\mathbf{D}_j^m \ \nabla\phi_{vn} = \left[D_j \otimes (\nabla\phi^T e_v)\right]_{mn}$. We can finally compute the expressions to obtain the derivative with respect to $\mathbf{Q}_j^v$:

$$\frac{\partial \mathbf{S}}{\partial Q_j^v} = \frac{\partial \mathbf{S}}{\partial \mathbf{C}} : \left[D_j \otimes (\nabla\phi^T e_v) + (\nabla\phi^T e_v) \otimes D_j\right]$$

where $\frac{\partial \mathbf{S}}{\partial \mathbf{C}}$ is a fourth order tensor, applied to the matrix $\left[D_j \otimes (\nabla\phi^T e_v) + (\nabla\phi^T e_v) \otimes D_j\right]$ which is a second order tensor (a matrix). Finally the derivative we seek is :

$$\frac{\partial \mathbf{S}}{\partial Q_j} D_i = \sum_{v=1}^{3} \frac{\partial \mathbf{S}}{\partial Q_j^v} D_i \otimes e_v$$

Furthermore, we take advantage of the specific structure of the fourth order elasticity tensors. In all cases, this tensor can be written as a sum of two kinds of terms,

$$\beta_1^k \ \mathbf{A}_1^k \ \mathbf{H} \ \mathbf{A}_1^k \text{ or } \beta_2^k \ (\mathbf{H} : \mathbf{A}_2^k) \ \mathbf{A}_2^k$$

where β_u^k are scalars, $\mathbf{A}_u^k$ are symmetric matrices, and $\mathbf{A} : \mathbf{B} = tr(\mathbf{B}^T \mathbf{A})$ for any two matrices $\mathbf{A}, \mathbf{B}$. Each one of those two kinds of terms leads to simpler expressions of $\mathbf{R}^k$, respectively:

$$f^k(J) \ \nabla\phi \ \mathbf{L}_1^k(i,j) \ \nabla\phi^T \text{ and } f^k(J) \ \nabla\phi \ \mathbf{L}_2^k(i,j) \ \nabla\phi^T \tag{B.7}$$

where $\mathbf{L}_1^k(i,j)$ and $\mathbf{L}_2^k(i,j)$ are the linear matrices

$$\begin{cases} \mathbf{L}_1^k(i,j) = \beta_1^k \left(\mathbf{A}_1^k \ D_i \otimes D_j \ \mathbf{A}_1^k + \mathbf{A}_1^k (D_j \cdot \mathbf{A}_1^k \ D_i)\right) \\ \mathbf{L}_2^k(i,j) = 2\beta_2^k \left(\mathbf{A}_2^k \ D_j \otimes D_i \ \mathbf{A}_2^k\right) \end{cases} \tag{B.8}$$

which are constant in most cases.

To conclude, the stiffness matrix is:

$$\mathbf{K}_{h,ij} = \frac{\partial^2 W(T_P)}{\partial Q_i \partial Q_j} = V_0 \sum_k (\mathbf{G}^k + \mathbf{H}^k + \mathbf{I}^k + \lambda^k + \mathbf{M}^k + \mathbf{R}^k) \tag{B.9}$$

B.2 Combining MJED and Prony series

It consists in adding to the hyperelastic stress tensor $\mathbf{S}_v$ some time dependent stresses:

$$\alpha(t) = \alpha_\infty + \sum_i \alpha_i e^{-t/\tau_i} \text{ with } \left(\alpha_\infty + \sum_i \alpha_i\right) = 1$$

At time n the visco-hyperelastic SPK tensor $\mathbf{S}_v^n$ can be written as:

$$\mathbf{S}_v^n = \mathbf{S}_h^n - \sum_i \gamma_i^n$$

$$\gamma_i^n = a_i \mathbf{S}_h^n + b_i \gamma_i^{n-1} \text{ where } a_i = \frac{\Delta t\ \alpha_i}{\Delta t + \tau_i} \text{ and } b_i = \frac{\tau_i}{\Delta t + \tau_i}$$

Δt is the time step used for discretization and has to be the same as the time step for any solvers during the simulation. Therefore, we need to compute the total second Piola-Kirchoff stress tensor $\mathbf{S}_h^n$. This is done by computing the inverse deformation gradient :

$$\mathbf{S}_h^n = \nabla\phi^{-1}\left(\sum_k (f^{k'}(J) g^k(\tilde{I}) J \nabla\phi^{-T} + f^k(J)\nabla\phi \mathbf{S}_h^k)\right)$$

where $\nabla\phi^{-1} = \left(\sum_{l=1}^4 P_l \otimes \frac{\partial J}{\partial Q_l}\right)/J$.
The visco-hyperelastic nodal forces are therefore related to the hyperelastic ones by

$$F_{v,i}^n = F_{h,i}^n + V_0 \nabla\phi \sum_i \gamma_i^n D_i$$

Moreover, once we have γ_i^{n-1} the stiffness matrix is also slightly updated from its hyperelastic formulation:

$$\mathbf{K}_{v,ij}^n = \mathbf{K}_{h,ij}^n \left(1 - \sum_k a_k\right) - V_0 D_j^T \left(\sum_k b_k \gamma_k^{n-1}\right) D_i \mathbf{Id}$$

B.3 pseudo-code of the MJED method

To compute the FEM formulation, three functions are necessary to input into the solvers: an initialization , the computation of the force vector and finally the computation of the stiffness matrix. We start with the init() function (Algorithm 2) which loads the mesh, initializes the variables and precomputes some quantities. This function is only called once, before the simulation starts. Then we build the Force Vector (Algorithm 3) for every tetrahedron, and at each time step. And finally we compute the stiffness matrices (Algorithm 4 for every tetrahedron, at each time step (depending on the solver used).

B.4 MJED method on Costa's law

The MJED method can also be applied to laws where the strain energy does not depend on invariants but are function on the Green tensor $\mathbf{E}$. We describe here its derivation for Costa's orthotropic law. The strain energy for this material is given as:

$$\begin{aligned} W &= \frac{1}{2} a \left(e^{\bar{A}} - 1\right) + \frac{\kappa}{2}(J-1)^2 \\ \bar{A} &= J^{-4/3}(b_{ff}E_{ff}^2 + 2b_{fs}E_{fs}^2 + b_{ss}E_{ss}^2 + 2b_{fn}E_{fn}^2 + 2b_{sn}E_{sn}^2 + b_{nn}E_{nn}^2) \end{aligned} \tag{B.10}$$

Algorithm 2 init() function

Load the mesh and get the topology (tetrahedra, vertices, edges ...)
for every tetrahedron i **do**
    Get the reference points position in the tetrahedron, P_j
    Calculate the reference volume V_0
    Calculate the Shape Vectors D_j
    for every edge with vertices u and v **do**
        Compute the linear matrices $\mathbf{L}_k(u,v)$ (see equation B.8)
    end for
end for

Algorithm 3 addForce() function

for every tetrahedron i **do**
    Get the current points position in the tetrahedron, Q_j
    Compute the Deformation Gradient $\nabla\Phi$
    Compute the Cauchy-Green Tensor $\mathbf{C}$
    Compute the Jacobian J
    for every vertex j **do**
        Compute the first derivative of the Jacobian $\frac{\partial J}{\partial Q_j}$ (see equation B.2)
    end for
    for every k of the decomposition **do**
        Get f_k, f'_k, f''_k, g_k, and $\mathbf{S}_k$
    end for
    for every vertex j **do**
        Compute the Force F_j summing the contributions from the decomposition (see equation B.3)
    end for
end for

Algorithm 4 addDForce() function

for every tetrahedron i **do**
    for every edge with vertices u and v **do**
        Compute the second derivative of the Jacobian $\frac{\partial^2 J}{\partial Q_u \partial Q_v}$ (see equation B.5)
        for every k of the decomposition **do**
            Calculate $\mathbf{G}_k$, $\mathbf{H}_k$, $\mathbf{I}_k$, λ_k, $\mathbf{M}_k$ and $\mathbf{R}_k$ using $\mathbf{L}_k(u,v)$ (equations B.4, B.6 and B.7)
        end for
        Compute the Stiffness Matrix $\mathbf{K}_{uv}$ (see equation B.9)
    end for
end for

where b_{kl} are orthotropic coefficients with (f,s,n) respectively the fibers, sheets and normal-sheets directions; a, κ are material parameters and J is the Jacobian (ratio between deformed volume and rest volume). To optimize the implementation using the MJED method we decompose the strain energy as

$$W = \frac{a}{2} e^{f_1 g_1} + f_2 g_2$$

where

$$\begin{array}{lcl} f_1 & = & J^{-4/3} \\ g_1 & = & \mathbf{E}_{fsn} : (\mathbf{G}_{fsn} : \mathbf{E}_{fsn}) \\ f_2 & = & \frac{\kappa}{2}(J-1)^2 - \frac{a}{2} \\ g_2 & = & 1 \end{array} \tag{B.11}$$

with $\mathbf{A} : \mathbf{B} = tr(\mathbf{A}^T \mathbf{B})$ for two matrices $\mathbf{A}$ and $\mathbf{B}$, and $\mathbf{G}_{fsn}$ is the symmetric 4th order tensor in the local base (f,s,n) defined as the 6×6 matrix:

$$\mathbf{G}_{fsn} = \begin{pmatrix} b_{ff} & 0 & \dots & \dots & \dots & 0 \\ 0 & b_{fs} & \ddots & & & \vdots \\ \vdots & \ddots & b_{ss} & \ddots & & \vdots \\ \vdots & & \ddots & b_{fn} & \ddots & \vdots \\ \vdots & & & \ddots & b_{ns} & 0 \\ 0 & \dots & \dots & \dots & 0 & b_{nn} \end{pmatrix}$$

(f,s,n) can be found as the eigenvectors of the DT MRI tensor from images. The change from the local base (f,s,n) into the global base (x,y,z) is performed thanks to:

$$\begin{aligned} \mathbf{G} = & b_{ff}(f \otimes f) \otimes (f \otimes f) + b_{fs}(f \otimes s + s \otimes f) \otimes (f \otimes s + s \otimes f) \\ & + b_{ss}(s \otimes s) \otimes (s \otimes s) + b_{fn}(f \otimes n + n \otimes f) \otimes (f \otimes n + n \otimes f) \\ & + b_{sn}(s \otimes n + n \otimes s) \otimes (s \otimes n + n \otimes s) + b_{nn}(n \otimes n) \otimes (n \otimes n) \end{aligned} \tag{B.12}$$

where $u \otimes u$ is the symmetric matrix $\mathbf{A} = uu^t$ when u is a 3×1 vector, which can be expressed as a 6×1 vector. Therefore the tensor $\mathbf{A} \otimes \mathbf{A}$ can be calculated using the vector formulation and gives a symmetric 6×6 matrix. Hence the function g_1 is also equivalent to $\mathbf{E} : (\mathbf{G} : \mathbf{E})$.

Finally, the derivatives necessary to apply the MJED method are easily defined as:

$$\begin{array}{ll} f_1' = -\frac{4}{3} J^{-7/3} & f_1'' = \frac{28}{9} J^{-10/3} \\ \mathbf{S}_1 = \frac{\partial g_1}{\partial \mathbf{E}} = 2\mathbf{G} : \mathbf{E} & \frac{\partial \mathbf{S}_1}{\partial \mathbf{E}} : \mathbf{H} = 2\mathbf{G} : \mathbf{H} \\ f_2' = \kappa(J-1) & f_2'' = \kappa \\ \mathbf{S}_2 = \mathbf{0} & \frac{\partial \mathbf{S}_2}{\partial \mathbf{E}} : \mathbf{H} = \mathbf{0} \end{array} \tag{B.13}$$

Appendix C

Valve Model Calculation

C.1 Relation between nodal displacements and ventricular volumes

We compute the volume of the ventricle (open surface mesh Z) as a sum of the tetrahedra that are formed by each triangle on the surface and a unique point, for instance the point $\mathbf{O}$. Let $\mathbf{Q}_k$ be the deformed points on the surface with each unit volume of tetrahedron T_i given by $V_i = \frac{1}{6}|\mathbf{Q}_{T_i(0)}, \mathbf{Q}_{T_i(1)}, \mathbf{Q}_{T_i(2)}|$, where $|.,.,.|$ is the mix product. If the surface is closed, the total volume is the sum of the unit volumes over all the triangles.

For an open surface mesh, with N holes, we virtually close each of the holes n by a point $\mathbf{C}_n$ - the barycenter of the N_n points on the border named $\mathbf{Q}_{H_n(k)}$:

$$\mathbf{C}_n = \frac{1}{N_n} \sum_{k=0}^{N_n-1} \mathbf{Q}_{H_n(k)}$$

Therefore the total volume of the ventricle can be written as:

$$V_{total} = \sum_{T_i \varepsilon Z} V_i + \sum_n \sum_{k=0}^{N_n-1} \frac{1}{6} |\mathbf{Q}_{H_n(k)}, \mathbf{Q}_{H_n(k+1)}, \mathbf{C}_n| \tag{C.1}$$

C.2 Derivatives of the volume

We obtain the vector $\mathbf{G}_L$ (respectively $\mathbf{G}_R$), by differentiating the volume with respect to the nodal positions on the surface.

- *Inside Points*:

Let's define the area vector of a triangle T_i:

$$\mathbf{A}(T_i) = \frac{\mathbf{Q}_{T_i(0)} \times \mathbf{Q}_{T_i(1)} + \mathbf{Q}_{T_i(1)} \times \mathbf{Q}_{T_i(2)} + \mathbf{Q}_{T_i(2)} \times \mathbf{Q}_{T_i(0)}}{2}$$

then we need to sum over all the triangles that surround the point $\mathbf{Q}_i$.

$$\frac{\partial V}{\partial \mathbf{Q}_i} = \frac{1}{3} \sum_{T_j \supset \mathbf{Q}_i} \mathbf{A}(T_j)$$

- *Border Points*:

To this derivative, the contribution of $\frac{1}{6}|\mathbf{Q}_{H_j(k)}, \mathbf{Q}_{H_j(k+1)}, \mathbf{C}_j|$ has to be added. It gives therefore

$$\begin{aligned}\frac{\partial V}{\partial \mathbf{Q}_{H_n(i)}} =& \frac{1}{3} \sum_{T_j \supset \mathbf{Q}_{H_n(i)}} \mathbf{A}(T_j) \\ &+ \frac{\mathbf{Q}_{H_n(i)} \times \mathbf{Q}_{H_n(i+1)}}{6} + \frac{\mathbf{Q}_{H_n(i+1)} \times \mathbf{C}_n}{6} \\ &+ \frac{\mathbf{C}_n \times \mathbf{Q}_{H_n(i-1)}}{6} + \frac{\mathbf{Q}_{H_n(i-1)} \times \mathbf{Q}_{H_n(i)}}{6}\end{aligned} \tag{C.2}$$

- *Second Derivative for inside points*:

We want to differentiate $\frac{\partial V}{\partial \mathbf{Q}_i}$ with respect to $\partial \mathbf{Q}_k$. When we sum the area vectors over all the triangles that surround ∂Q_i, many terms are cancelled, and many do not include ∂Q_k. For the derivative, only two terms remain:

$$\frac{\partial^2 V}{\partial \mathbf{Q}_k \partial \mathbf{Q}_i} = \frac{1}{6} \frac{\partial}{\partial \mathbf{Q}_k} (\mathbf{Q}_k \times \mathbf{Q}_v + \mathbf{Q}_u \times \mathbf{Q}_k)$$

where $(\mathbf{Q}_k, \mathbf{Q}_v, \mathbf{Q}_i)$ and $(\mathbf{Q}_u, \mathbf{Q}_k, \mathbf{Q}_i)$ are two oriented triangles. The second derivative is then:

$$\frac{\partial^2 V}{\partial \mathbf{Q}_k \partial \mathbf{Q}_i} = \frac{1}{6} \begin{pmatrix} 0 & -b_3 & b_2 \\ b_2 & 0 & -b_1 \\ -b_2 & b_1 & 0 \end{pmatrix} \tag{C.3}$$

where $\mathbf{b} = (b_1, b_2, b_3) = \mathbf{Q}_u - \mathbf{Q}_v$.

- *Second Derivative for border points*:

When $\mathbf{Q}_i$ and $\mathbf{Q}_k$ are on the border, for instance $\mathbf{Q}_i = \mathbf{Q}_{H_n(i)}$ and $\mathbf{Q}_k = \mathbf{Q}_{H_n(i+1)}$, we have to add a vector $\tilde{\mathbf{b}} = \mathbf{Q}_{H_n(i)} - \mathbf{C}_n$ to $\mathbf{b}$.

Bibliography

Aliev, R. and Panfilov, A. (1996). A simple two-variable model of cardiac excitation. *Chaos, Solitons & Fractals*, 7(3):293–301.

Arruda, E. and Boyce, M. (1993). A three-dimensional constitutive model for the large stretch behavior of rubber elastic materials. *J. Mech. Phys. Solids*, 41(2):389–412.

Arts, T., Delhaas, T., Bovendeerd, P., Verbeek, X., and Prinzen, F. (2005). Adaptation to mechanical load determines shape and properties of heart and circulation: the circadapt model. *American Journal of Physiology-Heart and Circulatory Physiology*, 288(4):H1943–H1954.

Arts, T., Reneman, R., and Veenstra, P. (1979). A model of the mechanics of the left ventricle. *Annals of biomedical engineering*, 7(3):299–318.

Attene, M. and Falcidieno, B. (2006). ReMESH: An interactive environment to edit and repair triangle meshes. In *Shape Modeling and Applications, IEEE International Conference on*, page 41.

Barbič, J. and James, D. L. (2005). Real-time subspace integration for St. Venant-Kirchhoff deformable models. *ACM TOG (SIGGRAPH 2005)*, 24(3):982–990.

Baxley, W. and Joseph Reeves, T. (1971). Abnormal regional myocardial performance in coronary artery disease. *Progress in cardiovascular diseases*, 13(5):405–421.

Bestel, J., Clement, F., and Sorine, M. (2001). A biomechanical model of muscle contraction. *Medical Image Computing and Computer Assisted Intervention (MICCAI)*, pages 1159–1161.

Billet, F. (2010). *Assimilation de données images pour la personnalisation d'un modèle électromécanique du coeur*. PhD thesis, Université de Nice -Sophia Antipolis. In French.

Bortone, A. S., Hess, O. M., Chiddo, A., Gaglione, A., Locuratolo, N., Caruso, G., and Rizzon, P. (1989). Functional and structural abnormalities in patients with dilated cardiomyopathy. *J Am Coll Cardiol*, 14:613–623.

Chabiniok, R., Moireau, P., Lesault, P., Rahmouni, A., Deux, J., and Chapelle, D. (2011). Estimation of tissue contractility from cardiac cine-MRI using a biomechanical heart model. *Biomechanics and Modeling in Mechanobiology*, pages 1–22.

Chapelle, D., Fragu, M., Mallet, V., and Moireau, P. (2012a). Fundamental principles of data assimilation underlying the verdandi librairy: applications to biophysical model personalization with euheart. *Medical & Biological Engineering & Computing (MBEC)*.

Chapelle, D., Le Tallec, P., Moireau, P., and Sorine, M. (2012b). An energy-preserving muscle tissue model: formulation and compatible discretizations. *International Journal for Multiscale Computational Engineering*, 10(2):189–211.

Chinchapatnam, P., Rhode, K., Ginks, M., Rinaldi, C., Lambiase, P., Razavi, R., Arridge, S., and Sermesant, M. (2008). Model-based imaging of cardiac apparent conductivity and local conduction velocity for diagnosis and planning of therapy. *Medical Imaging, IEEE Transactions on*, 27(11):1631–1642.

Colli Franzone, P., Guerri, L., and Rovida, S. (1990). Wavefront propagation in an activation model of the anisotropic cardiac tissue: asymptotic analysis and numerical simulations. *Journal of mathematical biology*, 28(2):121–176.

Costa, K. D., Holmes, J., and McCulloch, A. D. (2001). Modelling cardiac mechanical properties in three dimensions. *Phil. Trans. R. Soc. Lond.*, 359:1233–1250.

Cotin, S., Delingette, H., and Ayache, N. (2000). A hybrid elastic model allowing real-time cutting, deformations and force-feedback for surgery training and simulation. *The Visual Computer*, 16(8):437–452.

Courtecuisse, H., Allard, J., Duriez, C., and Cotin, S. (2010). Asynchronous preconditioners for efficient solving of non-linear deformations. *VRIPHYS*, pages 59–68.

Craene, M. D., Allain, P., Gao, H., Prakosa, A., Marchesseau, S., Hilpert, L., Somphone, O., Delingette, H., Makram-Ebeid, S., Villain, N., D'hooge, J., Sermesant, M., and Saloux, E. (2012). Synthetic and Phantom Setups for the Second cardiac Motion Analysis Challenge (cMAC2). In *Proc. MICCAI Workshop on Statistical Atlases and Computational Models of the Heart: Imaging and Modelling Challenge (STACOM12)*, LNCS. Springer.

De Craene, M., Piella, G., Camara, O., Duchateau, N., Silva, E., Doltra, A., D'hooge, J., Brugada, J., Sitges, M., and Frangi, A. F. (2012a). Temporal diffeomorphic free-form deformation: Application to motion and strain estimation from 3D echocardiography. *Med Image Anal*, 16(2):427–450.

De Craene, M., Tobon-Gomez, C., Butakoff, C., Duchateau, N., Piella, G., Rhode, K. S., and Frangi, A. F. (2012b). Temporal diffeomorphic free form deformation (TDFFD) applied to motion and deformation quantification of tagged MRI sequences. In Camara, O., Konukoglu, E., Pop, M., Rhode, K., Sermesant, M., and Young, A., editors, *Statistical Atlases and Computational Models of the Heart. Imaging and Modelling Challenges*, volume 7085 of *Lecture Notes in Computer Science*, pages 68–77. Springer Berlin / Heidelberg.

Delingette, H. (2008). Triangular Springs for Modeling Nonlinear Membranes. *IEEE J VCG*, 14(2):329–341.

Delingette, H. and Ayache, N. (2004). Soft tissue modeling for surgery simulation. In *Computational Models for the Human Body*, pages 453–550. Elsevier.

Delingette, H., Billet, F., Wong, K., Sermesant, M., Rhode, K., Ginks, M., Rinaldi, C., Razavi, R., and Ayache, N. (2012). Personalization of cardiac motion and contractility from images using variational data assimilation. *Biomedical Engineering, IEEE Transactions on*, 59(1):20–24.

Ecabert, O., Peters, J., Walker, M. J., Ivanc, T., Lorenz, C., von Berg, J., jonathan Lessick, mani Vembar, and Weese, J. (2011). Segmentation of the heart and great vessels in CT images using a model-based adaptation framework. *Medical Image Analysis*, 15(6):863–876.

Endo, M. (1977). Calcium release from the sarcoplasmic reticulum. *Physiological Reviews*, 57(1):71–108.

Faure, F., Duriez, C., Delingette, H., Allard, J., Gilles, B., Marchesseau, S., Talbot, H., Courtecuisse, H., Bousquet, G., Peterlik, I., et al. (2012). SOFA: A Multi-Model Framework for Interactive Physical Simulation. *Soft Tissue Biomechanical Modeling for Computer Assisted Surgery*, pages 283–321.

FitzHugh, R. (1961). Impulses and physiological states in theoretical models of nerve membrane. *Biophysical Journal*, 1:445–466.

Ginks, M. R., Lambiase, P. D., Duckett, S. G., Bostock, J., Chinchapatnam, P., Rhode, K., McPhail, M. J., Simon, M., Bucknall, C., Carr-White, G., Razavi, R., and Rinaldi, C. A. (2011). A simultaneous X-Ray/MRI and noncontact mapping study of the acute hemodynamic effect of left ventricular endocardial and epicardial cardiac resynchronization therapy in humans. *Circulation Heart Failure*, 4(2):170–179.

Hawkes, D., Barratt, D., Blackall, J., Chan, C., Edwards, P., Rhode, K., Penney, G., McClelland, J., and Hill, D. (2005). Tissue deformation and shape models in image-guided interventions: a discussion paper. *Medical Image Analysis*, 9(2):163 – 175.

Hodgkin, A. and Huxley, A. (1952). A quantitative description of membrane current and its application to conduction and excitation in nerve. *Journal of Physiology*, 177:500–544.

Holzapfel, G., Gasser, T., and Ogden, R. (2000). A new constitutive framework for arterial wall mechanics and a comparative study of material models. *Journal of elasticity*, 61(1):1–48.

Holzapfel, G. and Ogden, R. (2009). Constitutive modelling of passive myocardium: a structurally based framework for material characterization. *Philosophical Transactions of the Royal Society A: Mathematical, Physical and Engineering Sciences*, 367(1902):3445–3475.

Humphrey, J., Strumpf, R., and Yin, F. (1990). Determination of a constitutive relation for passive myocardium: I. a new functional form. *Journal of biomechanical engineering*, 112:333.

Hunter, P., Nash, M., and Sands, G. (1997). Computational electromechanics of the heart. *Computational biology of the heart*, pages 345–407.

Huxley, A. (1957). Muscle structure and theories of contraction. *Progress in biophysics and biophysical chemistry*, 7:255.

Imperiale, A., Chabiniok, R., Moireau, P., and Chapelle, D. (2011). Constitutive parameter estimation using tagged-mri data. In *Proceedings of FIMH'11, LNCS 6666*, pages 409–417. Springer.

James, D. L. and Pai, D. K. (1999). ArtDefo accurate real time deformable objects. In *Computer Graphics (SIGGRAPH)*, pages 65–72.

Joldes, G., Wittekemail, A., and Miller, K. (2009). Suite of finite element algorithms for accurate computation of soft tissue deformation for surgical simulation. *Medical Image Analysis*, 13(6):912 – 919.

Julier, S. and Uhlmann, J. (1997). A new extension of the Kalman filter to nonlinear systems. In *Int. Symp. Aerospace/Defense Sensing, Simul. and Controls*, volume 3, page 26. Citeseer.

Keener, J. and Sneyd, J. (2009). *Mathematical physiology: Cellular physiology*, volume 1. Springer Verlag.

Kerckhoffs, R. C. P., editor (2010). *Patient-Specific Modeling of the Cardiovascular System, Technology-Driven Personalized Medicine*. Springer.

Kerdok, A. E. (2006). *Characterizing the Nonlinear Mechanical Response of Liver to Surgical Manipulation*. PhD thesis, Harvard University.

Klabunde, R. (2011). *Cardiovascular physiology concepts*. Lippincott Williams & Wilkins.

Koon, K., Thebault, C., Le Rolle, V., Donal, E., and Hernández, A. (2010). Atrioventricular delay optimization in cardiac resynchronization therapy assessed by a computer model. In *Computing in Cardiology, 2010*, pages 333 –336.

Krejci, P., Sainte-Marie, J., Sorine, M., and Urquiza, J.-M. (2006). Solutions to muscle fiber equations and their long time behaviour. *Nonlinear Analysis: Real World Applications*, 7(4):535–558.

Larrabide, I., Omedas, P., Martelli, Y., Planes, X., Nieber, M., Moya, J., Butakoff, C., Sebastián, R., Camara, O., De Craene, M., et al. (2009). Gimias: an open source framework for efficient development of research tools and clinical prototypes. *Functional Imaging and Modeling of the Heart*, pages 417–426.

Lepiller, D., Sermesant, M., Pop, M., Delingette, H., Wright, G., and Ayache, N. (2008). Cardiac electrophysiology model adjustment using the fusion of mr and optical imaging. *Medical Image Computing and Computer-Assisted Intervention–MICCAI 2008*, pages 678–685.

Liu, H. and Shi, P. (2009). Maximum a posteriori strategy for the simultaneous motion and material property estimation of the heart. *Biomedical Engineering, IEEE Transactions on*, 56(2):378–389.

Liu, Z. and Bilston, L. (2002). Large deformations shear properties of liver tissue. *Biorheology*, 39(6):735–742.

Lombaert, H., Peyrat, J.-M., Croisille, P., Rapacchi, S., Fanton, L., Clarysse, P., Delingette, H., and Ayache, N. (2011). Statistical Analysis of the Human Cardiac Fiber Architecture from DT-MRI. In Axel, L. and Metaxas, D., editors, *Proceedings of FIMH Conference 2011*, volume 6666 of *LNCS*, pages 171–179. Springer. Best Paper Award.

Lorensen, W. E. and Cline, H. E. (1987). Marching cubes: A high resolution 3d surface construction algorithm. *Computer Graphics*, 21(4):163–169.

Mansi, T., André, B., Lynch, M., Sermesant, M., Delingette, H., Boudjemline, Y., and Ayache, N. (2009). Virtual Pulmonary Valve Replacement Interventions with a Personalised Cardiac Electromechanical Model. In *Recent Advances in the 3D Physiological Human*, pages 201–210. Springer.

Mansi, T., Pennec, X., Sermesant, M., Delingette, H., and Ayache, N. (2011). iLogDemons: A demons-based registration algorithm for tracking incompressible elastic biological tissues. *International Journal of Computer Vision*, 92(1):92–111.

Mansi, T., Voigt, I., Georgescu, B., Zheng, X., Mengue, E., Hackl, M., Ionasec, R., Noack, T., Seeburger, J., and Comaniciu, D. (2012). An integrated framework for finite-element modeling of mitral valve biomechanics from medical images: Application to mitralclip intervention planning. *Medical Image Analysis*.

Marbán, E. (2002). Cardiac channelopathies. *Nature*, 415(6868):213–218.

Marchesseau, S., Delingette, H., Peterlik, I., Cotin, S., and Faure, F. (2010a). Technical report on first results on new sofa modules development. Technical Report PASSPORT WP6: D 6.1.

Marchesseau, S., Delingette, H., Sermesant, Cabrera-Lozoya, R., Tobon-Gomez, C., Lekadir, K., Figueras, R., Frangi, A., Rhode, K., Duckett, S., Rinaldi, C., Razavi, R., Leclercq, C., Donal, E., Hernandez, A., Garreau, M., Moireau, P., Chapelle, D., and Ayache, N. (2013a). Personalization of a Cardiac Electromechanical Model using Reduced Order Unscented Kalman Filtering from Regional Volumes. *Submitted to Medical Image Analysis*.

Marchesseau, S., Delingette, H., Sermesant, M., and Ayache, N. (2012a). Fast Parameter Calibration of a Cardiac Electromechanical Model from Medical Images based on the Unscented Transform. *Biomechanics and Modeling in Mechanobiology*, pages 1–17.

Marchesseau, S., Delingette, H., Sermesant, M., Rhode, K., Duckett, S., Rinaldi, C., Razavi, R., and Ayache, N. (2012b). Calibration of a Cardiac Electromechanical Model using the Unscented Transform from Medical Images. *Cardiac Physiome Workshop 2012*.

Marchesseau, S., Delingette, H., Sermesant, M., Rhode, K., Duckett, S., Rinaldi, C., Razavi, R., and Ayache, N. (2012c). Cardiac Mechanical Parameter Calibration based on the Unscented Transform. In *Proc. Medical Image Computing and Computer Assisted Intervention (MICCAI'12)*, volume 7511 of *LNCS*. Springer.

Marchesseau, S., Delingette, H., Sermesant, M., Sorine, M., Rhode, K., Duckett, S., Rinaldi, C., Razavi, R., and Ayache, N. (2012d). Preliminary Specificity Study of the Bestel-Clément-Sorine Electromechanical Model of the Heart using Parameter Calibration from Medical Images. *Journal of the Mechanical Behavior of Biomedical Materials*.

Marchesseau, S., Heimann, T., Chatelin, S., Willinger, R., and Delingette, H. (2010b). Fast porous visco-hyperelastic soft tissue model for surgery simulation: application to liver surgery. *Progress in Biophysics and Molecular Biology*, 103(2-3):185–196.

Marchesseau, S., Heimann, T., Chatelin, S., Willinger, R., and Delingette, H. (2010c). Multiplicative Jacobian Energy Decomposition Method for Fast Porous Visco-Hyperelastic Soft Tissue Model. In *Proc. Medical Image Computing and Computer Assisted Intervention (MICCAI'10)*, volume 6361 of *LNCS*, pages 235–242, Beijing, China. Springer.

Marchesseau, S., Sermesant, M., Billet, F., Delingette, H., and Ayache, N. (2013b). Personnalisation de modèles électromécaniques du coeur par assimilation de données cliniques hétérogènes. In *Analyse d'images cardiaques et thoraciques*. Hermes. In French, Under Review.

Mazhari, R. and McCulloch, A. D. (2000). Effect of laminar orthotropic myofiber architecture on regional stress and strain in the canine left ventricule. *Journal of Elasticity*, 61(4):143–164.

McLeod, K., Prakosa, A., Mansi, T., Sermesant, M., and Pennec, X. (2012). An Incompressible Log-Domain Demons Algorithm for Tracking Heart Tissue. In *Proc. MICCAI Workshop on Statistical Atlases and Computational Models of the Heart: Mapping Structure and Function (STACOM11)*, volume 7085 of *LNCS*, pages 54–65, Toronto. Springer.

Miller, K., Joldes, G., Lance, D., and Wittek, A. (2006). Total lagrangian explicit dynamics finite element algorithm for computing soft tissue deformation. *Communications in Numerical Methods in Engineering*, 23:121–134.

Mitchell, C. and Schaeffer, D. (2003). A two-current model for the dynamics of cardiac membrane. *Bulletin of mathematical biology*, 65(5):767–793.

Moireau, P. and Chapelle, D. (2011a). Reduced-order Unscented Kalman Filtering with application to parameter identification in large-dimensional systems. *COCV*, 17:380–405. doi:10.1051/cocv/2010006.

Moireau, P. and Chapelle, D. (2011b). Reduced-order Unscented Kalman Filtering with application to parameter identification in large-dimensional systems. *COCV*, 17:380–405. doi:10.1051/cocv/2010006.

Moireau, P., Chapelle, D., and Tallec, P. L. (2008). Joint state and parameter estimation for distributed mechanical systems. *Computer Methods in Applied Mechanics and Engineering*, 197:659–677.

Mooney, M. (1940). A theory of large elastic deformation. *Journal of Applied Physics*, 11(2):582–592.

Moreau-Villéger, V., Delingette, H., Sermesant, M., Ashikaga, H., McVeigh, E., and Ayache, N. (2006). Building maps of local apparent conductivity of the epicardium with a 2-d electrophysiological model of the heart. *Biomedical Engineering, IEEE Transactions on*, 53(8):1457–1466.

Müller, M., Dorsey, J., McMillan, L., Jagnow, R., and Cutler, B. (2002). Stable real-time deformations. In *SCA '02: Proceedings of the 2002 ACM SIGGRAPH/Eurographics Symposium on Computer Animation*, pages 49–54.

Nagumo, J., Arimoto, S., and Yoshizawa, S. (1962). An active pulse transmission line simulating nerve axon. *Proceedings of the IRE*, 50(10):2061–2070.

Nash, M. (1998). *Mechanics and material properties of the heart using an anatomically accurate mathematical model*. PhD thesis, University of Auckland.

Nesme, M., Payan, Y., and Faure, F. (2005). Efficient, physically plausible finite elements. In *Eurographics 2005, August, 2005*, Trinity College, Dublin, Ireland.

Niederer, S., Hunter, P., and Smith, N. (2006). A quantitative analysis of cardiac myocyte relaxation: a simulation study. *Biophysical journal*, 90(5):1697–1722.

Noble, D. (1962). A modification of the hodgkin–huxley equations applicable to purkinje fibre action and pace-maker potentials. *J Physiol*, 160:317–352.

Noble, D., Varghese, A., Kohl, P., Noble, P., et al. (1998). Improved guinea-pig ventricular cell model incorporating a diadic space, ikr and iks, and length-and tension-dependent processes. *The Canadian journal of cardiology*, 14(1):123.

Ogden, R. (1972). Large deformation isotropic elasticity-on the correlation of theory and experiment for incompressible rubberlike solids. *Proceedings of the Royal Society of London. A. Mathematical and Physical Sciences*, 326(1567):565–584.

Ottensmeyer, M. (2002). Tempest 1-d: an instrument for measuring solid organ soft tissue properties. *Experimental Techniques*, 26(3):48–50.

Otto, C. (2012). *Practice of Clinical Echocardiography*. Saunders.

Oudry, N. P. J., Chatelin, S., Sandrin, L., Allemann, A., Soler, L., and Willinger, R. (2009). In vivo liver tissue mechanical properties by transient elastography: Comparison with dynamic mechanical analysis. *International Research Council on Biomechanics of Injury 2009*.

Pernod, E., Sermesant, M., Konukoglu, E., Relan, J., Delingette, H., and Ayache, N. (2011). A Multi-Front Eikonal Model of Cardiac Electrophysiology for Interactive Simulation of Radio-Frequency Ablation. *Computers and Graphics*, 35:431–440.

Peterlík, I., Nouicer, M., Duriez, C., Cotin, S., and Kheddar, A. (2011). Constraint-based haptic rendering of multirate compliant mechanisms. *IEEE Transactions on Haptics*, 4(3):175–187.

Peyrat, J.-M., Sermesant, M., Pennec, X., Delingette, H., Xu, C., McVeigh, E. R., and Ayache, N. (2007). A Computational Framework for the Statistical Analysis of Cardiac Diffusion Tensors: Application to a Small Database of Canine Hearts. *IEEE Transactions on Medical Imaging*, 26(11):1500–1514. PMID: 18041265.

Picinbono, G., Delingette, H., and Ayache, N. (2003). Non-Linear Anisotropic Elasticity for Real-Time Surgery Simulation. *Graphical Models*, 65(5):305–321.

Prakosa, A., Sermesant, M., Delingette, H., Marchesseau, S., Saloux, E., Allain, P., Villain, N., and Ayache, N. (2012). Generation of Synthetic but Realistic Time Series of Cardiac Images Combining a Biophysical Model and Clinical Images. *IEEE Trans. Med. Imaging*.

Prakosa, A., Sermesant, M., Delingette, H., Saloux, E., Allain, P., Cathier, P., Etyngier, P., Villain, N., and Ayache, N. (2011). Synthetic Echocardiographic Image Sequences for

Cardiac Inverse Electro-Kinematic Learning. In *Proceedings of Medical Image Computing and Computer Assisted Intervention (MICCAI)*, LNCS, page 8p, Toronto, Canada. Springer, Heidelberg.

Relan, J., Chinchapatnam, P., Sermesant, M., Rhode, K., Ginks, M., Delingette, H., Rinaldi, C. A., Razavi, R., and Ayache, N. (2011a). Coupled Personalization of Cardiac Electrophysiology Models for Prediction of Ischaemic Ventricular Tachycardia. *Journal of the Royal Society Interface Focus*, 1(3):396–407.

Relan, J., Sermesant, M., Delingette, H., and Ayache, N. (2011b). Personalisation of a 3D ventricular electrophysiological model, using endocardial and epicardial contact mapping and MRI. In *Statistical Atlases and Computational Models of the Heart. Imaging and Modelling Challenges - Second International Workshop, STACOM 2011, Held in Conjunction with MICCAI 2011*, pages 14–22.

Rhode, K., Sermesant, M., Brogan, D., Hegde, S., Hipwell, J., Lambiase, P., Rosenthal, E., Bucknall, C., Qureshi, S., Gill, J., Razavi, R., and Hill, D. (2005). A system for real-time XMR guided cardiovascular intervention. *IEEE Transactions on Medical Imaging*, 24(11):1428–1440.

Rivlin, R. (1948). Large elastic deformations of isotropic materials. iv. further developments of the general theory. *Philosophical Transactions of the Royal Society of London. Series A, Mathematical and Physical Sciences*, 241(835):379–397.

Sachse, F. (2004). *Computational cardiology: modeling of anatomy, electrophysiology, and mechanics*, volume 2966. Springer Verlag.

Sainte-Marie, J., Chapelle, D., Cimrman, R., and Sorine, M. (2006). Modeling and estimation of the cardiac electromechanical activity. *Computers & structures*, 84(28):1743–1759.

Schäffler, A. and Schmidt, S. (1999). *Anatomie Physiologie Biologie*. In French.

Sermesant, M., Chabiniok, R., Chinchapatnam, P., Mansi, T., Billet, F., Moireau, P., Peyrat, J., Wong, K., Relan, J., Rhode, K., Ginks, M., Lambiase, P., Delingette, H., Sorine, M., Rinaldi, C., Chapelle, D., Razavi, R., and Ayache, N. (2012). Patient-specific electromechanical models of the heart for the prediction of pacing acute effects in CRT: A preliminary clinical validation. *Medical Image Analysis*, pages 201–215.

Sermesant, M., Delingette, H., and Ayache, N. (2006). An Electromechanical Model of the Heart for Image Analysis and Simulation. *IEEE Transactions in Medical Imaging*, 25(5):612–625.

Sermesant, M., Konukoglu, E., Delingette, H., Coudiere, Y., Chinchaptanam, P., Rhode, K., Razavi, R., and Ayache, N. (2007). An anisotropic multi-front fast marching method for real-time simulation of cardiac electrophysiology. In *Proceedings of Functional Imaging and Modeling of the Heart 2007 (FIMH'07)*, volume 4466 of *LNCS*, pages 160–169.

Smith, N., de Vecchi, A., McCormick, M., Nordsletten, D., Camara, O., Frangi, A., Delingette, H., Sermesant, M., Relan, J., Ayache, N., Krueger, M. W., Schulze, W., Hose, R., Valverde, I., Beerbaum, P., Staicu, C., Siebes, M., Spaan, J., Hunter, P., Weese, J.,

Lehmann, H., Chapelle, D., and Razavi, R. (2011). euheart: Personalized and integrated cardiac care using patient-specific cardiovascular modelling. *Journal of the Royal Society Interface Focus*, 1(3):349–364.

Sundar, H., Davatzikos, C., and Biros, G. (2009). Biomechanically-constrained 4D estimation of myocardial motion. *Medical Image Computing and Computer-Assisted Intervention–MICCAI 2009*, pages 257–265.

Talbot, H., Marchesseau, S., Duriez, C., Courtecuisse, H., Relan, J., Sermesant, M., Cotin, S., and Delingette, H. (2012a). Interactive Electromechanical Model of the Heart for Patient-Specific Therapy Planning and Training using SOFA. *Virtual Human Project (VPH)*.

Talbot, H., Marchesseau, S., Duriez, C., Sermesant, M., Cotin, S., and Delingette, H. (2012b). Interactive Electromechanical Model of the Heart for Rehearsal in the Context of Cardiac Resynchronization Therapy. *Interface Focus*.

Taylor, Z., Comas, O., Cheng, M., Passenger, J., Hawkes, D., Atkinson, D. ., and Ourselin, S. (2009). On modelling of anisotropic viscoelasticity for soft tissue simulation: numerical solution and gpu execution. *Medical Image Analysis*, 13:234–244.

Ten Tusscher, K., Noble, D., Noble, P., and Panfilov, A. (2004). A model for human ventricular tissue. *American Journal of Physiology-Heart and Circulatory Physiology*, 286(4):H1573–H1589.

Teran, J., Blemker, S., Hing, V. N. T., and Fedkiw, R. (2003). Finite volume methods for the simulation of skeletal muscle. In *Eurographics/SIGGRAPH Symposium on Computer Animation*, pages 68–74, San Diego, California.

Teran, J., Sifakis, E., Blemker, S. S., Ng-Thow-Hing, V., Lau, C., and Fedkiw, R. (2005). Creating and simulating skeletal muscle from the visible human data set. *IEEE Transactions on Visualization and Computer Graphics*, 11(3):317–328.

Tobon-Gomez, C., De Craene, M., Dahl, A., Kapetanakis, S., Carr-White, G., Lutz, A., Rasche, V., Etyngier, P., Kozerke, S., Schaffeter, T., Riccobene, C., Martelli, Y., Camara, O., Frangi, A., and Rhode, K. S. (2011). A multimodal database for the 1st cardiac motion analysis challenge. In *Proc. MICCAI Workshop on Statistical Atlases and Computational Models of the Heart: Mapping Structure and Function (STACOM11)*, volume 7085 of *LNCS*, pages 32–43, Toronto. Springer.

Tobon-Gomez, C., Duchateau, N., Sebastian, R., Marchesseau, S., Donal, E., De Craene, M., Pashaei, A., Relan, J., Steghofer, M., Lamata, P., Camara, O., Delingette, H., Duckett, S., Garreau, M., Hernandez, A., Rhode, K. S., Sermesant, M., Ayache, N., Leclercq, C., Razavi, R., Smith, N., and Frangi, A. F. (2012a). Understanding the mechanisms amenable to CRT response: from pre-operative multimodal image data to patient-specific computational models. *Medical & Biological Engineering & Computing*.

Tobon-Gomez, C., Sukno, F. M., Butakoff, C., Huguet, M., and Frangi, A. F. (2012b). Automatic training and reliability estimation for 3D ASM applied to cardiac MRI segmentation. *Phys Med Biol*, 57(13):4155.

Toussaint, N., Stoeck, C. T., Kozerke, S., Sermesant, M., and Batchelor, P. G. (2010). In-vivo Human 3D Cardiac Fibre Architecture: Reconstruction Using Curvilinear Interpolation of Diffusion Tensor Images. In *Proc. Medical Image Computing and Computer Assisted Intervention (MICCAI'10)*, volume 13 of *LNCS*, pages 418–425, Beijing, China. Springer.

Valtorta, D. and Mazza, E. (2005). Dynamic measurements of soft tissue viscoelastic properties with a torsional resonator device. *Medical Image Analysis*, 9(5):481–490.

Veress, A. I., Gullberg, G. T., and Weiss, J. A. (2005). Measurement of strain in the left ventricle during diastole with cine-mri and deformable image registration. *Journal of Biomechanical Engineering*, 127(7):1195–1207.

Veronda, D. and Westmann, R. (1970). Mechanical characterization of skin finite deformations. *Journal of Biomechanics*, 3(1):111–124.

Wan, E. and Van Der Merwe, R. (2000). The unscented Kalman filter for nonlinear estimation. In *Adaptive Systems for Signal Processing, Communications, and Control Symposium 2000. AS-SPCC. The IEEE 2000*, pages 153–158. IEEE.

Wang, V., Lam, H., Ennis, D., Cowan, B., Young, A., and Nash, M. (2009). Modelling passive diastolic mechanics with quantitative MRI of cardiac structure and function. *Medical Image Analysis*, 13(5):773–784.

Weiss, J., Maker, B., and Govindjee, S. (1996). Finite element implementation of incompressible, transversely isotropic hyperelasticity. *Computer Methods in Applied Mechanics and Engineering*, 135:107–128.

Williams, E., Kaplan, J., Thatcher, F., Zimmerman, G., and Knoebel, S. (1980). Prolongation of proton spin lattice relaxation times in regionally ischemic tissue from dog hearts. *Journal of Nuclear Medicine*, 21(5):449.

Wong, K. C., Wang, L., Zhang, H., Liu, H., and Shi, P. (2008). Simulation of Active Cardiac Dynamics with Orthotropic Hyperelastic Material Model. *The MIDAS Journal - Computational Biomechanics for Medicine*.

Wong, K. C. L., Billet, F., Mansi, T., Chabiniok, R., Sermesant, M., Delingette, H., and Ayache, N. (2010). Cardiac motion estimation using a proactive deformable model: evaluation and sensitivity analysis. In *MICCAI Workshop on Statistical Atlases and Computational Models of the Heart: Mapping Structure and Function (STACOM) and a Cardiac Electrophysiological Simulation Challenge (CESC'10)*, volume 6364 of *LNCS*, pages 154–163. Springer.

Xi, J., Lamata, P., Lee, J., Moireau, P., Chapelle, D., and Smith, N. (2011). Myocardial transversely isotropic material parameter estimation from in-silico measurements based on a reduced-order unscented kalman filter. *Journal of the mechanical behavior of biomedical materials*, 4(7):1090–1102.

Xiao, H. and Chen, L. (2002). Hencky's elasticity model and linear stress-strain relations in isotropic finite hyperelasticity. *Acta Mechanica*, 157:51–60.

Yamada, H. (1970). *Strength of Biological Materials*. Williams and Wilkins Co.

Zienkiewicz, C. and Taylor, R. (2000). *The Finite Element Method, Volume 2 : Solid Mechanics*. Butterworth-Heinemann.

Simulation de modèles personnalisés du coeur pour la prédiction de thérapies cardiaques

Résumé : La compréhension clinique et le traitement des maladies cardiovasculaires est extrêmement complexe. Pour chaque patient, les cardiologues sont confrontés à des difficultés pour déterminer la pathologie, choisir une thérapie ou encore sélectionner les patients susceptibles de bien répondre à un traitement donné. Afin de fournir une aide additionnelle aux cardiologues, de nombreuses équipes de recherche étudient la possibilité de planifier de telles thérapies grâce à des modèles biophysiques du cœur. Ils formulent l'hypothèse que l'on peut combiner les données fonctionnelles et anatomiques afin de créer des modèles cardiaques personnalisés à chaque patient qui auraient le potentiel de prédire les bénéfices des différentes thérapies. Les simulations électromécaniques du cœur sont basées sur des modèles informatiques qui peuvent représenter la géométrie, le mouvement et la propagation d'ondes électriques pendant un cycle cardiaque avec suffisamment de précision. L'intégration d'information anatomique, mécanique et électrophysiologique pour un patient donné est essentielle pour construire ce type de modèle.

Dans cette thèse, nous étudions la possibilité de personnaliser le modèle électromécanique de Bestel-Clément-Sorine à partir d'images médicales (IRM). Pour cela, nous proposons en premier lieu une méthode automatique de calibration qui estime les paramètres mécaniques globaux à partir de courbes de pressions et volumes. Ensuite, les paramètres sont personnalisés localement avec un algorithme d'optimisation plus complexe. Cette stratégie de personnalisation a été validée et testée sur plusieurs cas pathologiques et volontaires. Ces différentes contributions ont montré des résultats prometteurs tout au long de cette thèse et certains sont déjà utilisés pour quelques études de recherche.

Mots clés : Modélisation Cardiaque ; Mécanique Cardiaque ; Modèle Informatique ; Etude de Sensibilité ; Etude de Spécificité ; Calibration des Paramètres ; Personnalisation ; Imagerie Medicale

Simulation of patient-specific cardiac models for therapy planning

Abstract: The clinical understanding and treatment of cardiovascular diseases is highly complex. For each patient, cardiologists face issues in determining the pathology, choosing a therapy or selecting suitable patients for the therapy. In order to provide additional guidance to cardiologists, many research groups are investigating the possibility to plan such therapies based on biophysical models of the heart. The hypothesis is that one may combine anatomical and functional data to build patient-specific cardiac models that could have the potential to predict the benefits of different therapies. Cardiac electromechanical simulations are based on computational models that can represent the heart geometry, motion and electrophysiology patterns during a cardiac cycle with sufficient accuracy. Integration of anatomical, mechanical and electrophysiological information for a given subject is essential to build such models.

In this thesis, we focus on the personalisation of the Bestel-Clément-Sorine electromechanical model of the heart from medical images (MRI data). To this end, we first propose an automatic calibration algorithm that estimates global mechanical parameters from volume and pressure curves. Then the parameters are locally personalized with a more complex optimization algorithm. This personalization strategy was validated and tested on several pathological and healthy cases. These contributions have led to promising results through this thesis and some are already used for various research studies.

Keywords: Cardiac Modeling; Cardiac Mechanics; Computer Model; Sensitivity Analysis; Specificity Analysis; Parameter Calibration; Patient-Specific; Medical Imaging

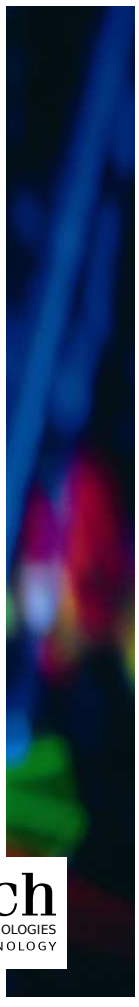

MINES ParisTech

ParisTech
INSTITUT DES SCIENCES ET TECHNOLOGIES
PARIS INSTITUTE OF TECHNOLOGY